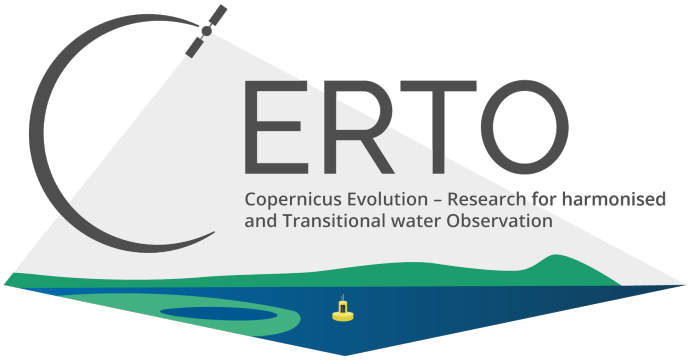

Horizon 2020 LC-SPACE-04-EO-2019-2020

Copernicus Evolution – Research for harmonised and Transitional-water Observation (CERTO)

Project Number: 870349

Deliverable No: D4.4		Work Package: 4	
Date:	26-SEPT-2022	Contract delivery due date	XX-XXX-XXXX
Title:	WP4 Optimal- algorithms		
Lead Partner for Deliverable	PML		
Author(s):	Thomas Jackson, PML, Elizabeth Atwood, PML,		
Dissemination level (PU=public, RE=restricted, CO=confidential)			PU
Report Status (DR = Draft, FI = FINAL)			FI

Acknowledgements

This project has received funding from the European Union's Horizon 2020 research and innovation programme grant agreement N° 870349

Contents

List of figures

List of tables

1 Introduction

This report aims to characterise optical water types (OWT's) based on in-situ field data and to document the recommended algorithms for deriving in-water products for each of those optical water types. This follows the application of fuzzy logic c-means clustering to create both regional cluster sets (see regional reports) and a 'global' cluster set which represents all 6 CERTO study sites, (see global reports).

In a first step (§2), the comparison database is created combining field data with satellite matchup data. In a bid to add additional matched observations of remote-sensing reflectance and in-situ in-water measurements, we convolved in-situ hyper-spectral reflectance data to match the satellite sensor, thus synthesising the missing satellite reflectance. These matched satellite and convolved reflectance measurements formed the training data that were then used to perform OWT assignment and on convolved in-situ reflectance measurements.

Thereafter (§3), differences of OWT assignment based on satellite or in-situ data are assessed, in part to determine if the in-situ data with associated hyper-spectral data can be used for characterisation of the remote sensing classes. The comparison can also be used to make initial assessment of OWT-dependent atmospheric correction error for those data with satellite overpass matchup data.

In the third section (§4), regional OWT are characterised based on their: in-situ sampled biogeochemical parameters of chlorophyll-a (chl-a), suspended particulate matter (SPM), and coloured dissolved organic matter (CDOM); wind and water conditions of secchi depth, wind speed at time of sampling, water depth, and water temperature; and finally reflectance ratios such as the green-NIR ratio used in the HR-OC atmospheric blending scheme.

The fourth section (§5) examines the same parameters and characterisation for the global OWT cluster set. Additionally, there is a novel assessment of regional group cohesion based purely on the reflectance signal, using a comparison of biogeochemical parameters within the grouped regional OWTs.

In the final section (§6) a round robin intercomparison of Rrs-derived product algorithms is performed and the optimal algorithm for use in each OWT is discussed.

2 Database creation

2.1 In-situ data overview

Regional datasets provided by the U Stirling team were collated, noting the region, station name, date/time (in UTC), and location. This work is based on the matchup v02 dataset (Table 1), which comprises the 2022, 2021, and 2020 field data as well as regional historic datasets for all six CERTO regions. In the historic data, some regions have both reflectance and biogeochemical parameter measurements, but sampling was not concurrent (Tamar, Elbe).

Post collation, quality checks on the merged database led to a number of data points being removed/cleaned. The removal criteria were as follows:

- If either date/time or location were missing from the provided datasets, then the data point was removed.

- Secchi disk values that were marked as “bottom” were changed to NA and bottom_vis set to yes, secchi disk values that were given as “>13 m” were set to NA as it is assumed in these cases that the water clarity was longer than the rope used for measuring.
- Negative Chl-a values were removed from the dataset (these all occurred within the Elbe historic data and were taken using a continuous fluorometer).
- Negative absorption measurements of CDOM were also removed (one point from Tamar CDOM 2021, two points Tagus CDOM 2022).
- Wind speeds that were “0-2 m/s” were changed to 1 m/s (these only occurred in the Elbe 2021 dataset).
- Some reflectance datasets, in particular the historic ones, were provided with spectral interval steps greater than 1 nm, in which case these data were interpolated for coherency and simplification in following analyses.

An overview of which data have been used to build the matchup dataset, and which data were provided but not used (and why), is provided in Table 1.

Spectrometer measurement platforms were semi-regional specific (but consistent for a given region), thus spectral range coverage differs across the dataset (Table 2).

For Rrs data collect by TriOS alone, So-Rad or HyperSAS systems, U Stirling provided two results: (1) raw Rrs (<sensor>_Rrs_raw); (2) residual reflected skylight (delta) corrected Rrs (<sensor>_Rrs_corrected) following Jiang et al. (2020). The team at U Stirling recommended analyses be based on the latter. Default Rrs processing was the fingerprint (FP) method but the 3C method was used if they didn’t pass the validity flag in fingerprint processing (FP). The overarching goal was to align with FP method, but if there were some stations where Rrs is missing due to not passing the FP flag, then these data were re-processed using the 3C method. For data which were allowed to pass based on FP, the following data quality flags were retained to assess potential aberrant behaviour during OWT characterisation assessment:

0. Good;
1. Strong oxygen absorption at ~760nm;
2. Out of the processing range of the delta correction method;
3. Extremely turbid water, e,g. algae bloom, floating materials, extremely high TSM, uncertainties may exist in the corrected Rrs;
4. Many negative Rrs exist between 400-700nm in the delta corrected Rrs.

Additional Rrs filtering based on these data quality flags was deemed particularly important for TriOS transect, So-rad and HyperSAS historical data, because these data are continuously measured Rrs (ie. taken automatically) and thus represent thousands of data points. For stationary data, U Stirling recommended to use all Rrs data points, since flags 1-4 are coming mostly from warning of the high oxygen peak around 760nm or extremely turbid water which are expected conditions of the regions being studied and are not indications of questionable quality data points.

*Table 1: Overview of in-situ field data used for OWT characterisation. * 'Full CERTO dataset' indicates that the complete suggested CERTO parameter suite was collected, which for the analysis here was shortened to: wind/water conditions (wind speed, surface temperature, secchi depth, bottom depth, bottom visible), chlorophyll-a, suspended particulate matter (SPM, equivalent to total suspended matter, TSM), and absorption by coloured dissolved organic matter at 440 nm (aCDOM440).*

Region	Dataset	File	Time period covered	N	variables	v02	Notes
Curonian	2022	CERTO_CuronianLagoon_in_situ_data_2022_v1.xlsx	2022.Mar-Jun	16	full CERTO dataset*	yes	WISP Rrs so no DeltaCor (Jiang 2020)
	2021	CERTO_CuronianLagoon_in_situ_data_2021_v1.xlsx	2021.Jul	12	full CERTO dataset*	yes	WISP Rrs so no DeltaCor (Jiang 2020)
	historic	CERTO_CuronianLagoon_in_situ_data_2020_v1.xlsx	2020.Sept	19	full CERTO dataset*	yes	WISP Rrs so no DeltaCor (Jiang 2020)
		CERTO_CuronianLagoon_historical_data_v1.xlsx	2009.Mar-2016.Aug	120	Chl-a, TSM, CDOM, Bottom Depth, Rrs (ASD-FR, SE 3500, WISP-3), aPHYTO - aNAP, bb	yes	1. Rrs from SE-3500 are interpolated into 1nm interval. 2. Rrs from ASD and SE-3500 are firstly smoothed, and then delta corrected; Rrs from WISP3 are not delta corrected as there is no Rrs810 and Rrs840 available.
Danube/ Razelm-Sinoe	2022	CERTO_DanubeDelta_in_situ_data_2022_v1.xlsx	2022.May-Aug	60	full CERTO dataset*	yes	Chl-a concentration were measured by GeoEcoMar using spectrophotometry method. 1. TriOS Rrs only available for stations DDC099 - DDC118, which were measured using Stirling TriOS. The Rrs at other stations were not measured, but So-rad may have some data(transect, so-rad only works when boat is moving). 2. TriOS Rrs were processed using 3C algorithm, because a lot of data didn't pass the flag when using FP method.
		CERTO_DanubeDelta_So-Rad_data_2022_FP_DeltaCor_Jiang_v1.csv	2022.May-Jul	1,701	Timestamp, location, Rrs	yes	
		CERTO_DanubeDelta_TriOS_Rrs_transect_3C_2022_DeltaCor_Jiang_v1.csv	2022.Jun-Jul	12,720	Timestamp, location, Rrs	yes	TriOS Rrs were processed using 3C algorithm, because a lot of data didn't pass the flag when using FP method (assume this is the same as for above CERTO_DanubeDelta_in_situ_data_2022_v1.xlsx)
	2021	CERTO_DanubeDelta_in_situ_data_2021_v1.xlsx	2021.Apr-Oct	82	full CERTO dataset*	yes	Chl-a concentration is measured by GeoEcoMar with spectrophotometry method. (19.12.2022) CDOM pending. There is no stationary Rrs in 2021 Danube campaign, but there are many So-rad Rrs transect data. (16.12.2022) Note that Danube 2021 in-situ Rrs look sometimes wonky.
		CERTO_DanueDelta_So-Rad_data_2021_FP_DeltaCor_Jiang_v1.csv	2021.Apr-Oct	4,951	Timestamp, location, Rrs	yes	
	historic	CERTO_DanubeDelta_historical_data_v1.xlsx	2015.May-2016.Jun	107	Chl-a, TSM, CDOM, Rrs (HyperSAS, TriOS), ISM	yes	Note that some data (Historical data from Danube Delta, Venice Lagoon) are unpublished, so only use them for CERTO project within the CERTO teams. Chla, TSM, ISM data are provided by Adriana in GeoEcoMar, Secchi disk depth, CDOM and Rrs data are from University of Stirling. aCDOM data is scattering corrected. Rrs data is processed using Fingerprint method first, and then delta corrected. All Rrs data in this file have passed the Fingerprint flag. Removed stations with missing date/time or location.
Elbe/ German Bight	2022	N/A	N/A	N/A	N/A	no	no data/ no campaign in 2022
	2021	CERTO_ElbeEstuary_in_situ_data_2021_v1.xlsx	2021.Jun-2021.Jul	9	full CERTO dataset*	yes	CDOM results are a combination of measurements with three LWCC systems with pathlength of 10, 50 and 250 cm. Rrs data re-processed using 3C method

							as some of the stations didn't pass FP flag in previous results. For Rrs data, some of the station the DeltaCor_flag=1, but they are ok to be used, just be careful of the value in NIR wavelengths. There is one station DeltaCor_flag=3, which means the water is extremely turbid, but it's ok to be used. AC-S, bb, CDOM, salinity, TSM, and turbidity data are provided by Rüdiger Röttgers; Rrs, ap, ad, aph and the other data are measured by Stirling.
	historic	CERTO_ElbeEstuary_historical_data_v1.xlsx	2016.May-2020.Dec	24,547	Timestamp, sampling_depth, location, CDOM (m-1), Chl (mg m-3 or µg/l), TSM (FNU)	yes	Only incorporated data from Prandtl_Chl_a (removed negative values). Only incorporated data from Prandtl_turbidity (using conversion factor of FNU*1.1=g/m3, also done for Tamar historic).
		CERTO_hzg_helgoland_Rrs_DeltaCor_Jiang_v1.xlsx	2016.Jul-.Sept	0	Timestamp, location, sampling_depth, Rrs	yes	TriOS, only incorporated data from 2016-07-20
	historic – not used or partially incor-porated	hzg_helgoland_rrs_20160720.csv	2016.Jul	103	Timestamp, location, sampling_depth, Rrs	yes	incorporated into CERTO_hzg_helgoland_Rrs_DeltaCor_Jiang_v1.xlsx
		hzg_helgoland_rrs_20160819.csv	2016.Aug	375	Timestamp, location, sampling_depth, Rrs	no	incorporated into CERTO_hzg_helgoland_Rrs_DeltaCor_Jiang_v1.xlsx, quality appears compromised
		hzg_helgoland_rrs_20160826.csv	2016.Aug	530	Timestamp, location, sampling_depth, Rrs	no	incorporated into CERTO_hzg_helgoland_Rrs_DeltaCor_Jiang_v1.xlsx, quality appears compromised
		hzg_helgoland_rrs_20160908.csv	2016.Sept	295	Timestamp, location, sampling_depth, Rrs	no	incorporated into CERTO_hzg_helgoland_Rrs_DeltaCor_Jiang_v1.xlsx, quality appears compromised
		hzg_helgoland_rrs_20160915.csv	2016.Sept	495	Timestamp, location, sampling_depth, Rrs	no	incorporated into CERTO_hzg_helgoland_Rrs_DeltaCor_Jiang_v1.xlsx, quality appears compromised
		Prandtl_CDOM_Turner_Cyclops_20190101_20210201.csv	2019.Jan-2020.Jun	32,275	Timestamp, sampling_depth, location, CDOM (m-1)	no	incorporated into CERTO_ElbeEstuary_historical_data_v1.xlsx, absorption wavelength not clear but likely in the UV, thus not used in matchups
		Prandtl_Chl_a_Fluor_Turner_Scufa_20190101_20201231.csv	2019.Jan-2020.Oct	29,506	Timestamp, sampling_depth, location, Chl (mg m-3)	yes	incorporated into CERTO_ElbeEstuary_historical_data_v1.xlsx
		Prandtl_Turb_Turner_Scufa_20180101_20201231.csv	2018.Oct-2020.Jun	24,546	Timestamp, sampling_depth, location, Turb (mg m-3)	no	incorporated into CERTO_ElbeEstuary_historical_data_v1.xlsx
		Seemanshoeft_parameters_2016-2020.csv	2016.May-2020.Dec	1,706	Timestamp, location, Temperature, pH, Turbidity (FNU), CHL (µg/l)	no	incorporated into CERTO_ElbeEstuary_historical_data_v1.xlsx, the time of Bunthaus and Seemanshoeft stations in historical data are set to 12:00, this is based on the email communication with Carole (Liz sent) and thus not used into matchups

		Bunthaus_parameters_2016-2020.csv	2016.May-2020.Dec	1,510	Timestamp, location, Temperature, pH, Turbidity (FNU), CHL (µg/l)	no	incorporated into CERTO_ElbeEstuary_historical_data_v1.xlsx, the time of Bunthaus and Seemanshoeft stations in historical data are set to 12:00, this is based on the email communication with Carole (Liz sent) and thus not used into matchups
Tagus	2022	in_situ_lisboat.xlsx	2022.May-2022.Aug	18	date/time (UTC), location, TriOs, SPM, turb, Chla, CDOM, Abs	yes	Giulia has not specified but check anyways since this is for her dissertation and half outside of CERTO. (19.12.2022) Chl-a should finish processing end Dec.
		CERTO_TagusEstuary_in_situ_data_2022_v1.xlsx	2022.Sep	30	full CERTO dataset*	yes	Chl-a concentration were measured using HPLC in FCUL, pending (19.12.2022, should finish end Dec). Rrs were processed using FP method.
		CERTO_TagusEstuary_So-Rad_data_FP_2022_DeltaCor_Jiang_v1.csv	2022.Apr-Nov	30,604	Timestamp, location, Rrs	yes	
		CERTO_TagusEstuary_TriOS_Rrs_transect_FP_2022_DeltaCor_Jiang_v1.csv	2022.Sep	3,219	Timestamp, location, Rrs	yes	
	2021	CERTO_TagusEstuary_in_situ_data_2021_v1.xlsx	2021.Nov	25	full CERTO dataset*	yes	yes DeltaCor (Jiang 2020)
		CERTO_TagusEstuary_So-Rad_data_FP_2021_DeltaCor_Jiang_v1.csv	2021.Jun-.Nov	36,529	Timestamp, location, Rrs	yes	
		CERTO_TagusEstuary_TriOS_Rrs_transect_FP_2021_DeltaCor_Jiang_v1.csv	2021.Oct	7,421	Timestamp, location, Rrs	yes	
	historic	CERTO_TagusEstuary_historical_data_v1	2015.Jan-2020.Jul	270	date/time (UTC), location, TSM[g/m3]	yes	
Tamar/ Plymouth Sound	2022	CERTO_PlymouthSound_in_situ_data_2022_v1.xlsx	2022.Apr	36	full CERTO dataset*	yes	Chl-a were measured using HPLC in Stirling. Spectral CDOM instrument has some problem in UV, so recommend to use CDOM data > 380nm. Rrs were processed using 3C algorithm (350-900nm only), because some of the stations couldn't pass the FP flag; some of the stations, which DeltaCor_flag=1 (Rrs data), they are ok to be used, just be careful of Rrs value in NIR wavelengths.
		CERTO_PlymouthSound_TriOS_Rrs_transect_3C_2022_DeltaCor_Jiang_v1.csv	2022.Apr	4,086	Timestamp, location, Rrs	yes	
		L4+WEC (see entry for historic)			Date, (Time), location, Depth, Temperature, Transmission, PAR, Fluorescence, Density, Oxygen, Salinity, Turbidity (NTU), HPLC_chl, fl_chl, nitrate+nitrite, SST, Sal, Chl, SPM (NTU), Nit, SPM (g/m3)	yes	TSM data (WEC dataset) DOI: 10.5281/zenodo.7273851, please use it when referring to these data. Chl is fluorometric. 2022 data from L4_matchup_database_cleaned.xlsx and wec_spm_2022.txt, see more detailed notes under historic.
		CDOM (see entry for historic)			Timestamp, location, CDOM	yes	2022 data from CDOM_params_v5_LizAtwood_TamarEstuary.csv, see more detailed notes under historic
		So-Rad (see entry for historic)			Timestamp, location, Rrs	yes	2022 data from CERTO_PlymouthSound_So-Rad_data_2020-2022_DeltaCor_Jiang_v1.csv

	2021	CERTO_PlymouthSound_in_situ_data_2021_v1.xlsx	2021.Sep	32	full CERTO dataset*	yes	TriOS: Rrs data re-processed using 3C method as some of the stations didn't pass FP flag in previous results.
		CERTO_PlymouthSound_TriOS_Rrs_transect_3C_2021_DeltaCor_Jiang_v1.csv	2021.Sep	5,686	Timestamp, location, Rrs	yes	
		L4+WEC (see entry for historic)			Date, (Time), location, Depth, Temperature, Transmission, PAR, Fluorescence, Density, Oxygen, Salinity, Turbidity (NTU), HPLC_chl, fl_chl, nitrate+nitrite, SST, Sal, Chl, SPM (NTU), Nit, SPM (g/m3)	yes	TSM data (WEC dataset) DOI: 10.5281/zenodo.7273851, please use it when referring to these data. Chl is fluorometric. 2021 data from L4_matchup_database_cleaned.xlsx and wec_spm_2022.txt, see more detailed notes under historic.
		CDOM (see entry for historic)			Timestamp, location, CDOM	yes	2021 data from CDOM_params_v5_LizAtwood_TamarEstuary.csv, see more detailed notes under historic
		WCO HyperSAS (see entry for historic)			Timestamp, location, Rrs	yes	2021 data from certo_plymouth_hypersas-extract_v1_oct2022.csv, see more detailed notes under historic
		So-Rad (see entry for historic)			Timestamp, location, Rrs	yes	2021 data from CERTO_PlymouthSound_So-Rad_data_2020-2022_DeltaCor_Jiang_v1.csv
	historic	L4+WEC (ie from combined L4_matchup_database_cleaned.xlsx and wec_spm_2022.txt)	2002.Jan-2022.Sep	718	Date, (Time), location, Depth, Temperature, Transmission, PAR, Fluorescence, Density, Oxygen, Salinity, Turbidity (NTU), HPLC_chl, fl_chl, nitrate+nitrite, SST, Sal, Chl, SPM (NTU), Nit, SPM (g/m3)	yes	TSM data (WEC dataset) DOI: 10.5281/zenodo.7273851, please use it when referring to these data. Chl is fluorometry since no HPLC exists 2016-2022. Tamar historic: was missing updated L4 data up until 2022, create v2 based on good L4 data, incorporated vmv's WEC data 2016-2022, either amending to existing L4 data or creating separate entry for new locations.
		CDOM (ie CDOM_params_v5_LizAtwood_TamarEstuary.csv)	2017-2022	141	Time, location, a254, a300, a340, a350, a440	yes	Within estuary dataset shared by PML MBO colleagues (Vas Kitidis & Andy Rees), use within CERTO consortium, PML team should be credited.
		WCO HyperSAS (ie certo_plymouth_hypersas-extract_v1_oct2022.csv)	2016.Apr-2021.Aug	50,057	Timestamp, location, Rrs	yes	HyperSAS data were interpolated into 1 nm, and smoothed (savitzky golay filtering with 21 nm window) to remove noise, and then delta corrected using the same method as previously for other data. Additional flag(flag=5), is to detect noise level of the spectrum in between 450-650nm, because the previous flags are for TriOS and are not able to flag the noise spectra, if you select the DeltaCor_flag=0, most of the data should be okay (not 100%). Tamar historic WCO Rrs data still have some oddities.
		So-Rad (ie CERTO_PlymouthSound_So-Rad_data_2020-2022_DeltaCor_Jiang_v1.csv)	2020-2022		Timestamp, location, Rrs	yes	(09.12.2022, Dalin) So-rad data downloaded from PML sever with the most updated code from Stefan for the period 2020-07 ~ 2022-08. Interpolated data into 1 nm interval then delta corrected using same method for CERTO spectra. Some strange spectra (looks like not a water spectrum) are not flagged using my code, hopefully you could filter them out using the flags from both Stefan and mine to deal with this problem (12.12.2022, Liz) have incorporated data with DeltaCor_flag=0 and q_2=1
	historic – not used	CERTO_PlymouthSound_historical_data.xlsx	Chl: 1992.Feb-2018.Oct	Chl: 1,543		no	(11.10.2022) have made decision to replace this table with the more complete L4 table from Tim Smyth

	or partially incor-porated		TSM: 2001.Jan-2014.Jan	TSM: 496			
		CERTO_2018.csv	2018.May-2018.Jun	4		no	(12.12.2022) this table discarded after provision of wec_spm_2022.txt data
		wec_spm_2022.txt	1988-2020	1,200		no	DOI: 10.5281/zenodo.7273851, please use it when referring to these data. (12.12.2022) see notes for L4 data, essentially used the Sentinel mission overlapping portion of these data to update missing L4 data or adding to in-situ tables for respective time period (historic, 2020, 2021, 2022)
		L4_matchup_database_cleaned.xlsx (replaced WCO_matchup_database.txt)	2002.Jan-2022.Sep	718		no	(13.12.2022) Stirling provided updated CERTO_PlymouthSound_historical_data_v1.xslx but this was missing updated L4 data that goes until 2022, PLM used this table and wec_spm_2022.txt to create a _v2.xlsx (and adding the 2021/22 data to their respective tables)
Venice/ NW Adriatic	2022	CERTO_VeniceLagoon_in_situ_data_2022_v1.xlsx	2022.Sep	39	full CERTO dataset*	yes	Turbidity is measured using SeaPoint turbidimeter at an average value 0.5-1 m; Rrs is measured using WISP-3, no delta correction because the Rrs810 and Rrs840 are not available. 1. Rrs from TriOS are only available from VLA stations (Aretusa boat), Rrs from WISP are available from all stations; 2. Rrs from So-Rad are available from VLL (Litus boat), but transect data only; 13.12.2022: thus use TriOS for stations where available, otherwise use WISP
		CERTO_VeniceLagoon_So_Rad_data_3C_2022_DeltaCor_Jiang_v1.csv	2022.Sep	795	Timestamp, location, Rrs	yes	So-rad Rrs transect data
		CERTO_VeniceLagoon_TriOS_Rrs_transect_FP_2022_DeltaCor_Jiang_v1.csv	2022.Sep	2,358	Timestamp, location, Rrs	yes	TriOS Rrs transect data
	2021	CERTO_VeniceLagoon_in_situ_data_2021_v1.xlsx	2021.Mar-2021.Aug	98	full CERTO dataset*	yes	WISP-3 Rrs so no DeltaCor (Jiang 2020). Rrs were measured using WISP-3; original Rrs for 09/03/2021 are 4 nm intervals (400-780 nm available only), this have been interpolated into 1 nm intervals in this file.
	historic	CERTO_VeniceLagoon_in_situ_data_2020_v1.xlsx	2020.Feb-.Sep	88	full CERTO dataset*	yes	Turbidity measured using SeaPoint turbidimeter at an average value 0.5-1 m. Rrs measured using WISP-3, no delta correction because the Rrs810 and Rrs840 are not available.
		CERTO_VeniceLagoon_historical_data.xlsx	2019.Jan-2019.Aug	122	Date/Time, location, Sampling_Depth, Chl [mg/m-3], TSM [mg/l], ISM [mg/l], Turb CTD [FNU], Secchi disk depth (m), Rrs	yes	Data shared by Federica. Note that, some of the data (Historical data from Danube Delta, Venice Lagoon) are unpublished, so only use them for CERTO project within the CERTO teams. Chl-a concentration measured by CNR-ISMAR using the HPLC method. Turbidity measured using SeaPoint turbidimeter, values are the average between 0.5-1.5m.

Table 2: Overview of field spectrometer specifications of in-situ reflectance data.

CERTO region	Dataset	Reflectance platform
Curonian	2022	WISP-3
	2021	WISP-3
	historic	ASD-FR, WISP-3, SE-3500
Danube	2022	TriOS alone, So-Rad
	2021	So-Rad
	historic	HyperSAS, TriOS
Elbe	2022	N/A
	2021	TriOS
	historic	TriOS
Tagus	2022	TriOS alone, So-Rad
	2021	TriOS
	historic	N/A
Tamar	2022	TriOS alone, So-Rad
	2021	TriOS alone, So-Rad, HyperSAS
	historic	So-Rad, HyperSAS
Venice	2022	TriOS alone, So-Rad
	2021	WISP-3
	historic	WISP-3

2.2 Matchup analysis

Time and location of sampling were used to search for same-day satellite acquisitions from both Sentinel-3 A & B platforms. Satellite data were atmospherically corrected following the same procedure as for training data (i.e. processed with POLYMER, following the CALIMNOS processing chain). Exact pixel matchup value as well as statistics (mean, median, standard deviation, count of valid/non-nan pixels) of the 9-nearest neighbour pixels were collated. Note that these neighbour pixels are based on geographic distance from sampling location and thus do not necessarily represent a 3x3 box around the exact overlapping pixel. Difference between sampling time and satellite acquisition was calculated to allow for more conservative time-window assessment as needed, but initial analyses are based on same-day matchup data. An overview of matchup totals is presented in Table 3. In a number of sites the use of the 9-nearest-neighbour pixels adds a relatively small number of matched data (Curonian, Danube, Tagus), and in others it increases the number of matched data significantly (Elbe, Tamar, Venice). By taking the mean and standard deviation of the nearest-neighbour pixels we can also calculate the co-efficient of variation of the match-up-macro-pixel. This coefficient of variation has been used as a filter for matchups in similar studies such as those of the OC-CCI and CMEMS groups. Although using same-day matchups is not ideal in coastal waters, especially those with strong or large tidal ranges, this work is data limited and compromises must be made. Further study into the impact of delta-t for matchups and the impact of the tidal cycle in regions such as the Tagus will be covered in other documents.

*Table 3: Matchups per region, for each dataset (2022/2021/historic) separately and as regional total. Exact pixel matchups listed separately to the 9-neareset neighbour totals separately. Summed region totals provided at bottom. *Historic datasets have extensive Rrs and biogeochemical data, but these were not collected concurrently.*

			OLCI	
Region	**Dataset**	**In-situ**	**Exact**	**9-NN**
Curonian	2022	16	16	16
	2021	12	12	12
	historic	139	33	35
	Regional total	*167*	*61*	*63*
Danube/ Razelm-Sinoe	2022	14,480	10,374	10,414
	2021	5,033	3,326	3,515
	historic	88	18	19
	Regional total	*19,601*	*13,718*	*13,948*
Elbe/ German Bight	2022	0	0	0
	2021	9	2	3
	historic*	53,504	6,251	7,481
	Regional total	*53,513*	*6,253*	*7,484*
Tagus	2022	33,869	5,113	5,773
	2021	43,975	7,437	7,568
	historic	269	61	63
	Regional total	*78,113*	*12,611*	*13,404*
Tamar/ Plymouth Sound	2022	6,446	2070	2551
	2021	12,550	912	1153
	historic*	24,567	4,292	4,713
	Regional total	*43,563*	*7,274*	*8,417*
Venice/ NW Adriatic	2022	3,192	214	335
	2021	98	45	59
	historic	210	85	109
	Regional total	*3,500*	*344*	*503*
Totals		***198,457***	***40,261***	***43,819***

2.3 OWT membership assignment

Matchup data memberships to both regional and global OWT cluster sets were calculated, which are fully described in the regional and global reports. Membership values were calculated as normalised Euclidean distance values, which have been found to better represent cluster spread for transitional waters, although the maximum reduced degrees of freedom chi2 membership value is retained to ensure that the data point is well represented (i.e. membership > 0.6) by at least one cluster in the set. Dominant OWT was also calculated, which remains the same whether considering Euclidean or Mahalanobis (chi2 distance) memberships.

2.4 Convolution in-situ to satellite bands

In-situ reflectance data were convolved to satellite sensor bands using the signal response function (SRF) available on the sensor's Copernicus webpage (Figure 1).

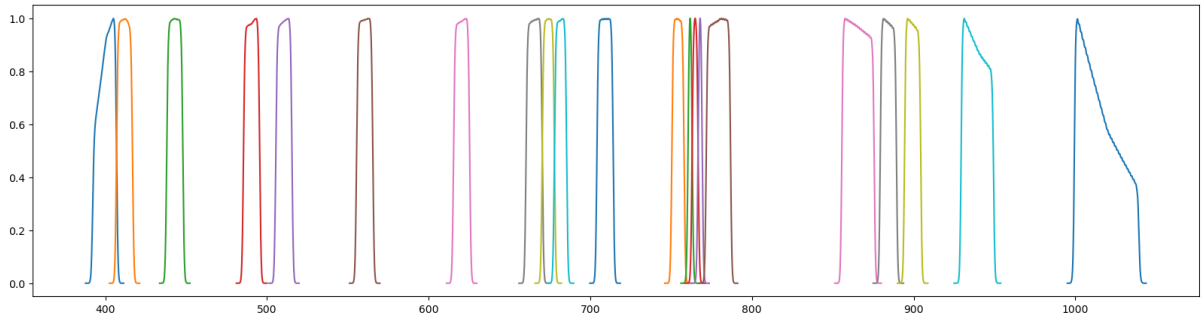

Figure 1: Sensor SRF functions (Sentinel-3A OLCI) used for convolution.

SRF data were trimmed to match the spectral range from the in-situ dataset (namely wavelengths from 324 nm to 953 nm). Satellite bands whose SRF would be heavily impacted by this range reduction (namely the mid NIR and longer wavelength channels) were not convolved. Example convolved data are shown in Figure 2.

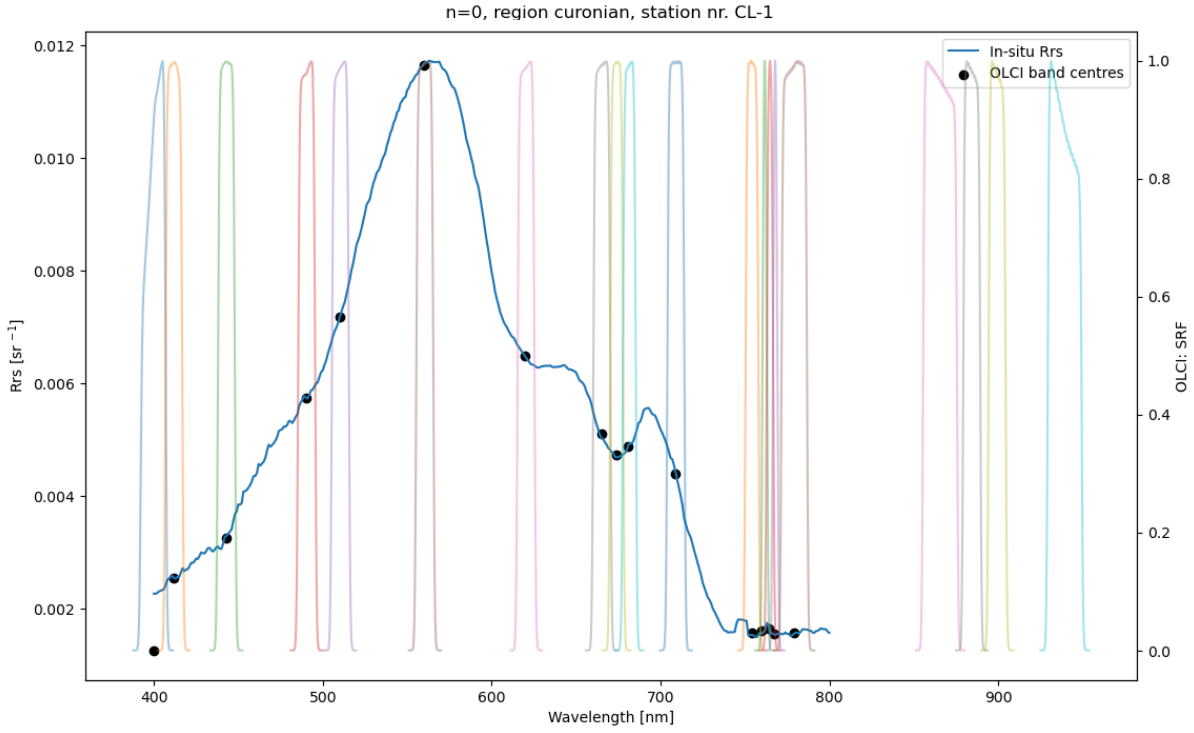

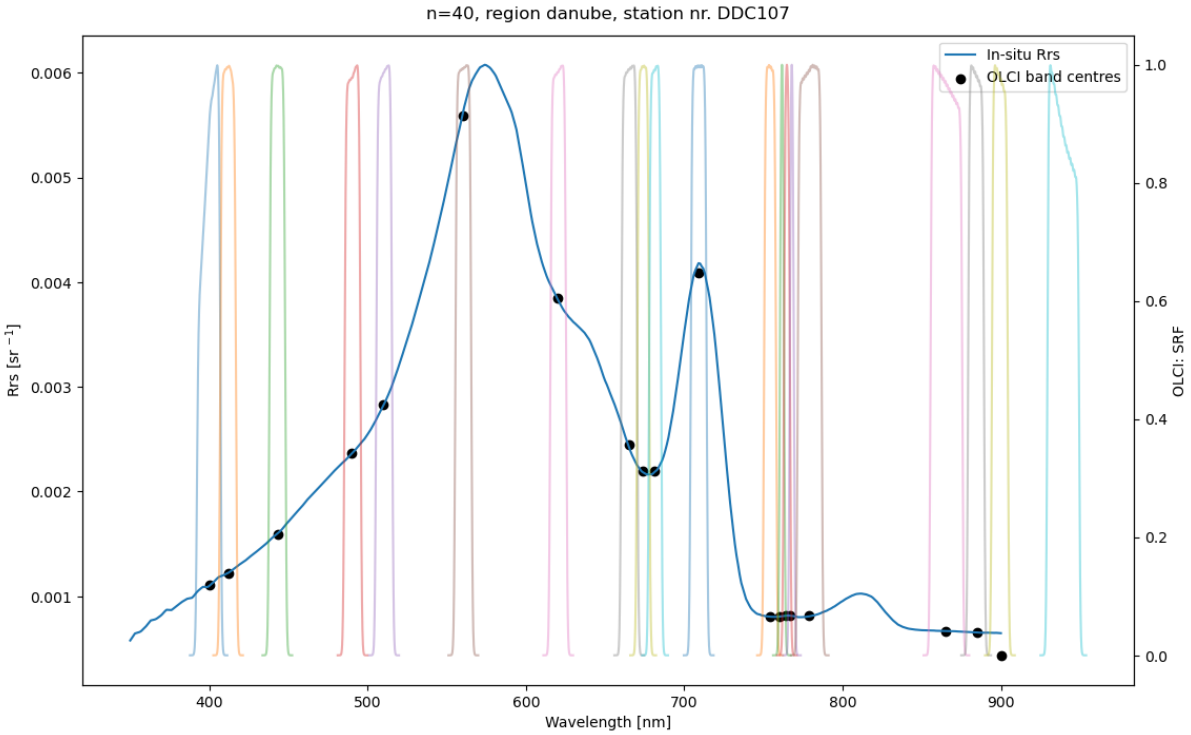
n=40, region danube, station nr. DDC107
In-situ Rrs
OLCI band centres
Rrs [sr⁻¹]
OLCI: SRF
Wavelength [nm]
0.001
0.002
0.003
0.004
0.005
0.006
0.0
0.2
0.4
0.6
0.8
1.0
400
500
600
700
800
900

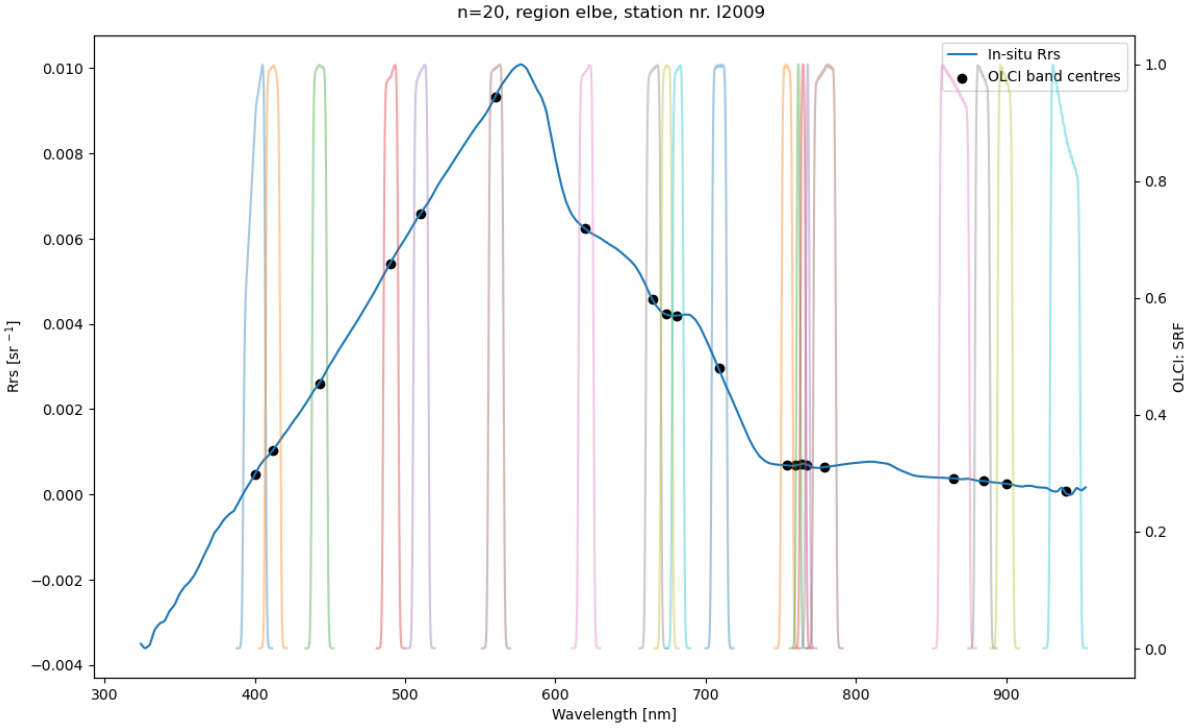
n=20, region elbe, station nr. I2009
In-situ Rrs
OLCI band centres
Rrs [sr⁻¹]
OLCI: SRF
Wavelength [nm]
−0.004
−0.002
0.000
0.002
0.004
0.006
0.008
0.010
0.0
0.2
0.4
0.6
0.8
1.0
300
400
500
600
700
800
900

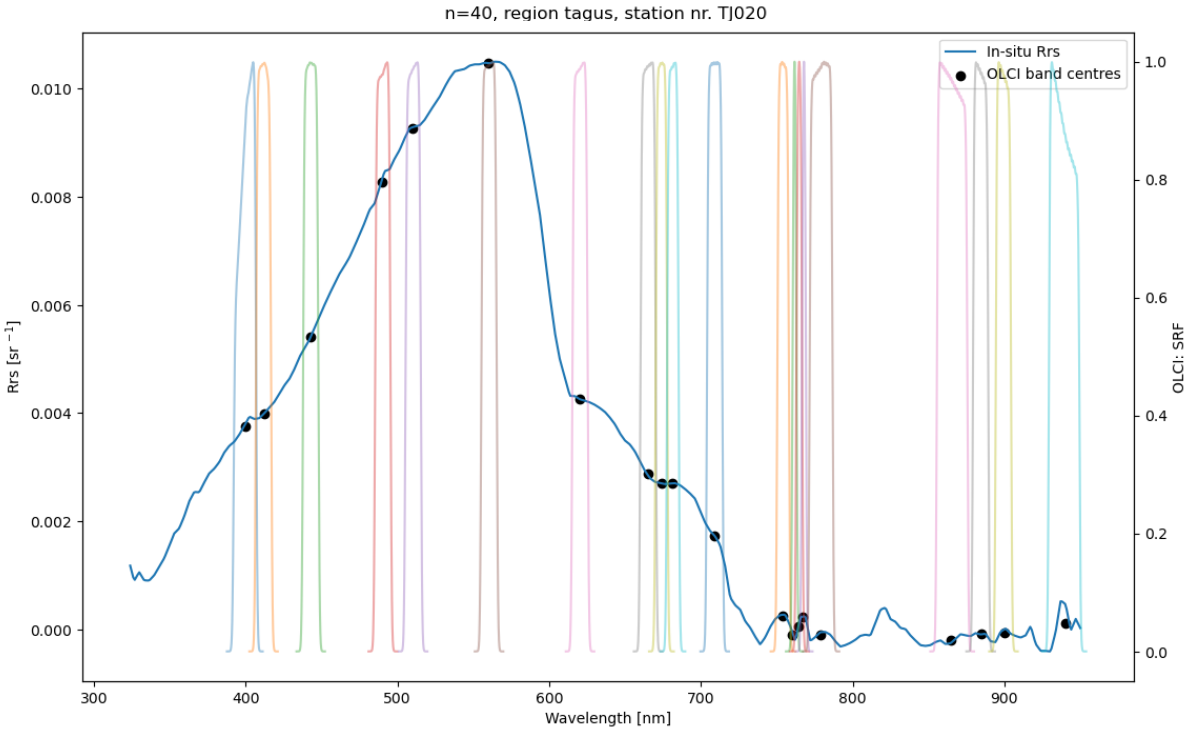
n=40, region tagus, station nr. TJ020
In-situ Rrs
OLCI band centres
Rrs [sr⁻¹]
OLCI: SRF
Wavelength [nm]
0.000
0.002
0.004
0.006
0.008
0.010
0.0
0.2
0.4
0.6
0.8
1.0
300
400
500
600
700
800
900

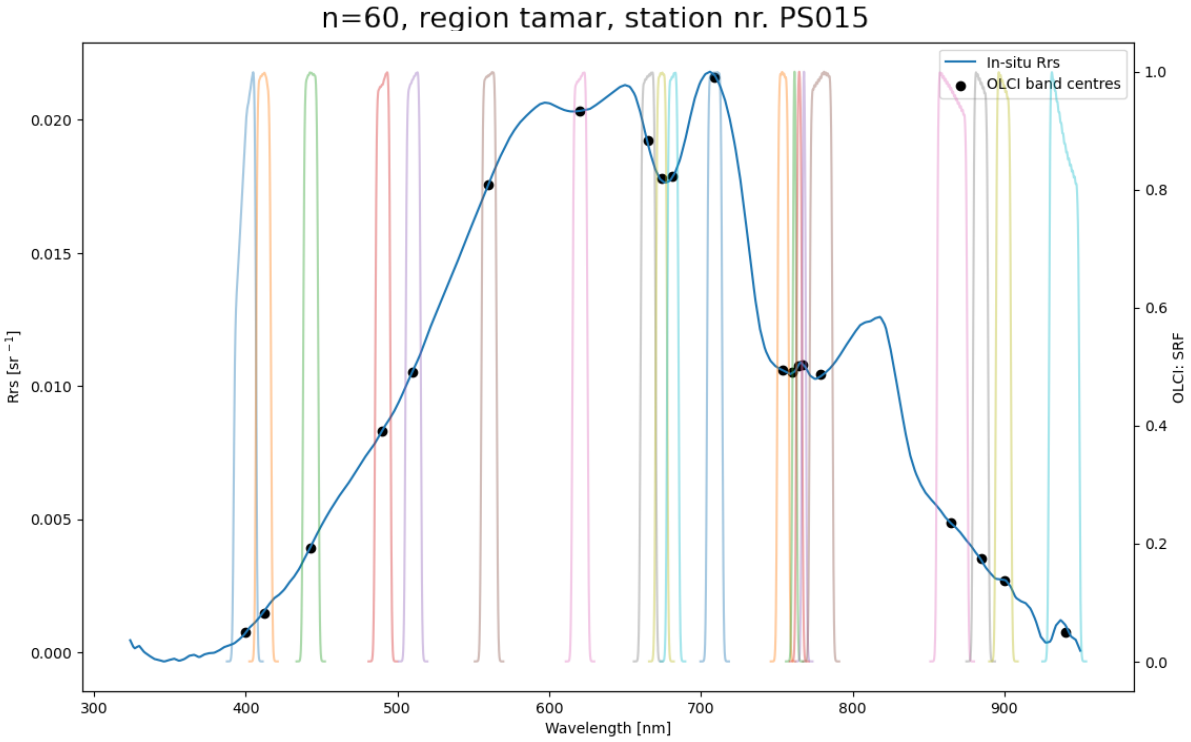
n=60, region tamar, station nr. PS015
In-situ Rrs
OLCI band centres
Rrs [sr⁻¹]
OLCI: SRF
Wavelength [nm]
0.000
0.005
0.010
0.015
0.020
0.0
0.2
0.4
0.6
0.8
1.0
300
400
500
600
700
800
900

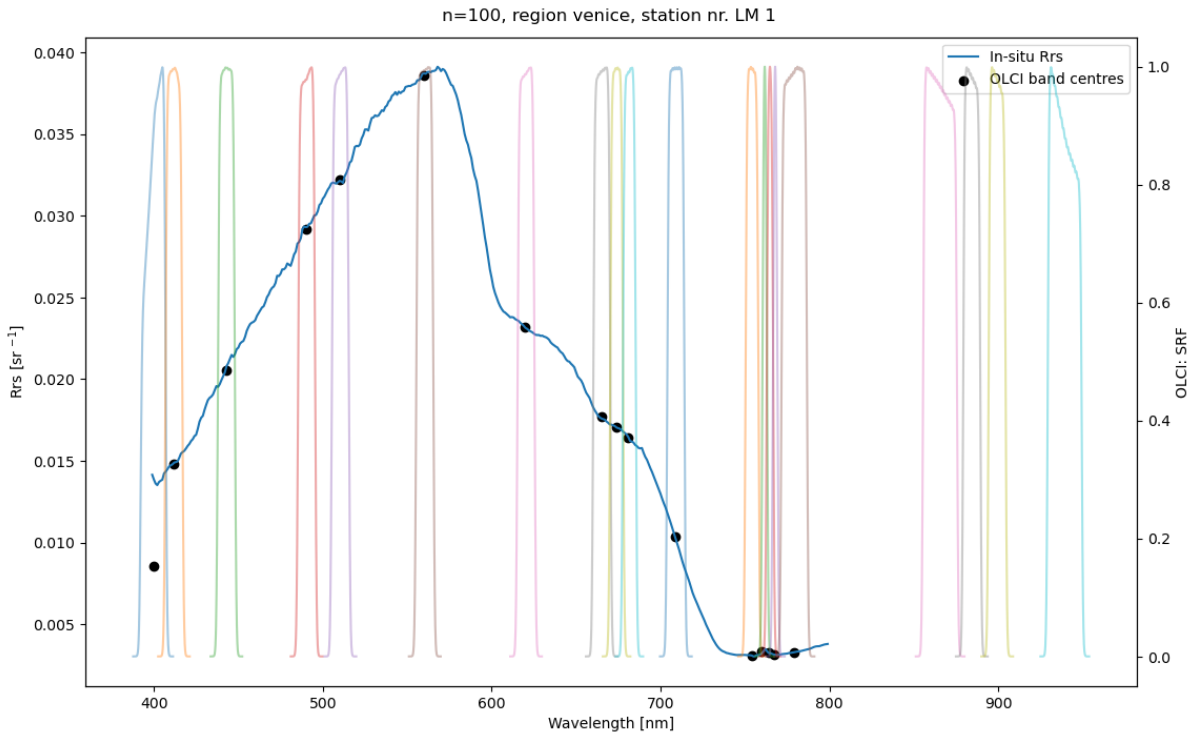

Figure 2: Convolved in-situ data (black points), with OLCI sensor SRF shown in the background (faded multicolour dependent on sensor band), overlaid with in-situ hyperspectral signal (blue curve).

In addition to calculating OWT memberships based on the matched satellite reflectance, OWT memberships were also assigned based on convolved sensor bands, following the same structure as presented in the section previous (§2.3). The goal of this step was to increase OWT characterisation data beyond that provided by the satellite matchups, i.e. can matchup data be expanded using the in-situ data where satellite data may be absent (described in more detail in §3.1). As mentioned in §2.1, some reflectance data did not pass data quality flags, totals are presented in Table 4.

Table 4: Convolution totals per region that are in addition to satellite match-up numbers listed in Table 3 (i.e. sufficient spectral range Rrs data are available for performing sensor convolution, but an exact satellite matchup is not available).

Region	Dataset	In-situ	Add. OLCI convolution
Curonian	2022	16	0
	2021	12	0
	historic	139	45
	Regional total	*167*	*45*
Danube/ Razelm-Sinoe	2022	14,480	4,452
	2021	5,033	1,812
	historic	88	53
	Regional total	*19,601*	*6,317*
Elbe/ German Bight	2022	0	0
	2021	9	7
	historic	53,504	0
	Regional total	*53,513*	*7*
Tagus	2022	33,869	27,886
	2021	43,975	34,587
	historic	269	0
	Regional total	*78,113*	*62,473*
Tamar/ Plymouth Sound	2022	6,446	4,628
	2021	12,550	11,562
	historic	24,567	19,649
	Regional total	*43,563*	*35,839*
Venice/ NW Adriatic	2022	3,192	2,963
	2021	98	0
	historic	210	0
	Regional total	*3,500*	*2,963*
Total		***198,457***	***107,644***

2.5 Full database overview

Table 5: Tabular key to matchup data.

Category	**Column headers**
Station data	'region', 'stn_name', 'obs_date_utc', 'obs_lat', 'obs_lon'
Wind/water conditions	'wwc_wind _m_s', 'wwc_surf_temp_C', 'wwc_secchi_m', 'wwc_depth_m', 'wwc_bott_vis'
Biogeochemical	'chl_mg_m3', 'SPM_g_m3', 'aCDOM440_ m-1'
In-situ reflectance	'Rrs_324', 'Rrs_325', …, 'Rrs_953'
MSI matchup value at exact pixel overlap	'msi_Rw490', 'msi_Rw560', 'msi_Rw665', 'msi_Rw705', 'msi_Rw740', 'msi_Rw783', 'msi_Rw865', 'msi_Rw945', 'msi_Rw1375', 'msi_Rw1610', 'msi_Rw2190'
9-nearest neighbour pixels stats and count valid (non-nan) pixels	'msi_Rw..._mean', 'msi_Rw..._std', 'msi_Rw…_median', 'msi_count'
MSI acquisition date	'msi_date_utc'
Delta time between satellite acquisition to field sampling time	'msi_delta_date_utc'
SRF convolution in-situ data ('msi_insitu')	'msi_insitu_Rw…'
OWT normalised Euclidean distance memberships ('eucC') for regional cluster sets ('reg')	'msi_OWT_reg_eucC…'
OWT reduced chi2 memberships	'msi_OWT_reg_maxRedChi2'
Dominant OWT	'msi_OWT_reg_domC'
Memberships to regional clusters based on convolved bands from in-situ data	'msi_insitu_OWT_reg_eucC…' 'msi_insitu_OWT_reg_maxRedChi2', 'msi_insitu_OWT_reg_domC'
Memberships based on global cluster set ('glo')	'msi_OWT_glo_eucC…', 'msi_OWT_glo_maxRedChi2', 'msi_OWT_glo_domC'
Memberships based on global cluster set plus convolved bands from in-situ data	'msi_insitu_OWT_glo_eucC…', 'msi_insitu_OWT_glo_maxRedChi2', 'msi_insitu_OWT_glo_domC'

2.6 OWT coverage overview

An overview of OWT representation is provided for the regional cluster sets: based solely on satellite data in Table 6; or based on satellite plus in-situ convolved data in Table 7. How those regional cluster sets are represented in the groupings used as basis for the global cluster set is presented in Table 8. These values were used for the 2022 field campaign planning to target OWT classes not yet well represented in the full dataset. Global cluster set OWT representation, which is assigned based on membership values to the trained global cluster centres, is presented in Table 9 (based solely on satellite data) and Table 10 (based on satellite plus in-situ convolved data).

Table 6: Regional OWT representation based solely on satellite matchups. Not all regional OWT sets have 10 classes, where this is not the case is marked with N/A.

		OLCI Regional OWT										
Region	**Dataset**	**0**	**1**	**2**	**3**	**4**	**5**	**6**	**7**	**8**	**9**	**10**
Curonian	2022	0	1	4	0	8	2	0	0	0	1	0
	2021	0	0	0	1	2	1	6	2	0	0	0
	historic	0	0	0	1	3	0	7	12	6	3	0
	Regional totals	***0***	***1***	***4***	***2***	***13***	***3***	***13***	***14***	***6***	***4***	***0***
Danube/ Razelm-Sinoe	2022	0	44	239	45	288	294	554	0	6,140	2,348	N/A
	2021	0	49	10	205	25	569	554	0	1,448	235	N/A
	historic	0	0	1	2	2	0	8	0	4	0	N/A
	Regional totals	***0***	***93***	***250***	***252***	***315***	***863***	***1,116***	***0***	***7,592***	***2,583***	***--***
Elbe/ German Bight	2022	0	0	0	0	0	0	N/A	N/A	N/A	N/A	N/A
	2021	1	1	0	0	0	0	N/A	N/A	N/A	N/A	N/A
	historic	1,077	547	833	1,182	1,637	779	N/A	N/A	N/A	N/A	N/A
	Regional totals	***1,078***	***548***	***833***	***1,182***	***1,637***	***779***	***--***	***--***	***--***	***--***	***--***
Tagus	2022	565	660	417	1,068	1,523	291	N/A	N/A	N/A	N/A	N/A
	2021	354	42	26	94	3,358	3,208	N/A	N/A	N/A	N/A	N/A
	historic	8	2	1	7	25	16	N/A	N/A	N/A	N/A	N/A
	Regional totals	***927***	***704***	***444***	***1,169***	***4,906***	***3,515***	***--***	***--***	***--***	***--***	***--***
Tamar/ Plymouth Sound	2022	88	372	818	275	0	141	N/A	N/A	N/A	N/A	N/A
	2021	209	205	325	151	0	3	N/A	N/A	N/A	N/A	N/A
	historic	1,727	1,480	649	385	28	16	N/A	N/A	N/A	N/A	N/A
	Regional totals	***2,024***	***2,057***	***1,792***	***811***	***28***	***160***	***--***	***--***	***--***	***--***	***--***
Venice/ NW Adriatic	2022	0	1	0	38	175	0	N/A	N/A	N/A	N/A	N/A
	2021	0	1	11	14	11	8	N/A	N/A	N/A	N/A	N/A
	historic	0	3	23	21	27	8	N/A	N/A	N/A	N/A	N/A
	Regional totals	***0***	***5***	***34***	***73***	***213***	***16***	***--***	***--***	***--***	***--***	***--***

Table 7: Same as Table 6, now based on satellite matchups and in-situ convolved data.

		OLCI Regional OWT										
Region	**Dataset**	**0**	**1**	**2**	**3**	**4**	**5**	**6**	**7**	**8**	**9**	**10**
Curonian	2022	0	1	4	0	8	2	0	0	0	1	0
	2021	0	0	0	1	2	1	6	2	0	0	0
	historic	0	0	0	1	12	8	7	12	6	5	26
	Regional totals	***0***	***1***	***4***	***2***	***22***	***11***	***13***	***14***	***6***	***6***	***26***
Danube/ Razelm-Sinoe	2022	2	44	247	51	288	300	606	1	6,523	6,342	N/A
	2021	0	49	10	211	25	588	614	1	1,853	1,556	N/A
	historic	11	0	8	7	4	2	15	0	12	11	N/A
	Regional totals	***13***	***93***	***265***	***269***	***317***	***890***	***1,235***	***2***	***8,388***	***7,909***	***--***
Elbe/ German Bight	2022	0	0	0	0	0	0	N/A	N/A	N/A	N/A	N/A
	2021	5	3	1	0	0	0	N/A	N/A	N/A	N/A	N/A
	historic	1,077	547	833	1,182	1,637	779	N/A	N/A	N/A	N/A	N/A
	Regional totals	***1,082***	***550***	***834***	***1,182***	***1,637***	***779***	***--***	***--***	***--***	***--***	***--***
Tagus	2022	1,507	1,068	493	4,061	9,026	16,255	N/A	N/A	N/A	N/A	N/A
	2021	1,489	1,206	209	2,357	20,519	15,889	N/A	N/A	N/A	N/A	N/A
	historic	8	2	1	7	25	16	N/A	N/A	N/A	N/A	N/A
	Regional totals	***3,004***	***2,276***	***703***	***6,425***	***29,570***	***32,160***	***--***	***--***	***--***	***--***	***--***
Tamar/ Plymouth Sound	2022	331	1,937	1,857	1,077	979	141	N/A	N/A	N/A	N/A	N/A
	2021	1,817	4,698	1,424	1,188	3,325	3	N/A	N/A	N/A	N/A	N/A
	historic	6,579	8,403	2,958	3,001	2,977	16	N/A	N/A	N/A	N/A	N/A
	Regional totals	***8,727***	***15,038***	***6,239***	***5,266***	***7,281***	***160***	***--***	***--***	***--***	***--***	***--***
Venice/ NW Adriatic	2022	0	1	1	165	1,199	1,811	N/A	N/A	N/A	N/A	N/A
	2021	0	1	11	14	11	8	N/A	N/A	N/A	N/A	N/A
	historic	0	3	23	21	27	8	N/A	N/A	N/A	N/A	N/A
	Regional totals	***0***	***5***	***35***	***200***	***1,237***	***1,827***	***--***	***--***	***--***	***--***	***--***

Table 8: Global OWT representation based solely on satellite matchups. Regional OWT clusters grouped to form basis for global OWT are listed (cur: Curonian; dan: Danube/Razelm-Sinoe;,elb: Elbe/German Bight; tag: Tagus; tam: Tamar/Plymouth Sound; ven: Venice/NW Adriatic; _<number> indicates which regional cluster). Total for the global OWT from the 2022, 2021 and historic datasets are listed separately, along with summed total. Regional additional column indicates with how many more points a regional OWT is represented when taking into account other grouped regional OWT classes.

OLCI Global OWT	Basis regional OWT grouping	2022	2021	historic	Total	Regional additional
0	cur_1	1	0	0	780	779
	elb_5	0	0	779		1
1	dan_0	0	0	0	2951	2951
	tag_0	565	354	8		2024
	tam_0	88	209	1727		927
	ven_0	0	0	0		2951
2	tag_1	660	42	2	2761	2057
	tam_1	372	205	1480		704
3	cur_3	0	1	1	1639	1637
	elb_4	0	0	1637		2
4	dan_1	44	49	0	2334	2241
	tag_2	417	26	1		1890
	tam_2	818	325	649		542
	ven_1	1	1	3		2329
5	dan_3	45	205	2	1434	1182
	elb_3	0	0	1182		252
6	dan_4	288	25	2	2323	2008
	tag_3	1068	94	7		1154
	tam_3	275	151	385		1512
	tam_4	0	0	28		2295
7	dan_6	554	554	8	1877	761
	elb_1	0	1	547		1329
	ven_4	175	11	27		1664
8	elb_0	0	1	1077	4593	3515
	tag_5	291	3208	16		1078
9	cur_9	1	0	3	4	0
	cur_10	0	0	0		4
10	dan_8	6140	1448	4	10191	2599
	dan_9	2348	235	0		7608
	ven_5	0	8	8		10175
11	dan_5	294	569	0	6675	5812
	elb_2	0	0	833		5842
	tag_4	1523	3358	25		1769
	ven_3	38	14	21		6602
12	cur_4	8	2	3	16	3
	cur_5	2	1	0		13
13	dan_2	239	10	1	284	34
	ven_2	0	11	23		250
14	cur_0	0	0	0	4	4
	cur_2	4	0	0		0
15	cur_6	0	6	7	33	20
	cur_7	0	2	12		19
	cur_8	0	0	6		27
16	dan_7	0	0	0	--	--
17	tam_5	141	3	16	--	--

Table 9: Global OWT representation based solely on satellite matchups, listed separately for region and dataset (2022/2021/historic) with class totals at the bottom.

		OLCI Global OWT																	
Region	**Dataset**	**0**	**1**	**2**	**3**	**4**	**5**	**6**	**7**	**8**	**9**	**10**	**11**	**12**	**13**	**14**	**15**	**16**	**17**
Curonian	2022	2	1	0	3	0	0	0	1	0	5	0	2	0	1	0	1	0	0
	2021	0	0	0	0	0	0	0	1	1	2	0	0	0	8	0	0	0	0
	historic	0	0	0	2	0	0	0	1	0	1	0	0	0	26	0	2	0	0
Danube/ Razelm-Sinoe	2022	0	0	0	111	0	0	107	128	64	45	0	40	161	951	119	925	216	7,085
	2021	0	0	0	0	17	0	44	47	24	177	135	316	1	576	243	154	59	1,302
	historic	0	0	0	1	0	0	0	0	0	2	0	0	2	0	9	0	0	3
Elbe/ German Bight	2022	0	0	0	0	0	0	0	0	0	0	0	0	0	0	0	0	0	0
	2021	0	0	0	0	0	0	0	0	0	0	0	0	0	0	0	2	0	0
	historic	115	325	52	676	387	33	270	921	80	627	245	501	65	150	198	358	981	71
Tagus	2022	290	44	68	91	259	28	555	800	316	1,122	400	152	33	0	258	18	90	0
	2021	276	10	39	17	10	18	12	91	19	123	529	1,228	0	0	2,901	1,509	296	4
	historic	0	0	0	2	0	0	3	13	3	6	4	6	0	0	11	8	1	2
Tamar/ Plymouth Sound	2022	5	40	113	0	83	215	536	401	253	47	0	0	1	0	0	0	0	0
	2021	0	18	236	0	91	87	364	0	94	0	0	0	3	0	0	0	0	0
	historic	336	757	1,222	21	468	606	583	42	189	26	20	0	15	0	0	0	0	0
Venice/ NW Adriatic	2022	0	0	0	0	0	0	0	0	1	32	18	6	152	0	5	0	0	0
	2021	0	0	0	0	0	0	2	4	6	2	7	4	3	0	10	0	0	7
	historic	0	0	0	0	1	0	5	10	8	12	6	3	14	2	13	0	0	8
	Global totals	***1,024***	***1,195***	***1,730***	***924***	***1,316***	***987***	***2,481***	***2,460***	***1,058***	***2,229***	***1,364***	***2,258***	***450***	***1,714***	***3,767***	***2,977***	***1,643***	***8,482***

Table 10: Global OWT representation now based on satellite matchups and in-situ convolved data, listed separately for region and dataset (2022/2021/historic) with class totals at the bottom.

		OLCI Global OWT																	
Region	**Dataset**	**0**	**1**	**2**	**3**	**4**	**5**	**6**	**7**	**8**	**9**	**10**	**11**	**12**	**13**	**14**	**15**	**16**	**17**
Curonian	2022	2	1	0	3	0	0	0	1	0	5	0	2	0	1	0	1	0	0
	2021	0	0	0	0	0	0	0	1	1	2	0	0	0	8	0	0	0	0
	historic	0	0	0	2	0	0	0	1	0	4	0	13	0	27	0	4	23	3
Danube/ Razelm-Sinoe	2022	2	0	0	117	0	0	107	132	64	48	6	42	162	951	142	952	4,354	7,325
	2021	1	0	0	0	17	0	44	47	24	177	135	327	2	578	260	200	557	2,538
	historic	9	1	0	4	1	0	0	5	0	6	0	1	4	2	12	2	6	17
Elbe/ German Bight	2022	0	0	0	0	0	0	0	0	0	0	0	0	0	0	0	0	0	0
	2021	0	0	0	0	0	0	0	0	0	0	0	1	0	0	0	4	3	1
	historic	115	325	52	676	387	33	270	921	80	627	245	501	65	150	198	358	981	71
Tagus	2022	673	80	81	576	300	75	584	1,500	385	2,476	2,132	1,608	2,800	14	5,419	140	2,724	10,843
	2021	1,095	140	159	290	232	76	162	1,386	387	1,600	7,889	2,387	977	4	13,490	1,531	1,231	8,633
	historic	0	0	0	2	0	0	3	13	3	6	4	6	0	0	11	8	1	2
Tamar/ Plymouth Sound	2022	42	108	267	104	902	538	1,425	942	676	443	342	143	47	0	32	1	216	94
	2021	11	98	791	909	625	1,133	741	3,283	200	1,593	316	400	14	0	248	594	945	554
	historic	456	2,904	5,570	499	3,302	1,842	2,472	1,654	1,730	1,012	779	20	1,373	0	116	3	9	193
Venice/ NW Adriatic	2022		0	0	0	0	0	0	0	4	42	223	6	865	0	394	0	2	1,641
	2021	0	0	0	0	0	0	2	4	6	2	7	4	3	0	10	0	0	7
	historic	0	0	0	0	1	0	5	10	8	12	6	3	14	2	13	0	0	8
	Global totals	***2,406***	***3,657***	***6,920***	***3,182***	***5,767***	***3,697***	***5,815***	***9,900***	***3,568***	***8,055***	***12,084***	***5,464***	***6,326***	***1,737***	***20,345***	***3,798***	***11,052***	***31,930***

3 Initial assessment of OWT-dependent atmospheric correction artifact

3.1 OWT assignment by satellite or in-situ reflectance

It is of interest to know if characterisation of OWT can be expanded beyond satellite matchup data through the use of in-situ reflectance data. The acceptable time window between sampling time and satellite overpass is an active point of discussion, though this time window must be smaller for the potentially highly variable hydrodynamic conditions in transitional water systems, due to factors like river discharge, tidal state, or wind conditions. Consistent dominant OWT assignment based on satellite data or from in-situ convolved data would potentially greatly increase the sample size. Comparing results using satellite data and convolved in-situ data, we find that the dominant OWT assignment agree for almost 50% of the matchup points for the regional cluster set (Table 11). This drops to about 20% for the global cluster set. Total potential matches (for this sensor, 30,960) is based upon both the satellite matchup and the in-situ convolved data being valid, which is different to totals presented in Table 3 and Table 4. Distribution of differences between dominant OWT assigned from satellite data as compared with that assigned from convolved data is shown in Figure 3.

Table 11:Overview of the number of identical dominant OWT assignments based on satellite matchup data and convolution in-situ data, listed separately for the regional and global OWT cluster sets.

OWT cluster set	Dominant OWT matches
Regional	14,400 of 30,960
Global	6,500 of 30,960

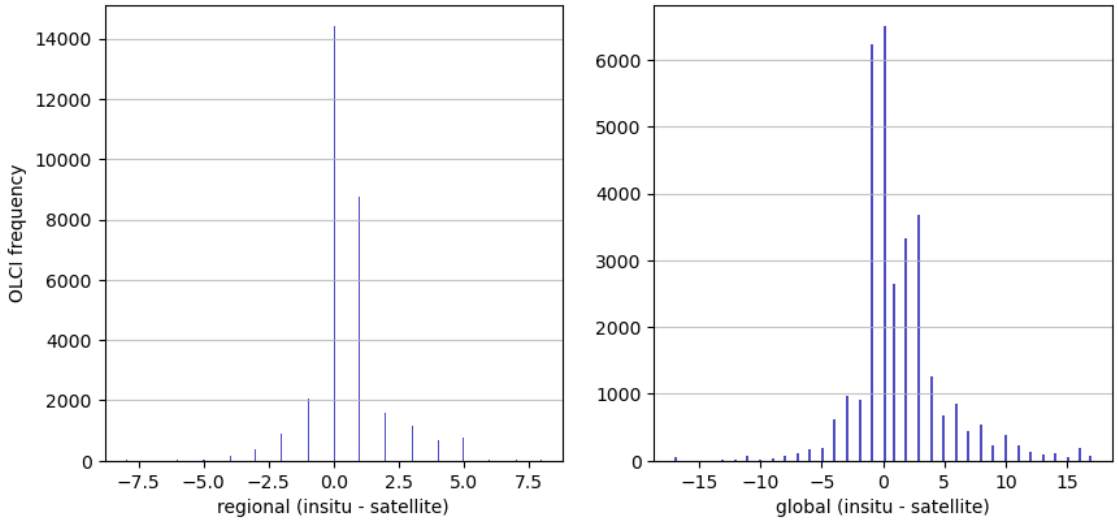

Figure 3: Difference in dominant OWT assigned by satellite as compared with that assigned based on convolved in-situ reflectance data. Cluster sets compared are regional (left) and global (right).

This suggests that using in-situ convolved data to assign OWT memberships would potentially introduce significant noise to the water type characterisations. On the other hand, basing characterisations on only a few data points invokes issues with small sample sizes from populations with high variability. Spectral reflectance plots for the regional cluster sets (Figures 4-9) and the global cluster set (Figure 10) also suggest that results from mixing convolved data OWT with those from satellite data should be taken with care. Thus, the decision is to present characterisations (§4 and §5) solely using dominant OWT from matchup data. Any additional

analysis using dominant OWT assignment from in-situ convolution should be treated as highly exploratory, and only used where satellite matchup data are not available

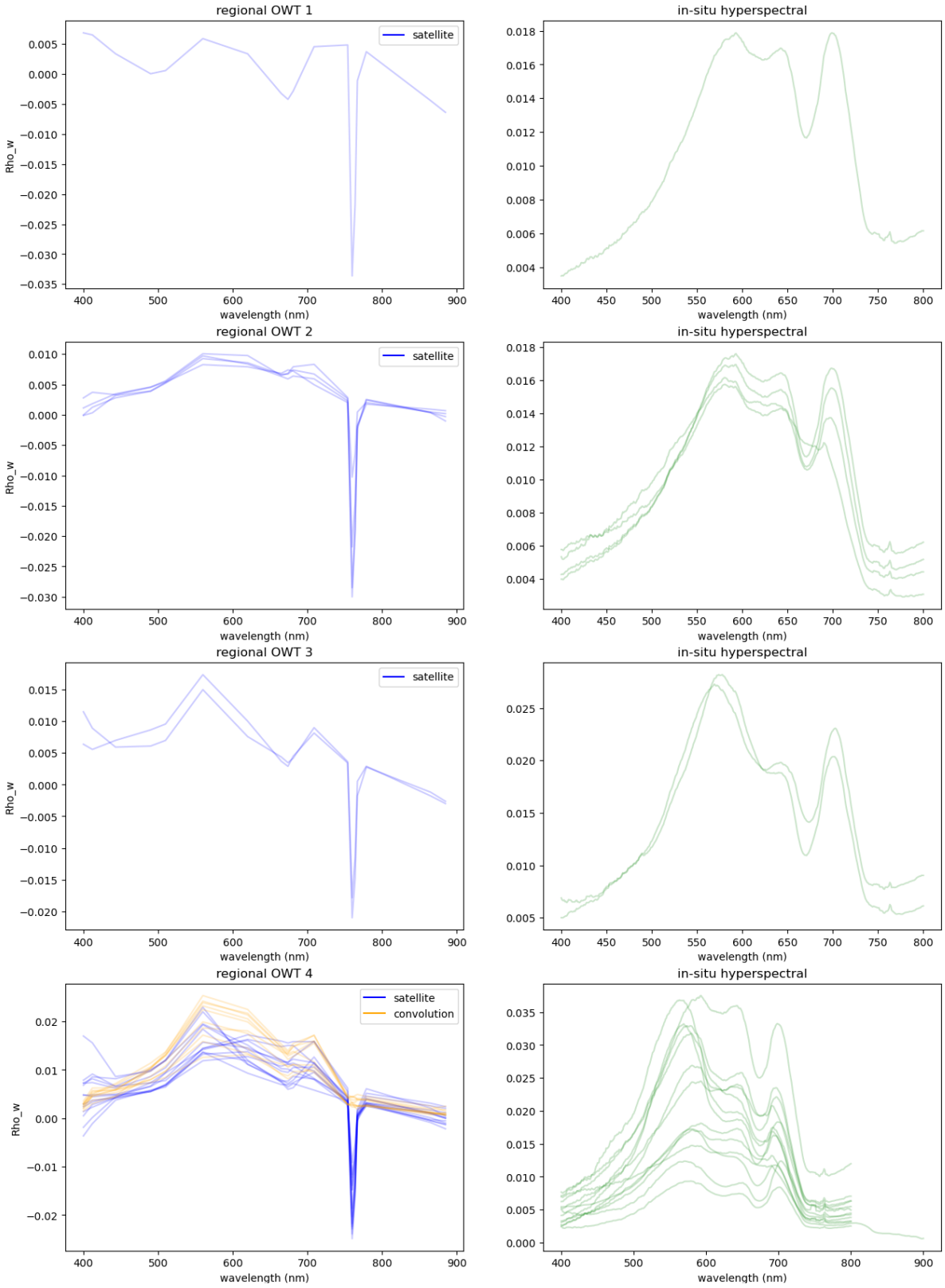
regional OWT 1
satellite
Rho_w
wavelength (nm)
in-situ hyperspectral
wavelength (nm)
regional OWT 2
satellite
Rho_w
wavelength (nm)
in-situ hyperspectral
wavelength (nm)
regional OWT 3
satellite
Rho_w
wavelength (nm)
in-situ hyperspectral
wavelength (nm)
regional OWT 4
satellite
convolution
Rho_w
wavelength (nm)
in-situ hyperspectral
wavelength (nm)

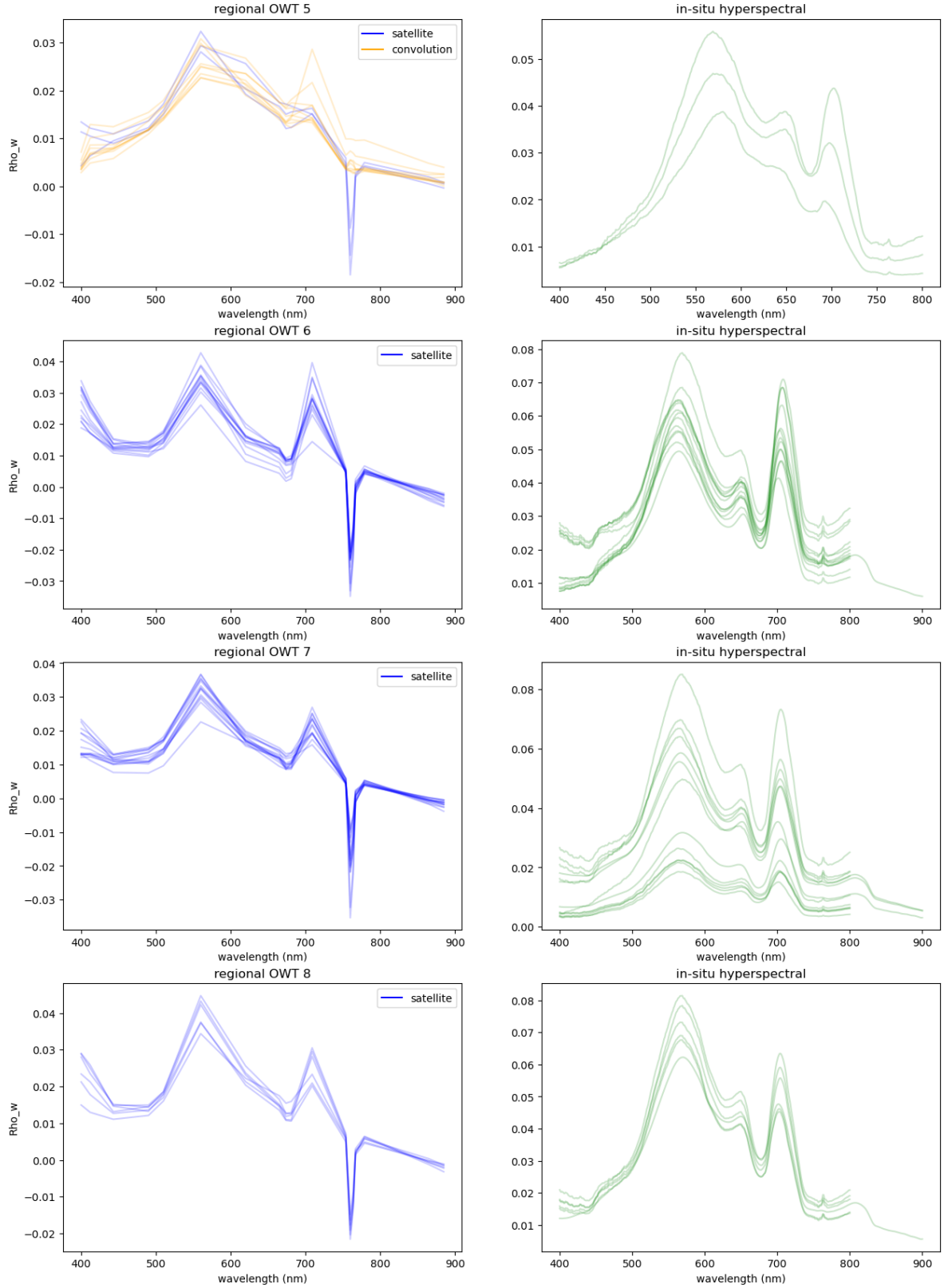
regional OWT 5
satellite
convolution
Rho_w
wavelength (nm)
in-situ hyperspectral
wavelength (nm)
regional OWT 6
satellite
Rho_w
wavelength (nm)
in-situ hyperspectral
wavelength (nm)
regional OWT 7
satellite
Rho_w
wavelength (nm)
in-situ hyperspectral
wavelength (nm)
regional OWT 8
satellite
Rho_w
wavelength (nm)
in-situ hyperspectral
wavelength (nm)

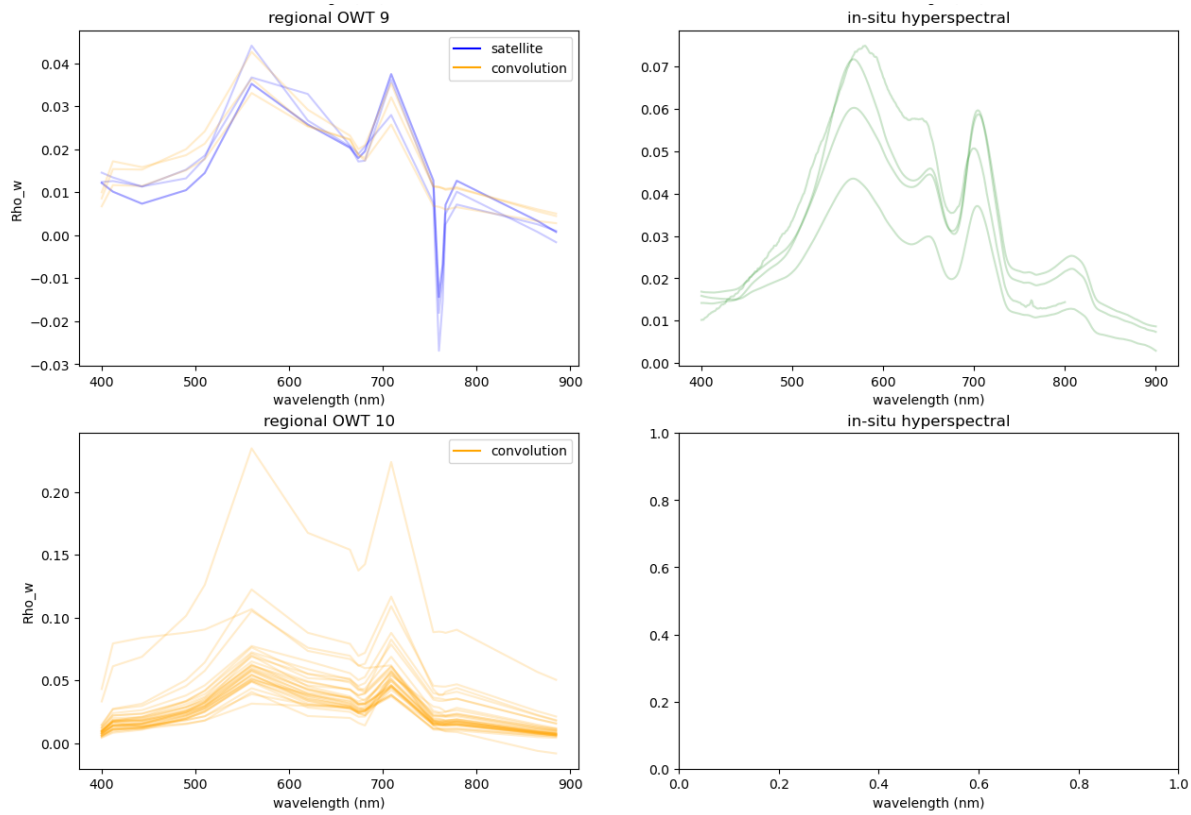

Figure 4: Curonian regional cluster set dominant OWT spectra, from both the satellite and convolved data (left column). Hyperspectral in-situ data from data points assigned that dominant OWT, based on the satellite signal, are shown in the right column.

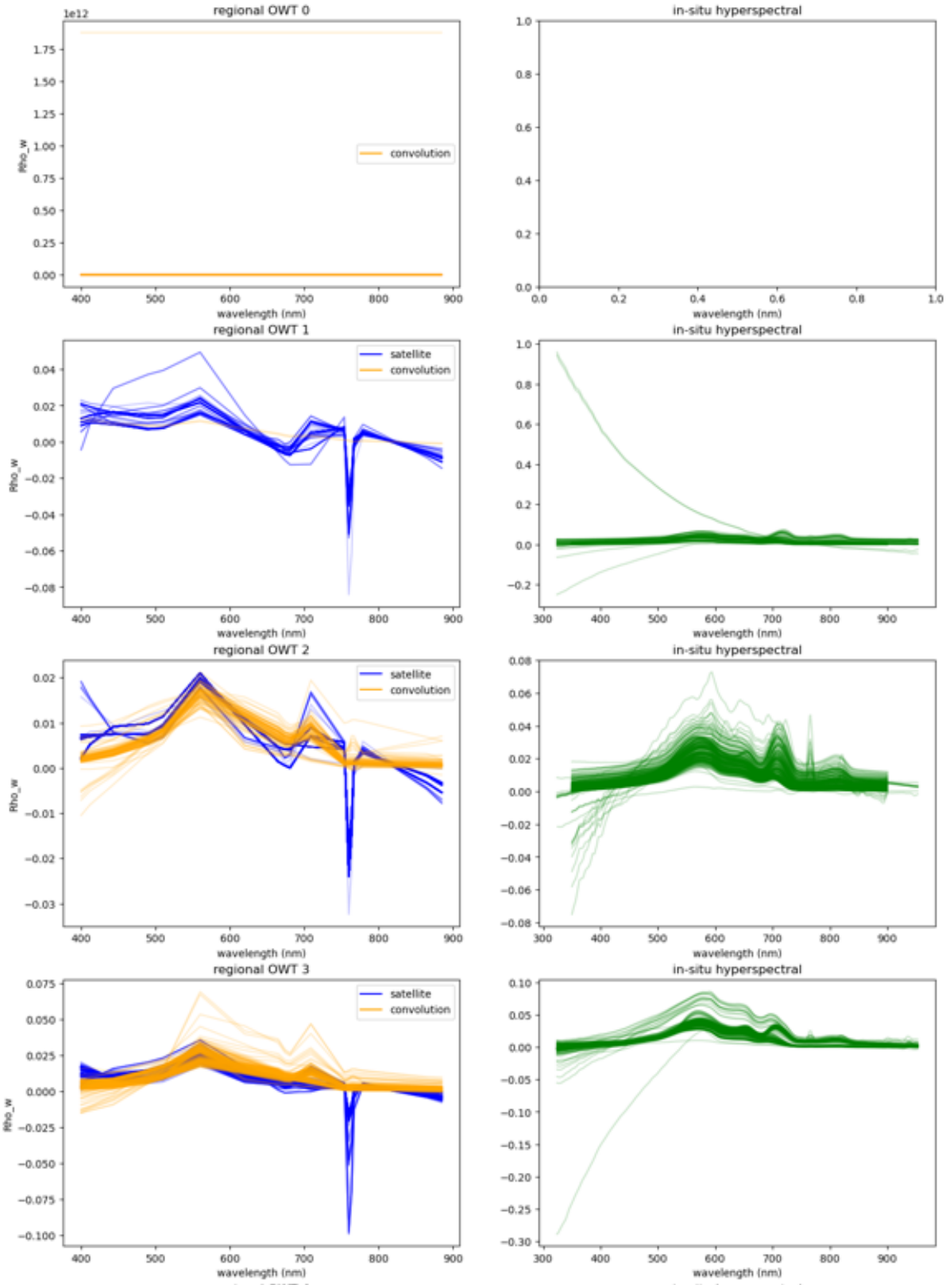
regional OWT 0
1e12
Rho_w
wavelength (nm)
convolution
in-situ hyperspectral
wavelength (nm)
regional OWT 1
satellite
convolution
Rho_w
wavelength (nm)
in-situ hyperspectral
wavelength (nm)
regional OWT 2
satellite
convolution
Rho_w
wavelength (nm)
in-situ hyperspectral
wavelength (nm)
regional OWT 3
satellite
convolution
Rho_w
wavelength (nm)
in-situ hyperspectral
wavelength (nm)

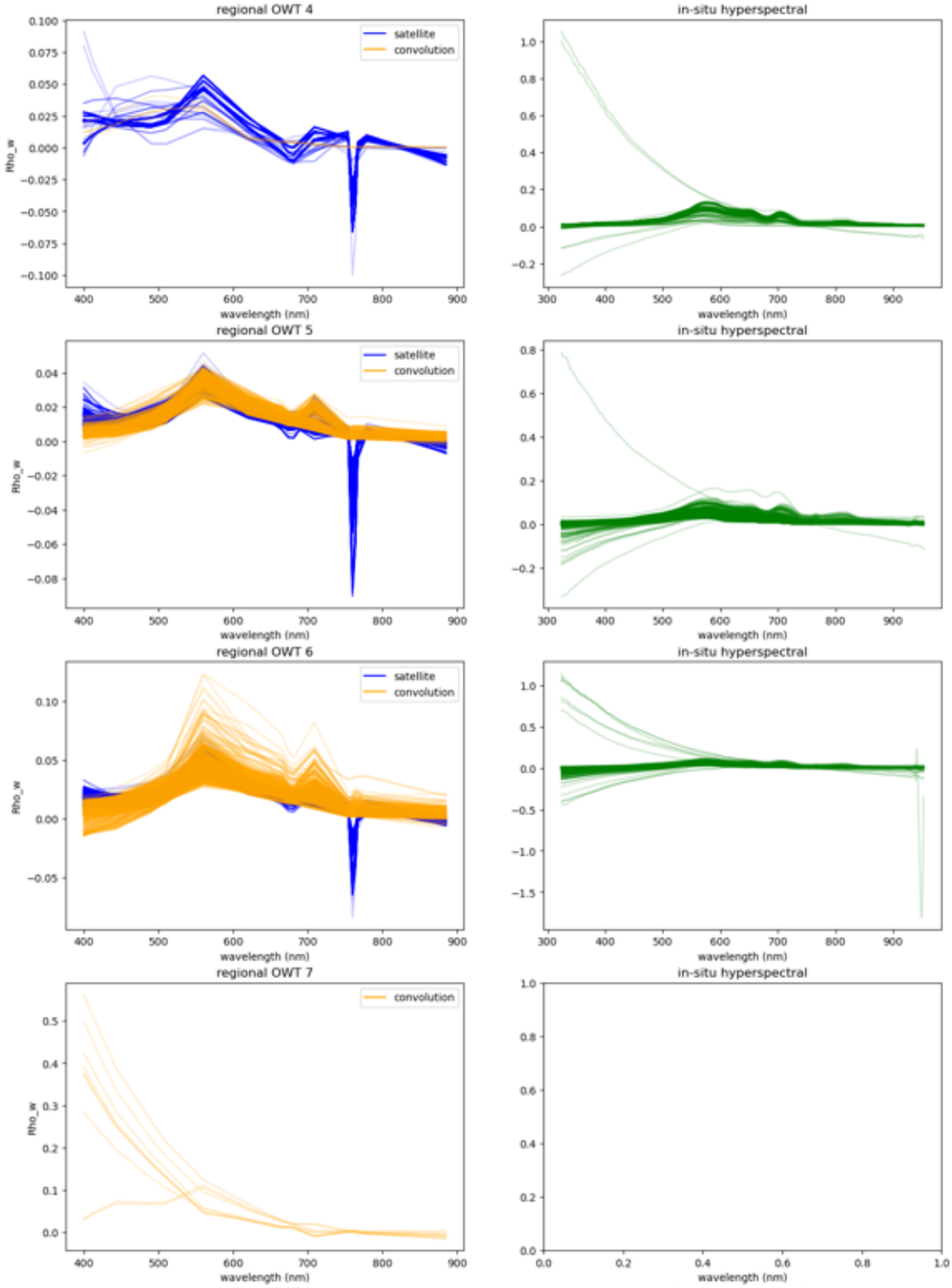
regional OWT 4
satellite
convolution
Rho_w
wavelength (nm)
in-situ hyperspectral
wavelength (nm)
regional OWT 5
satellite
convolution
Rho_w
wavelength (nm)
in-situ hyperspectral
wavelength (nm)
regional OWT 6
satellite
convolution
Rho_w
wavelength (nm)
in-situ hyperspectral
wavelength (nm)
regional OWT 7
convolution
Rho_w
wavelength (nm)
in-situ hyperspectral
wavelength (nm)

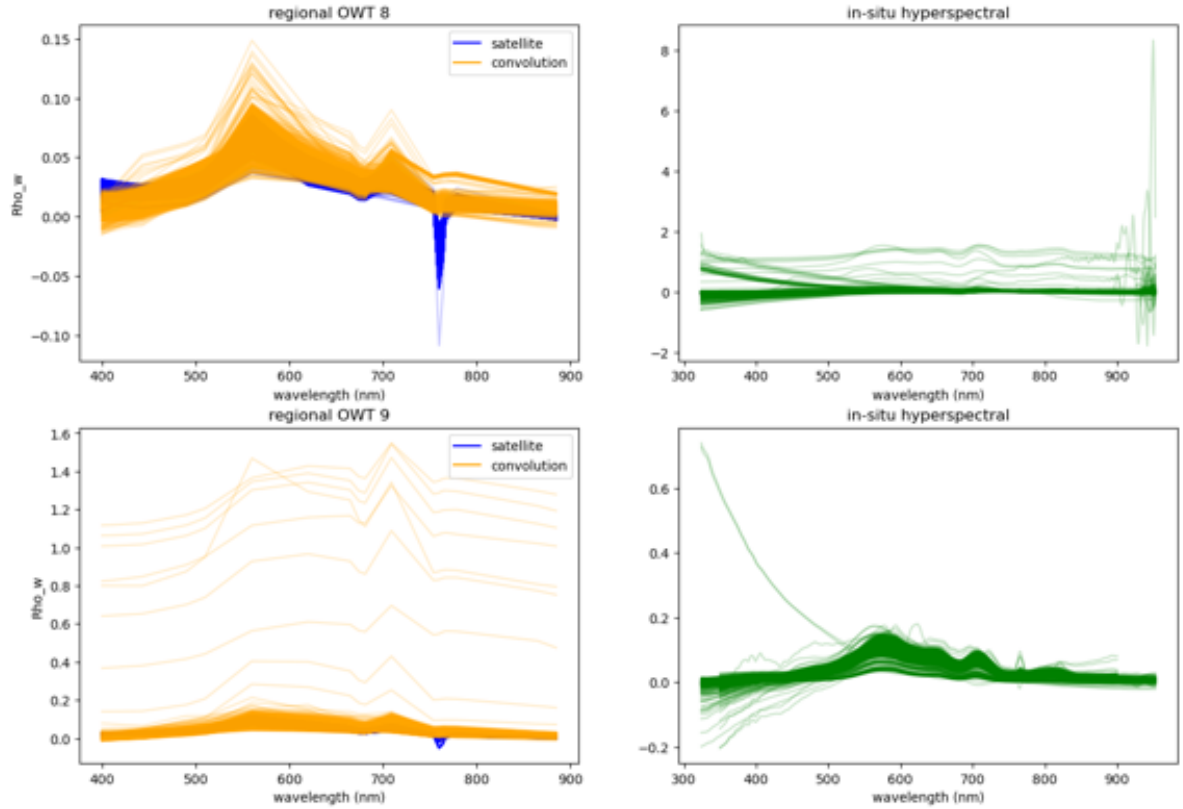

Figure 5: Danube Delta/Razelm-Sinoe Lake complex regional cluster set dominant OWT spectra, from both the satellite and convolved data (left column). Hyperspectral in-situ data from data points assigned that dominant OWT, based on the satellite signal, are shown in the right column.

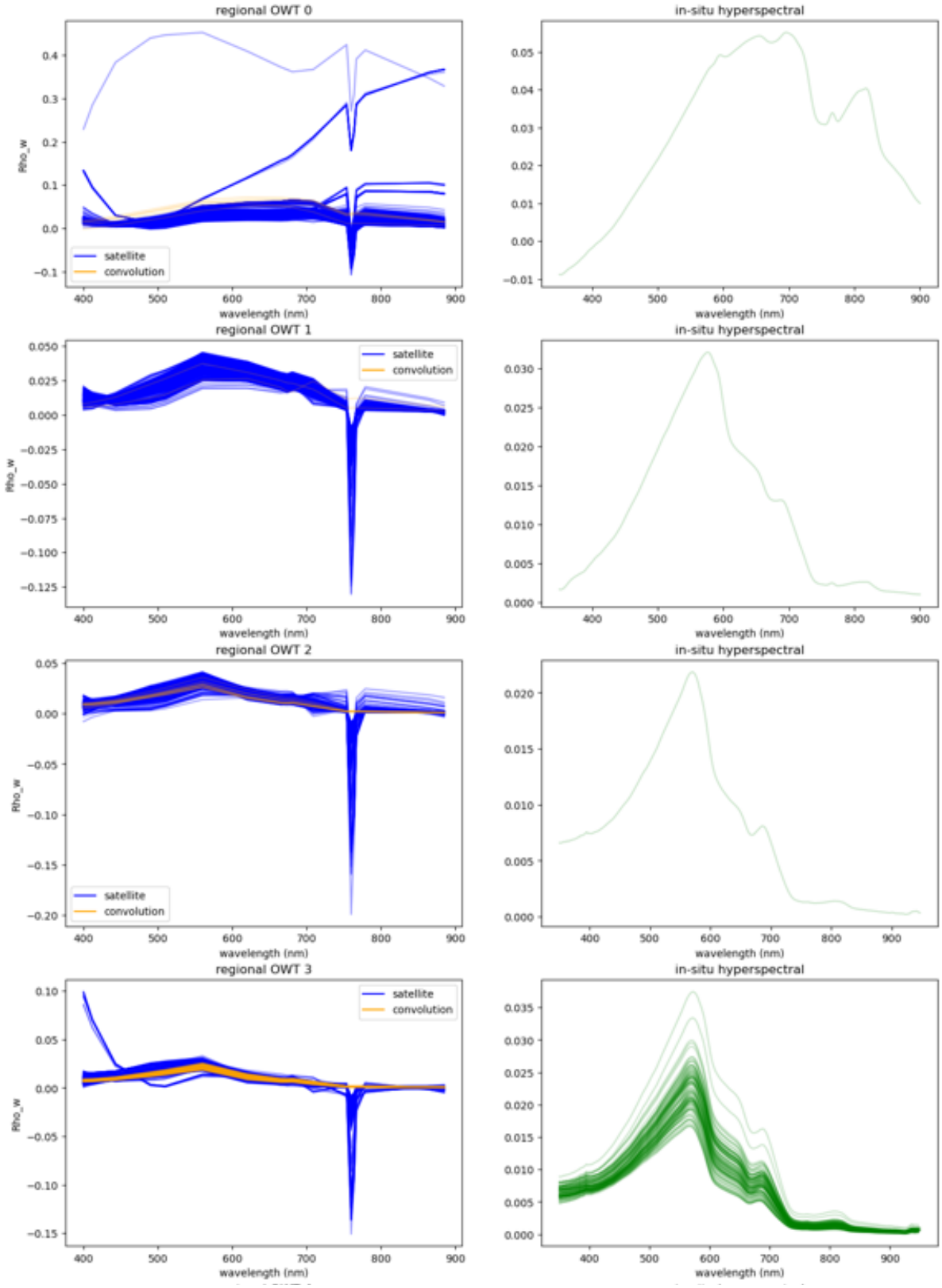
regional OWT 0
in-situ hyperspectral
regional OWT 1
in-situ hyperspectral
regional OWT 2
in-situ hyperspectral
regional OWT 3
in-situ hyperspectral
satellite
convolution
Rho_w
wavelength (nm)

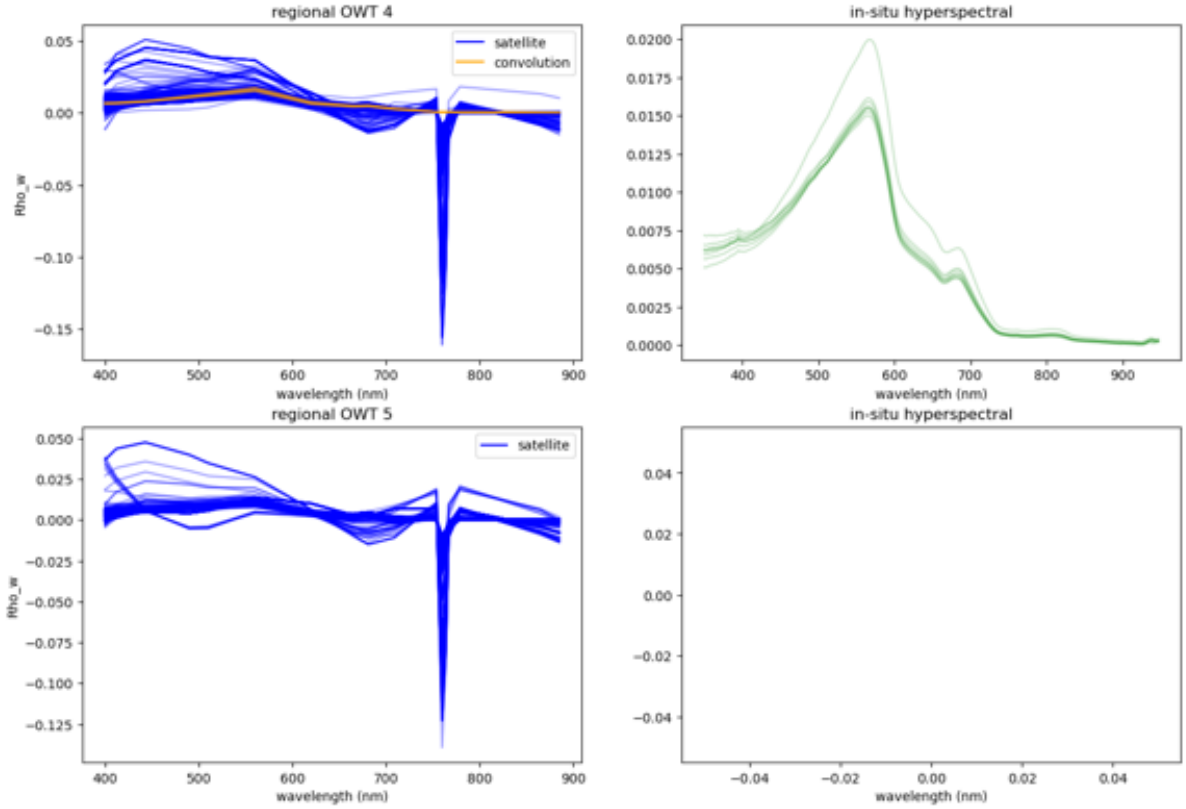

Figure 6: Elbe/German Bight regional cluster set dominant OWT spectra, from both the satellite and convolved data (left column). Hyperspectral in-situ data from data points assigned that dominant OWT, based on the satellite signal, are shown in the right column.

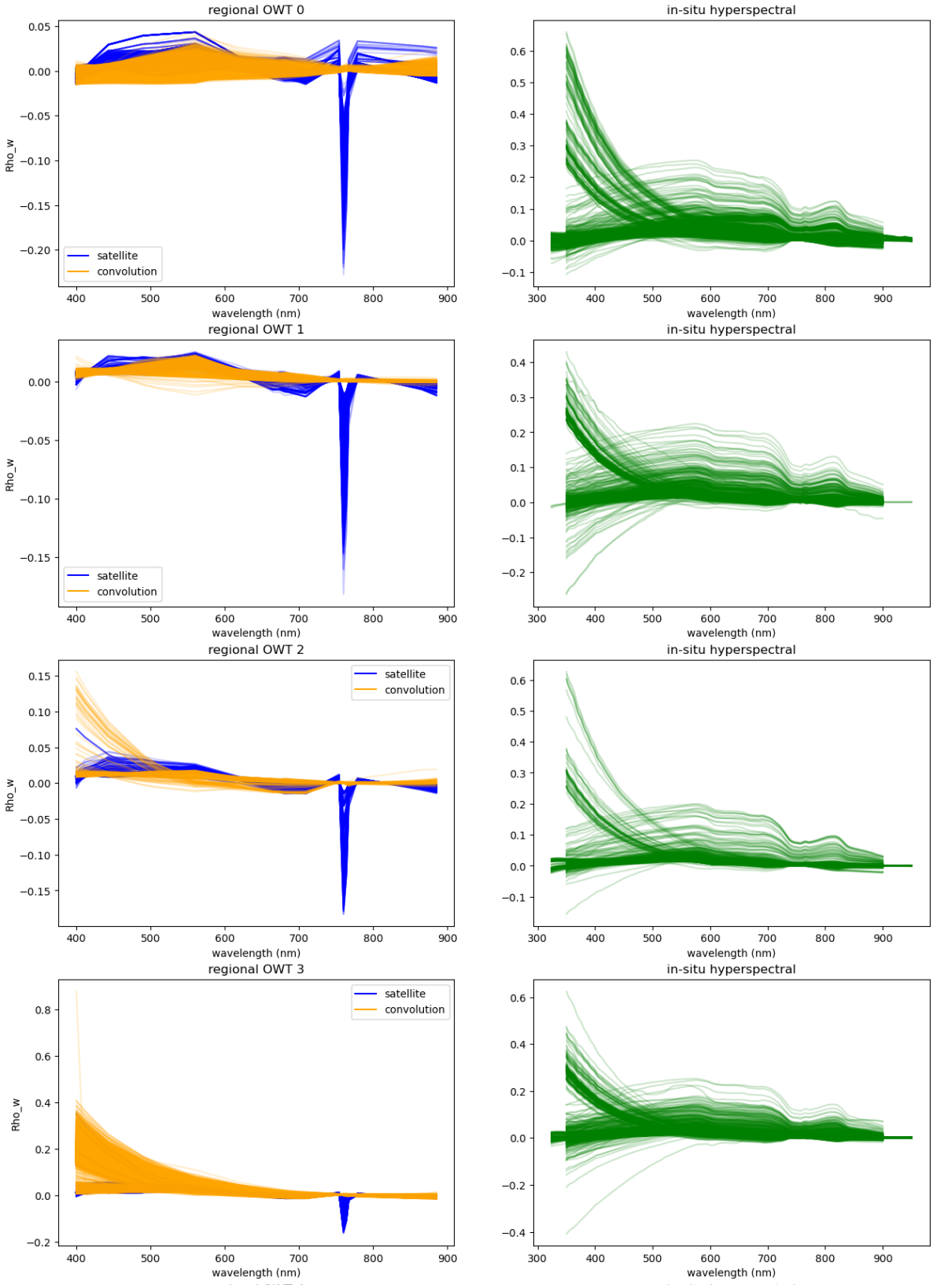
regional OWT 0
in-situ hyperspectral
regional OWT 1
in-situ hyperspectral
regional OWT 2
in-situ hyperspectral
regional OWT 3
in-situ hyperspectral
satellite
convolution
Rho_w
wavelength (nm)

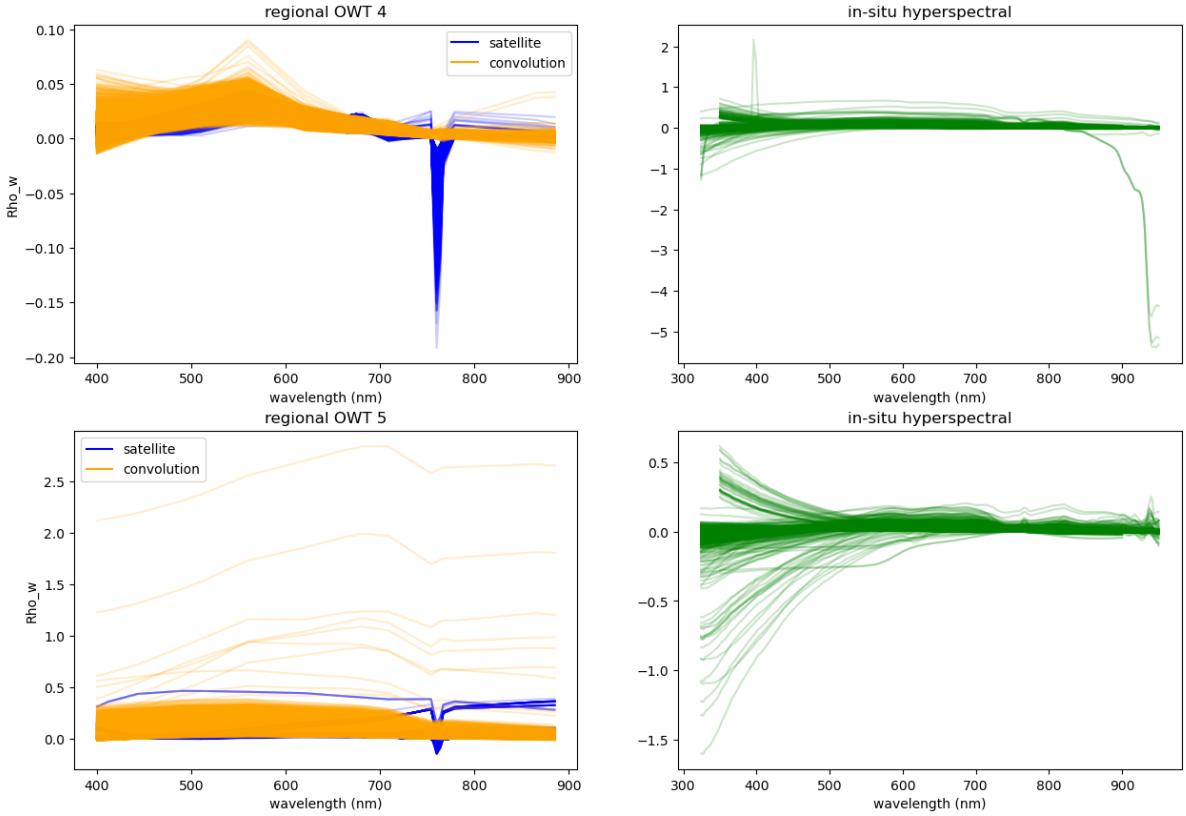

Figure 7: Tagus regional cluster set dominant OWT spectra, from both the satellite and convolved data (left column). Hyperspectral in-situ data from data points assigned that dominant OWT, based on the satellite signal, are shown in the right column.

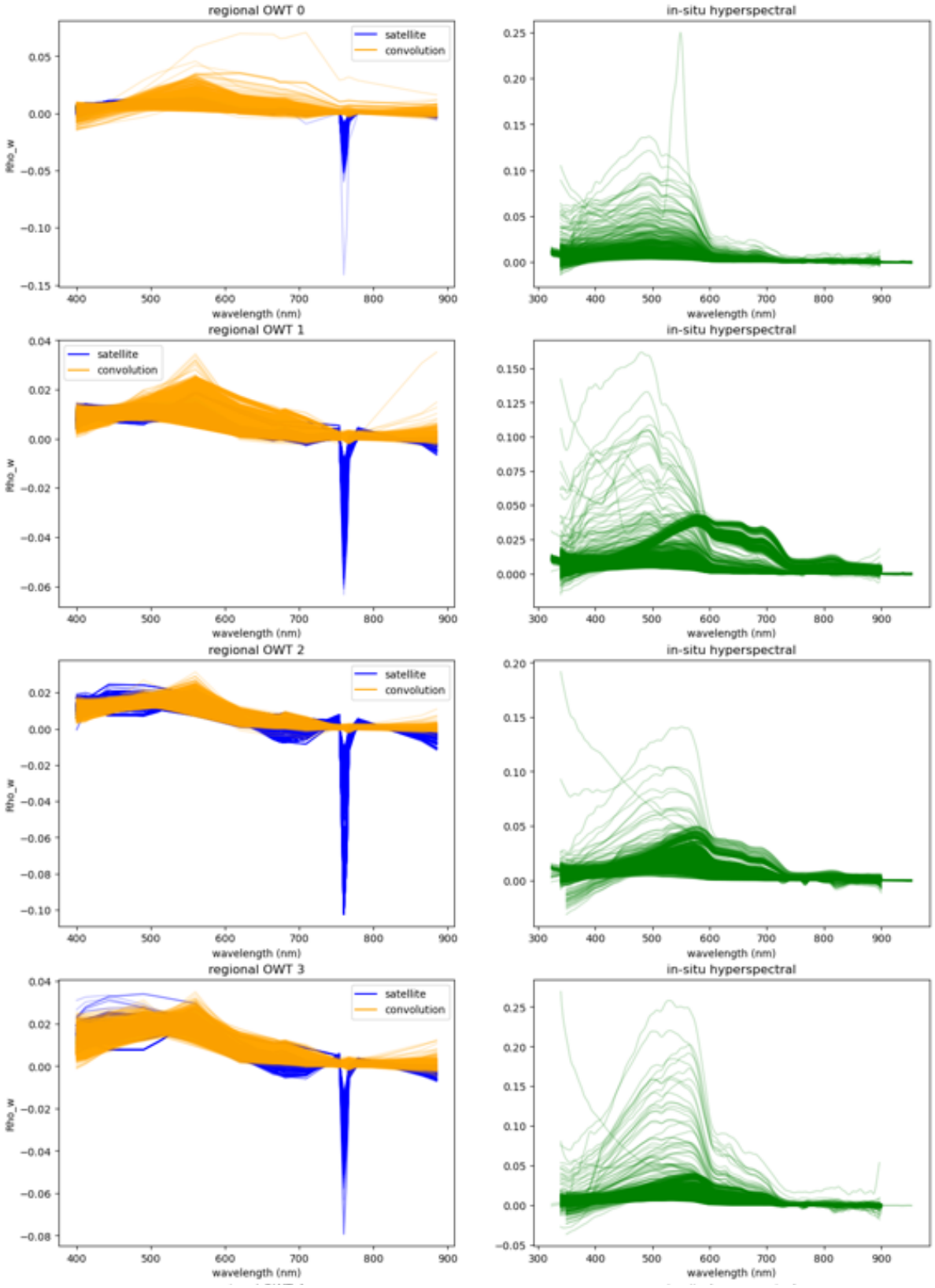
regional OWT 0
satellite
convolution
Rho_w
wavelength (nm)
in-situ hyperspectral
wavelength (nm)
regional OWT 1
satellite
convolution
Rho_w
wavelength (nm)
in-situ hyperspectral
wavelength (nm)
regional OWT 2
satellite
convolution
Rho_w
wavelength (nm)
in-situ hyperspectral
wavelength (nm)
regional OWT 3
satellite
convolution
Rho_w
wavelength (nm)
in-situ hyperspectral
wavelength (nm)

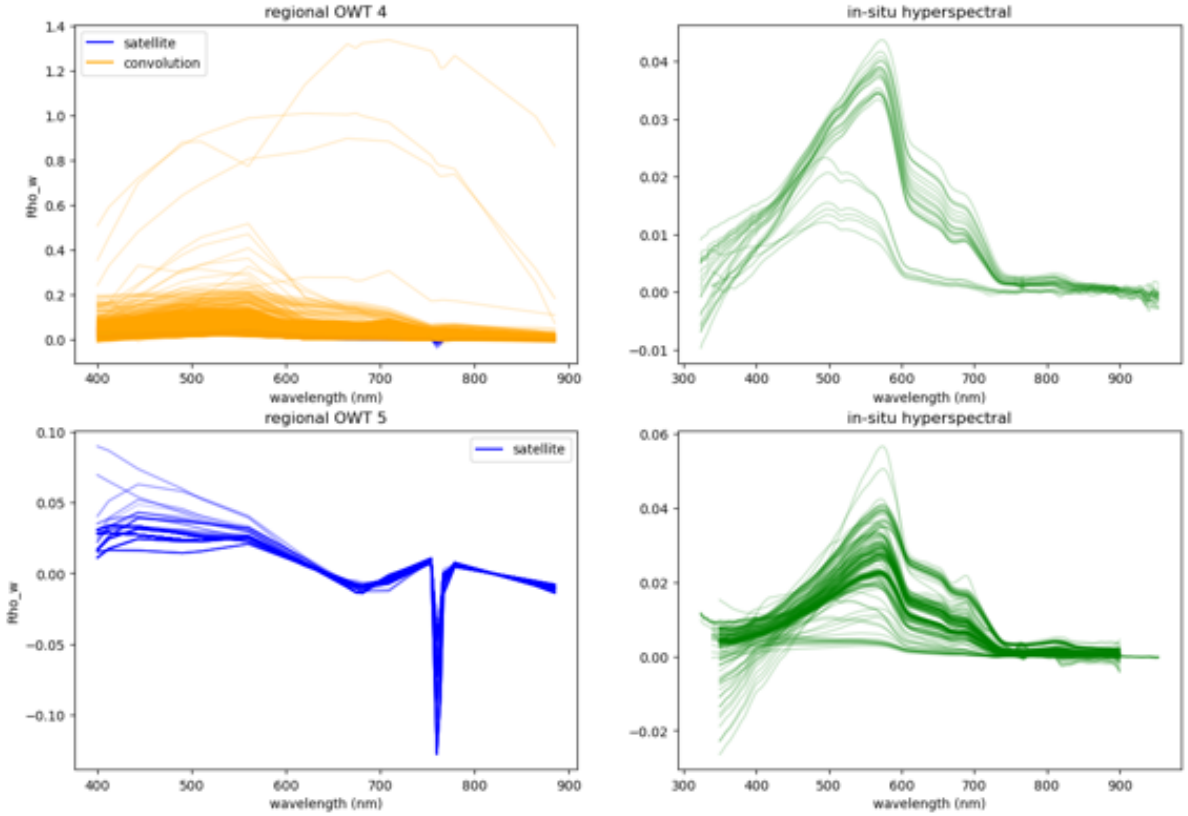

Figure 8: Tamar/Plymouth Sound regional cluster set dominant OWT spectra, from both the satellite and convolved data (left column). Hyperspectral in-situ data from data points assigned that dominant OWT, based on the satellite signal, are shown in the right column.

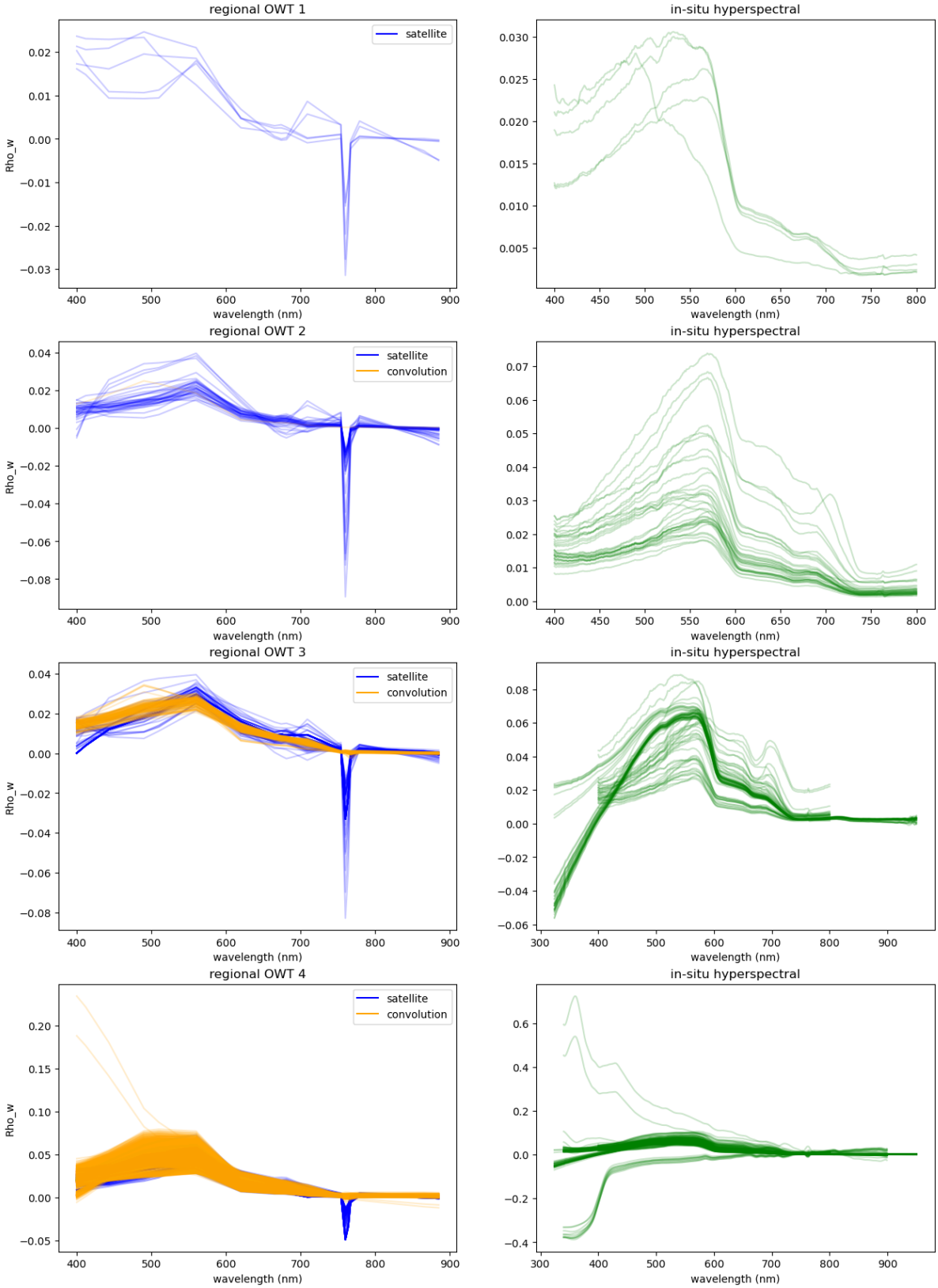
regional OWT 1
satellite
Rho_w
wavelength (nm)
in-situ hyperspectral
wavelength (nm)
regional OWT 2
satellite
convolution
Rho_w
wavelength (nm)
in-situ hyperspectral
wavelength (nm)
regional OWT 3
satellite
convolution
Rho_w
wavelength (nm)
in-situ hyperspectral
wavelength (nm)
regional OWT 4
satellite
convolution
Rho_w
wavelength (nm)
in-situ hyperspectral
wavelength (nm)

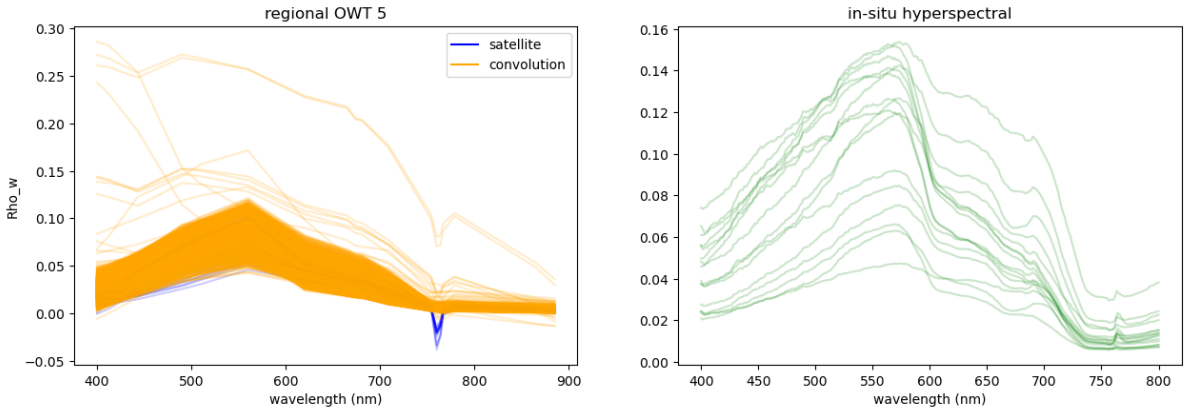

Figure 9: Venice/NW Adriatic regional cluster set dominant OWT spectra, from both the satellite and convolved data (left column). Hyperspectral in-situ data from data points assigned that dominant OWT, based on the satellite signal, are shown in the right column.

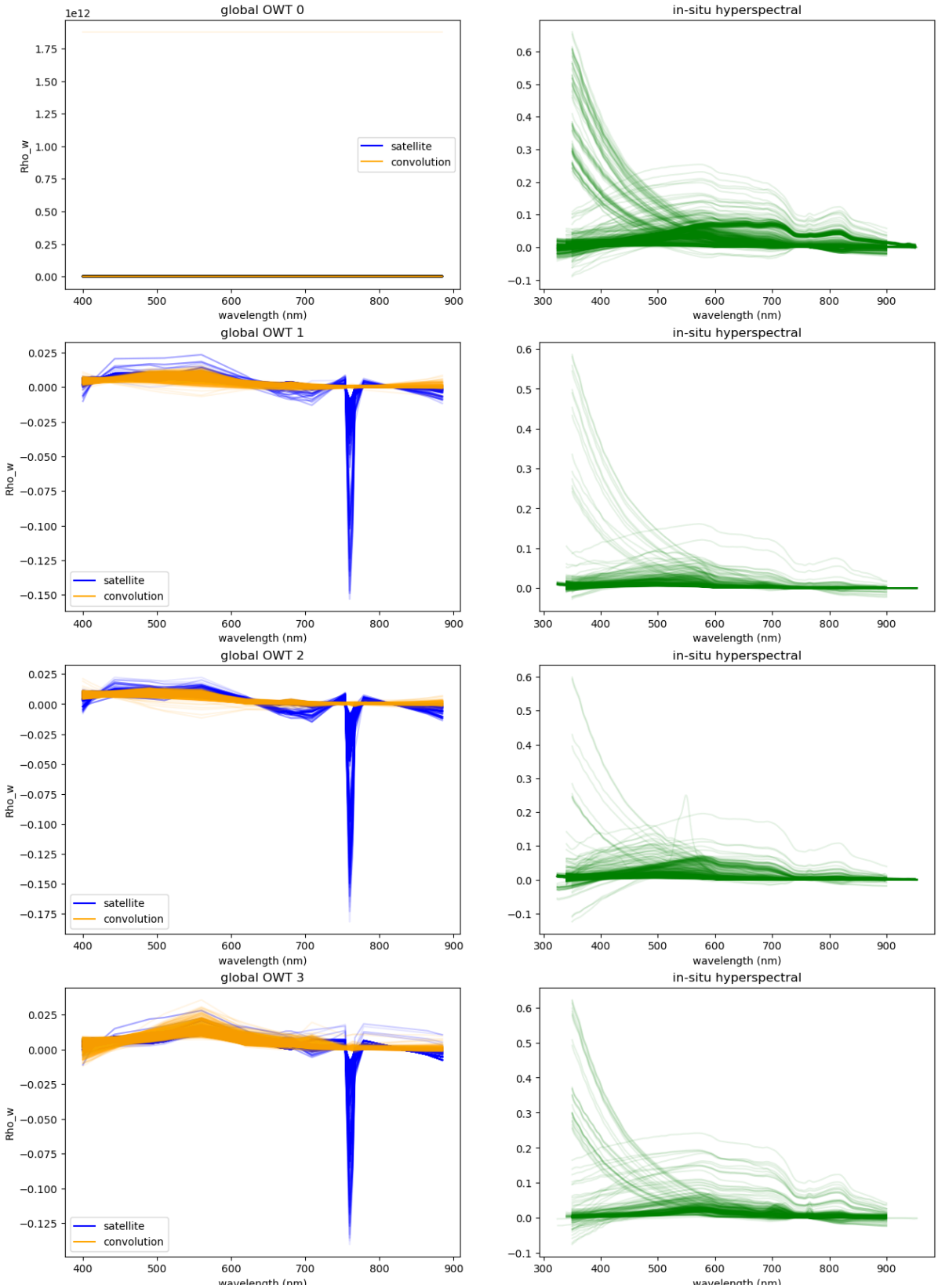
global OWT 0
in-situ hyperspectral
global OWT 1
in-situ hyperspectral
global OWT 2
in-situ hyperspectral
global OWT 3
in-situ hyperspectral
Rho_w
wavelength (nm)
satellite
convolution
1e12

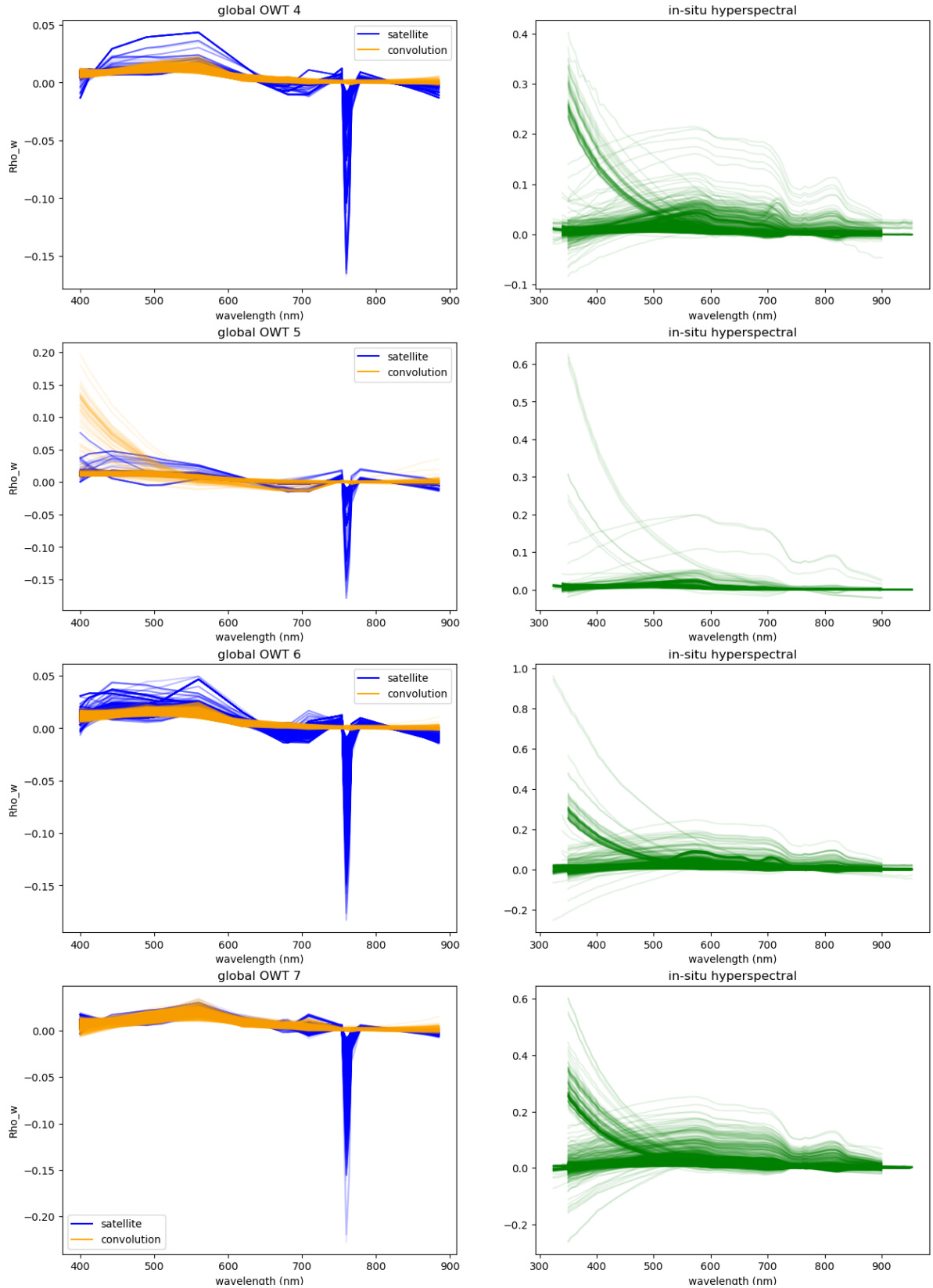
global OWT 4
in-situ hyperspectral
global OWT 5
in-situ hyperspectral
global OWT 6
in-situ hyperspectral
global OWT 7
in-situ hyperspectral
satellite
convolution
Rho_w
wavelength (nm)

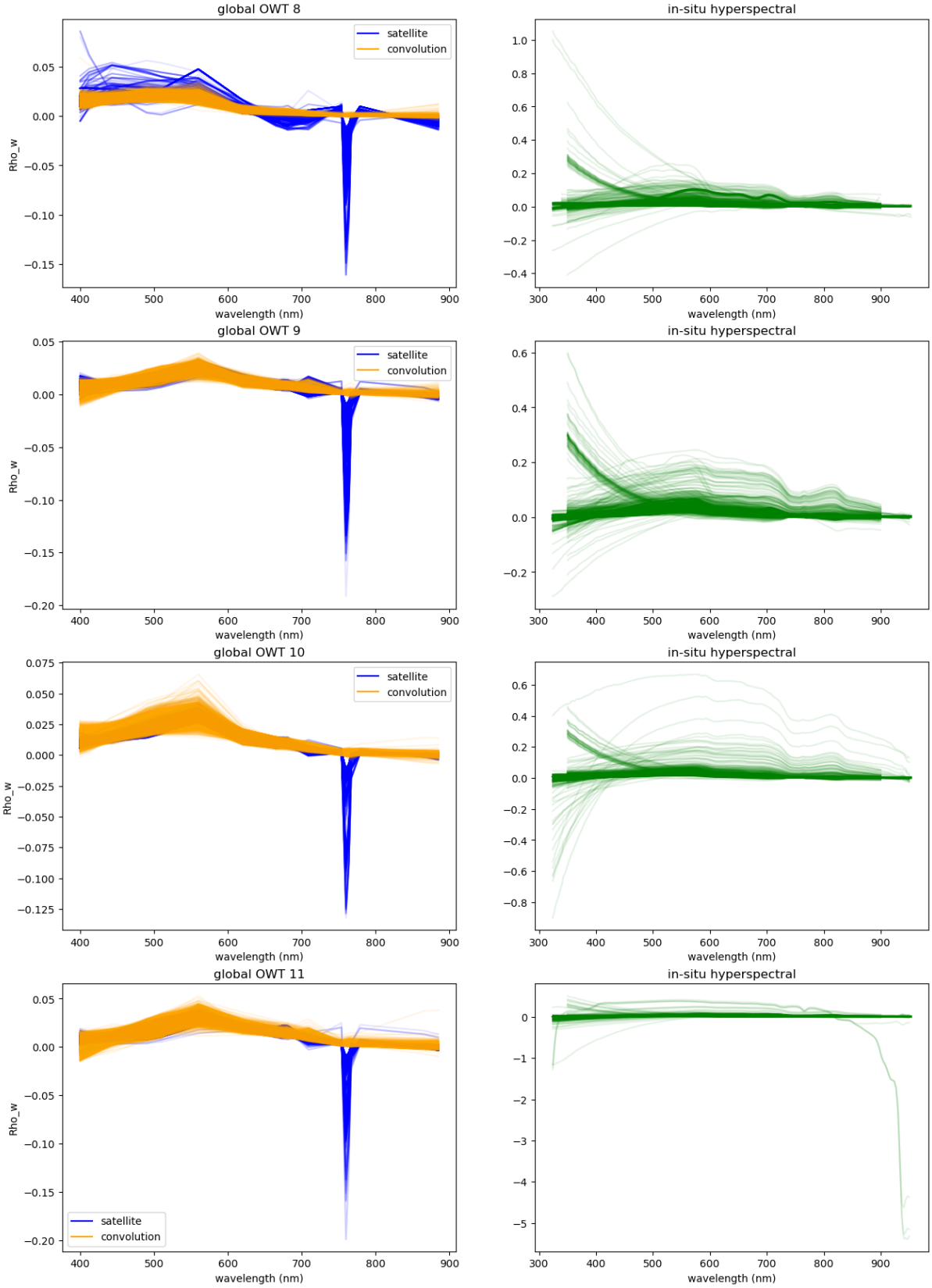
global OWT 8
in-situ hyperspectral
global OWT 9
in-situ hyperspectral
global OWT 10
in-situ hyperspectral
global OWT 11
in-situ hyperspectral
satellite
convolution
Rho_w
wavelength (nm)

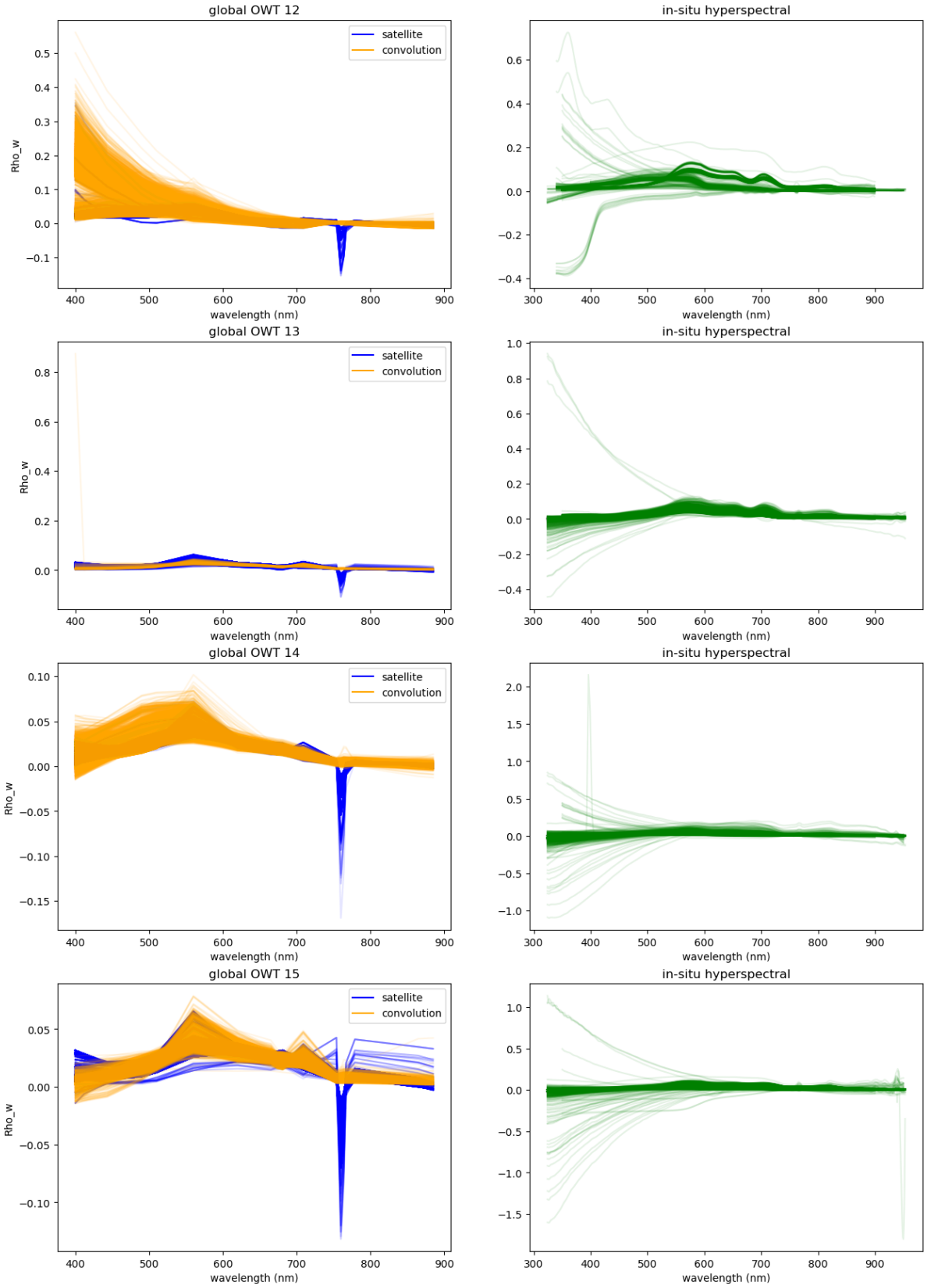
global OWT 12
in-situ hyperspectral
global OWT 13
in-situ hyperspectral
global OWT 14
in-situ hyperspectral
global OWT 15
in-situ hyperspectral
satellite
convolution
Rho_w
wavelength (nm)

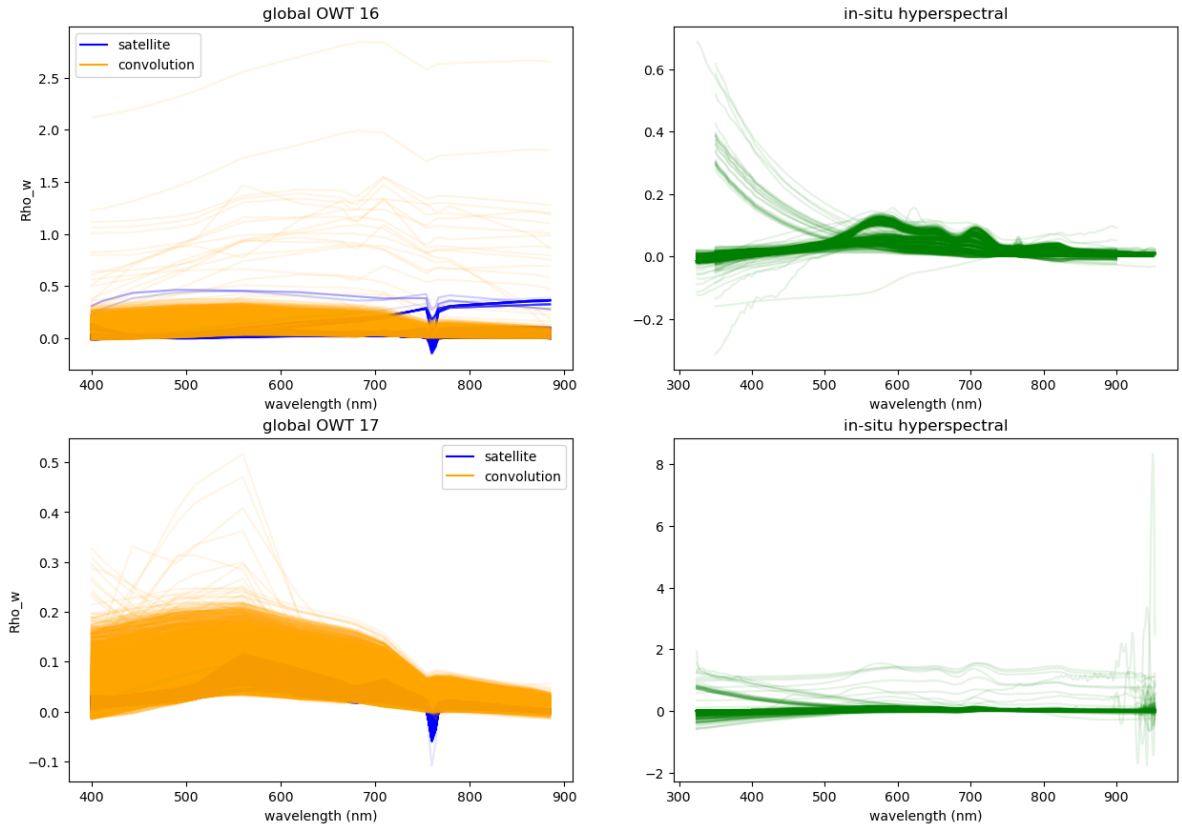

Figure 10: Global cluster set dominant OWT spectra, from both the satellite and convolved data (left column). Hyperspectral in-situ data from data points assigned that dominant OWT, based on the satellite signal, are shown in the right column.

3.2 Band-specific assessment

A precursor assessment of OWT cluster-specific atmospheric correction errors involved studying algorithm performance for matchup data between satellite L3 data and in-situ hyperspectral field data convolved to match the satellite sensor. A more in-depth assessment will be covered by WP5 activities. Comparisons of rho_w for each band, across global OWT clusters is presented in Figure 11.

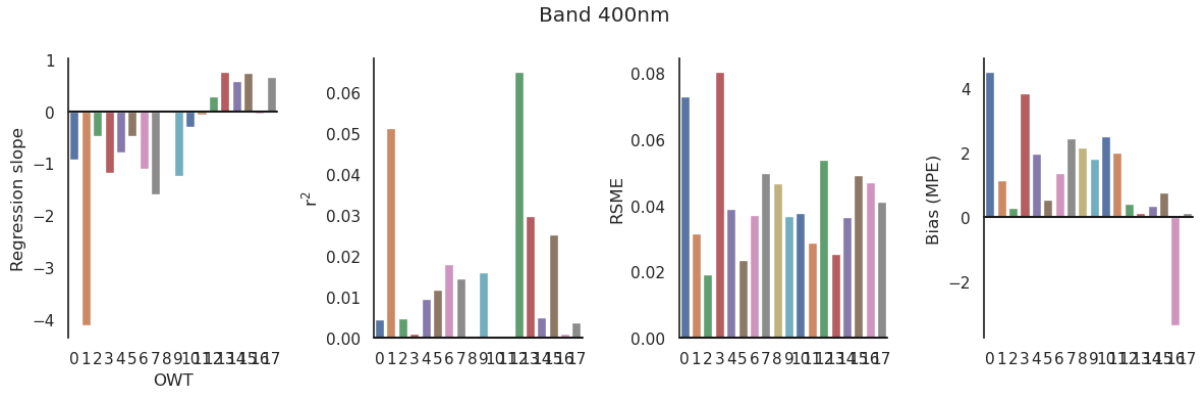

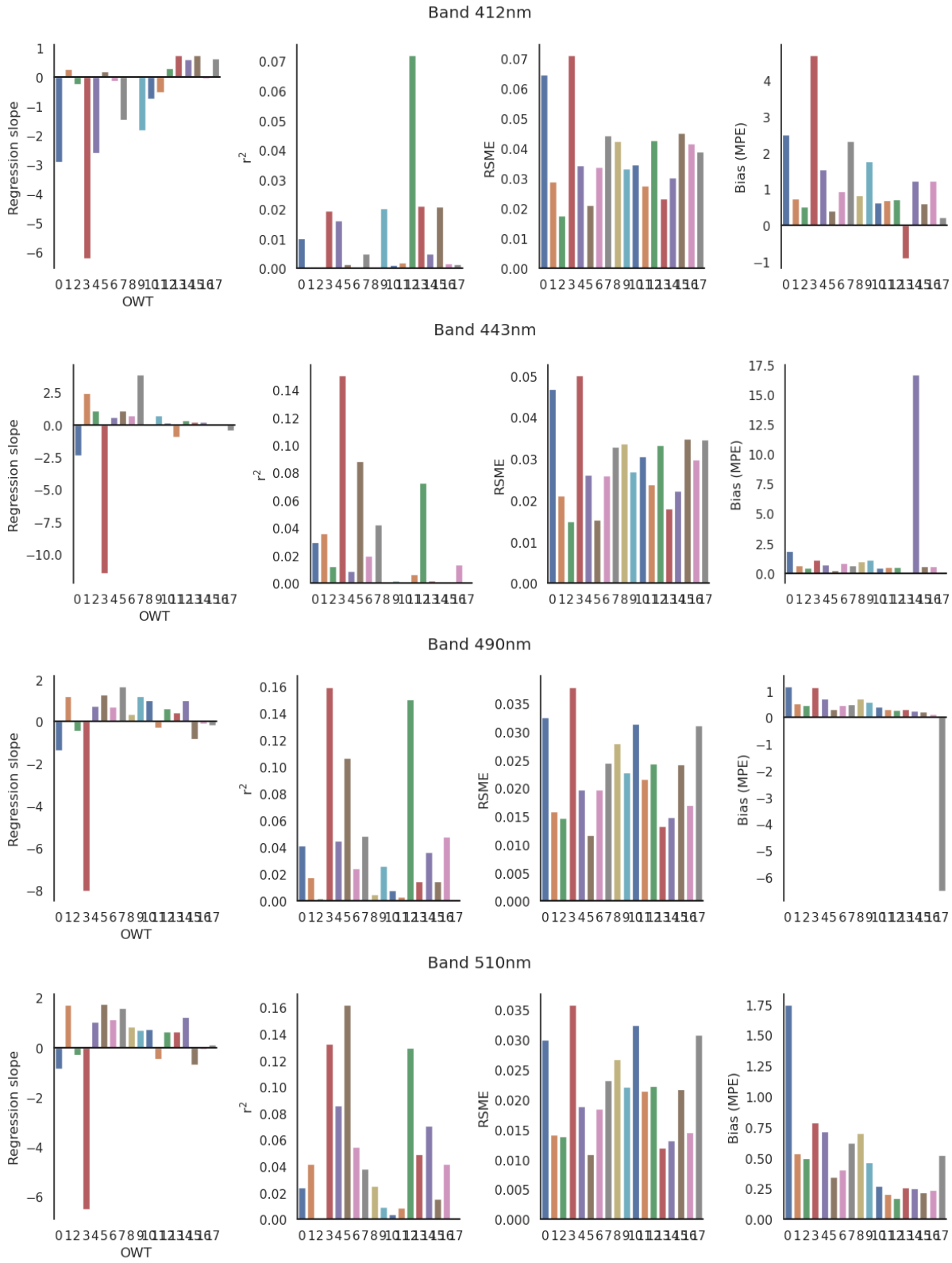
Band 412nm
Band 443nm
Band 490nm
Band 510nm
Regression slope
r²
RSME
Bias (MPE)
OWT

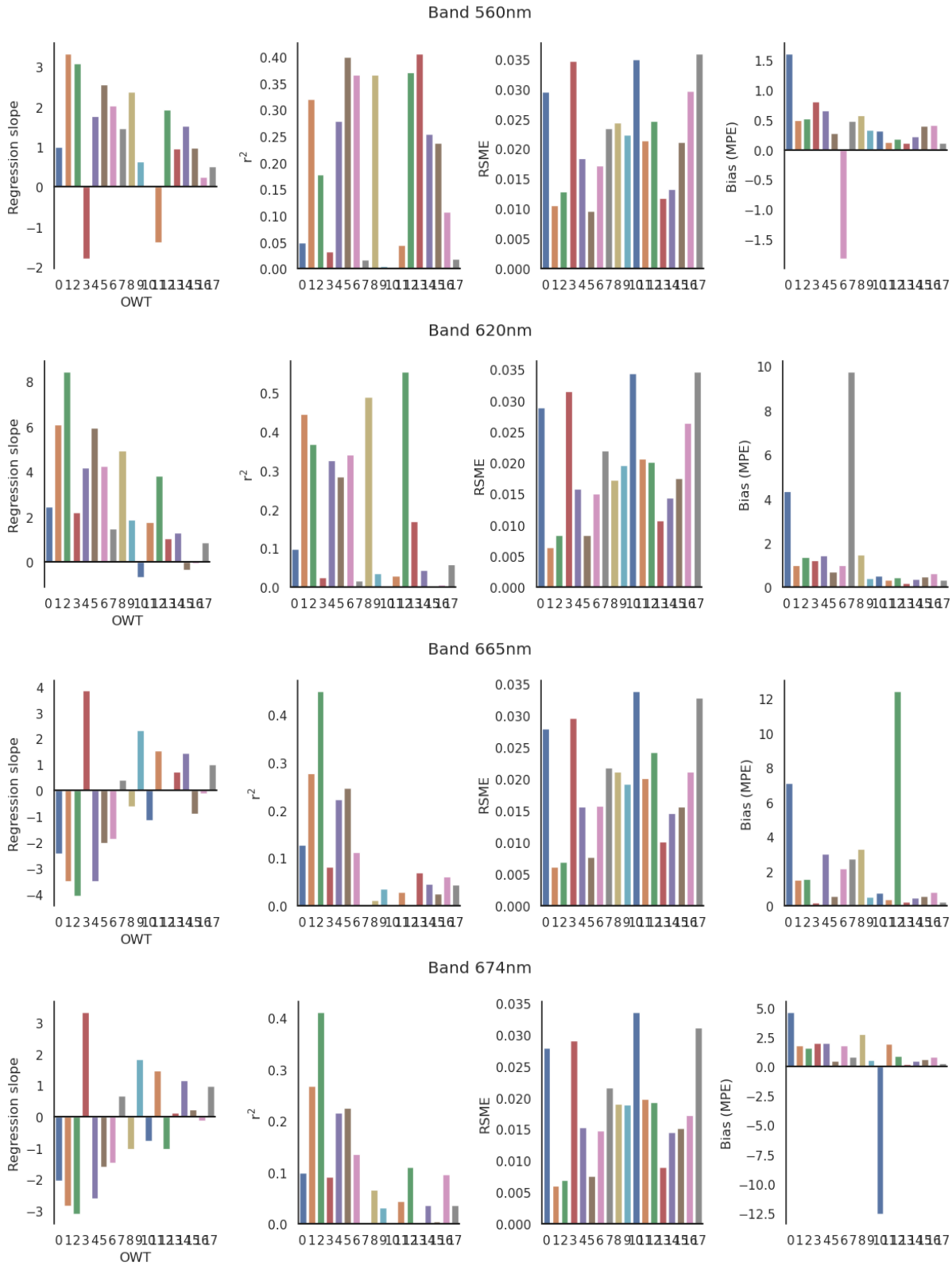
Band 560nm
Band 620nm
Band 665nm
Band 674nm
Regression slope
r²
RSME
Bias (MPE)
OWT

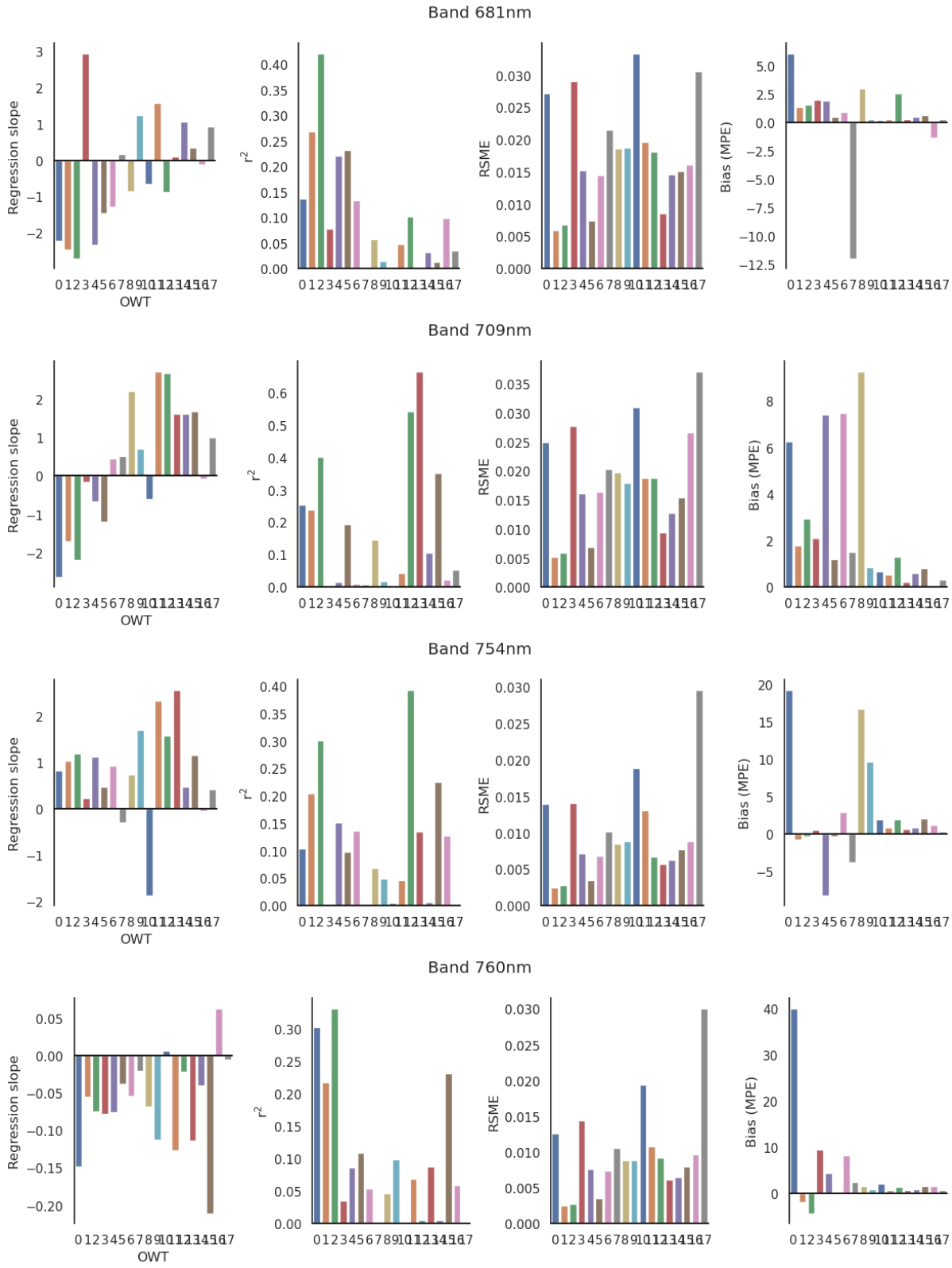
Band 681nm
Band 709nm
Band 754nm
Band 760nm
Regression slope
r²
RSME
Bias (MPE)
OWT

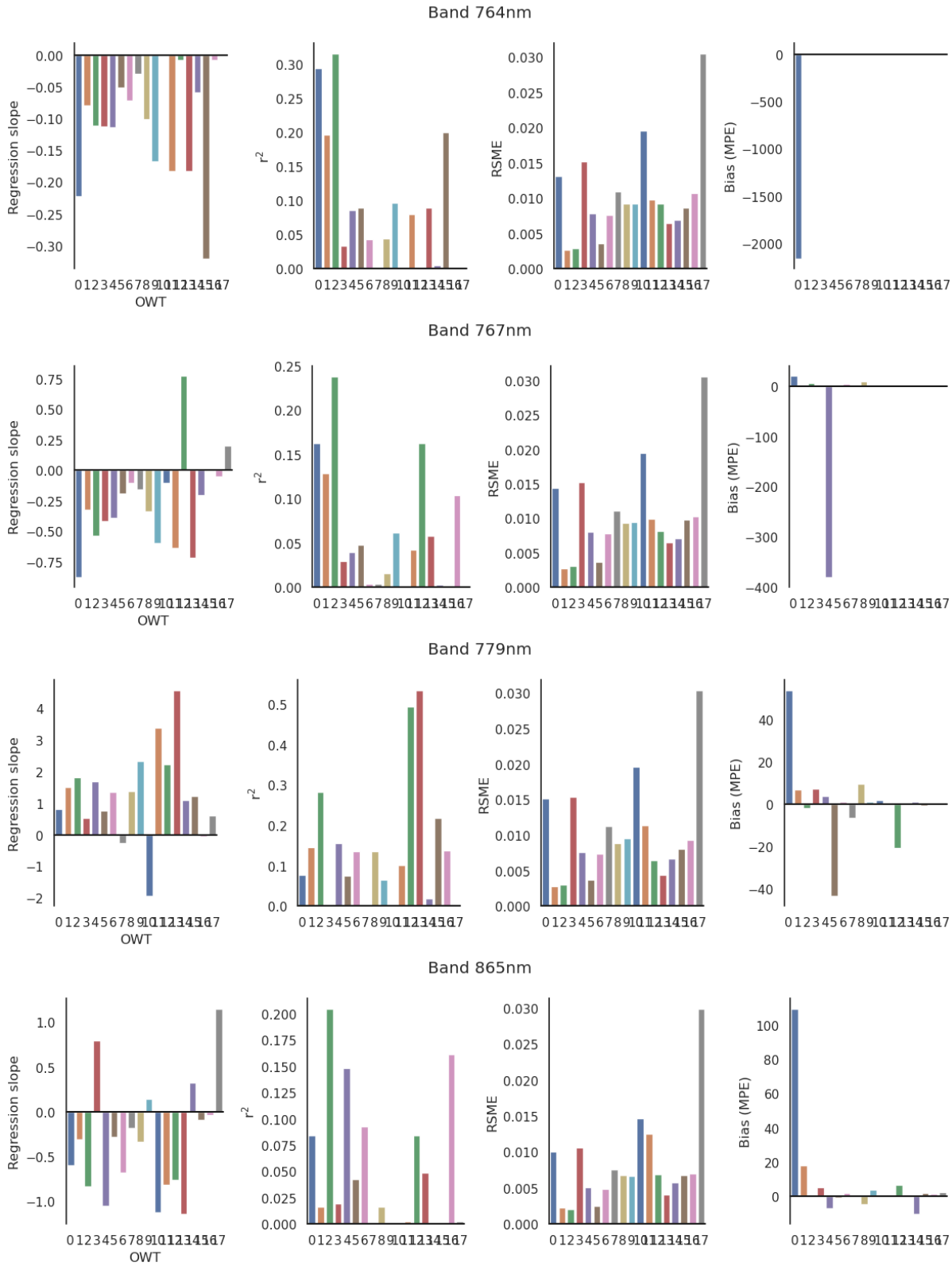
Band 764nm
Band 767nm
Band 779nm
Band 865nm
Regression slope
r²
RSME
Bias (MPE)
OWT

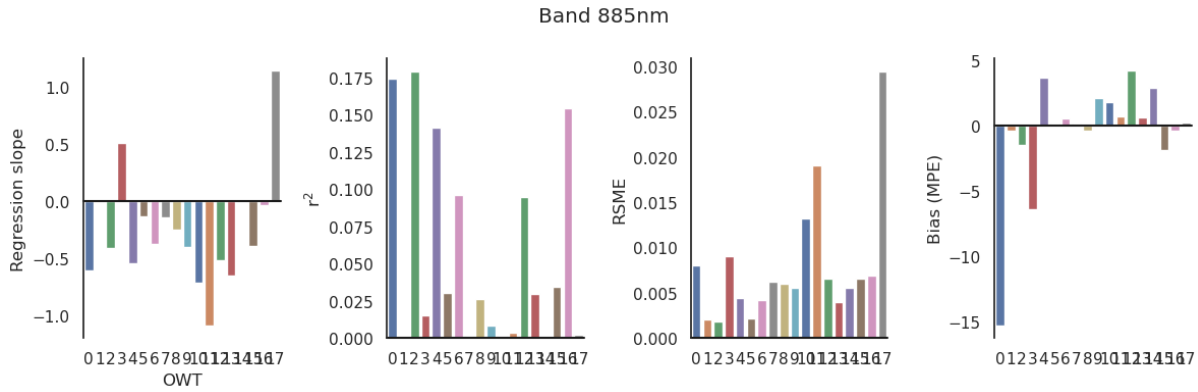

Figure 11: Remote sensing reflectance (Rrs) band-specific matchup statistics for global cluster set, including regression slope (ideally 1.0), coefficient of determination (r^2), root mean square error (RSME), and bias (represented by mean percentage error, MPE).

4 Regional cluster set characterisation

4.1 Biogeochemical parameters

Characterisation of the biogeochemical properties of the regional OWT classes are presented in Figure 12. All boxplots feature generally increasing values of chl-a and SPM with increasing OWT class number (which correspond to higher overall reflecting waters), a pattern which appears to be reversed for CDOM. The Curonian site was examined separately due to higher relative values compared to the other sites (Figure 13). This suggests that for the Curonian site, increasing trends in chl-a and SPM happen over two sets of reginal OWT classes, namely regional OWT classes {4, 5, 6} and {7, 8, 9}. Plotting the remaining four sites (Figure 14) suggests this same pattern for SPM in the Tagus regional OWT set.

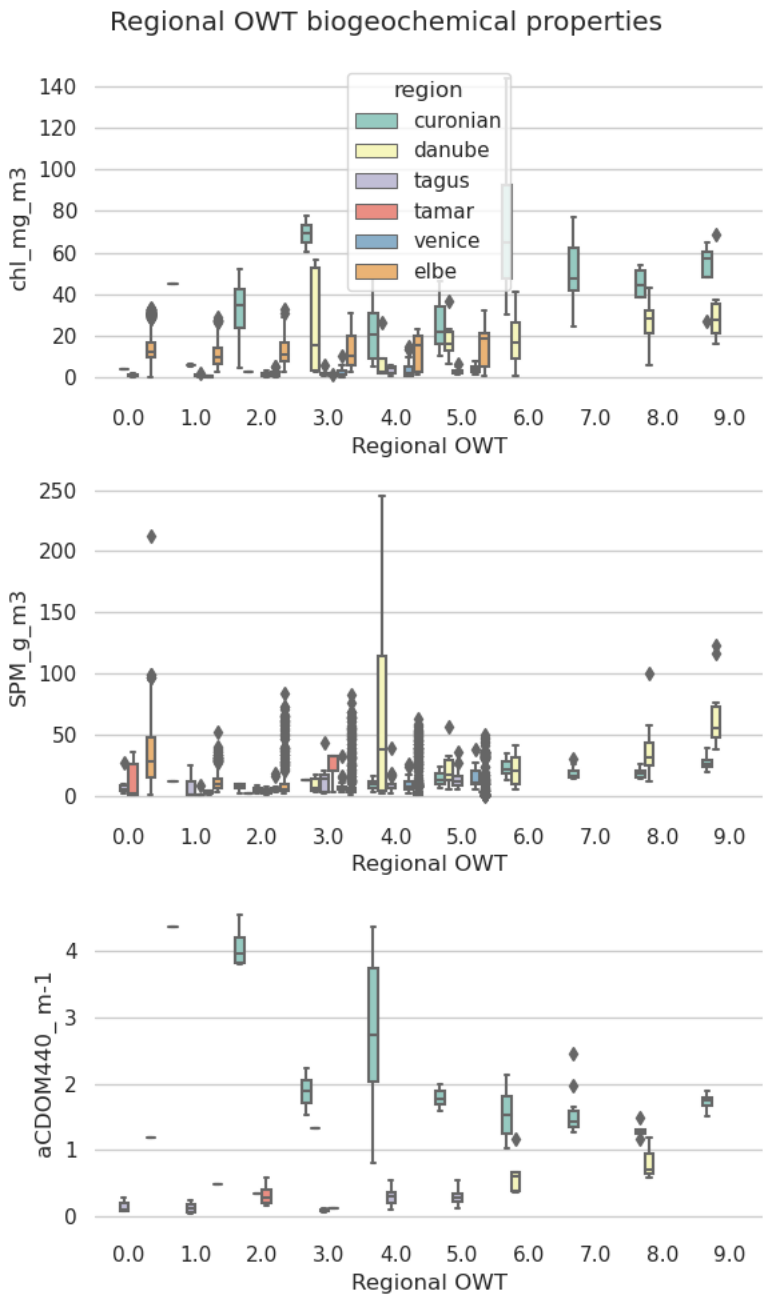

Figure 12: Biogeochemical properties (chlorophyll-a, suspended particulate matter, coloured dissolved organic matter) of regional OWT cluster sets.

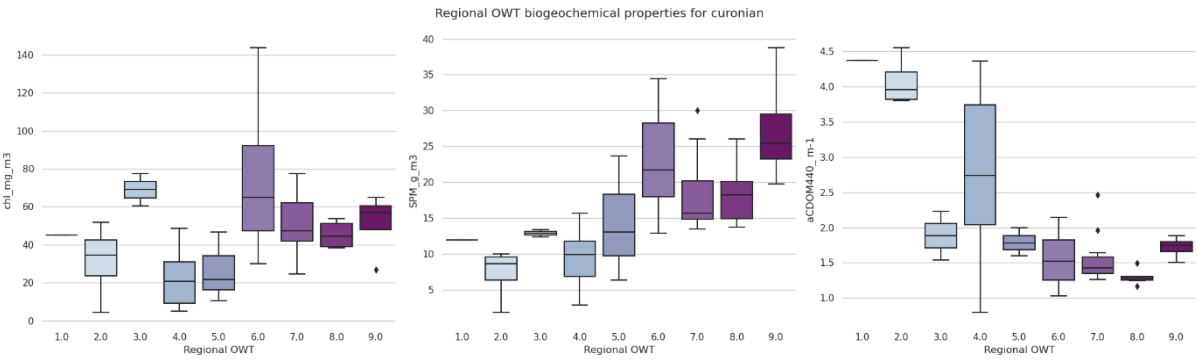

Figure 13: Biogeochemical properties (chlorophyll-a, suspended particulate matter, coloured dissolved organic matter) of the Curonian regional OWT cluster set.

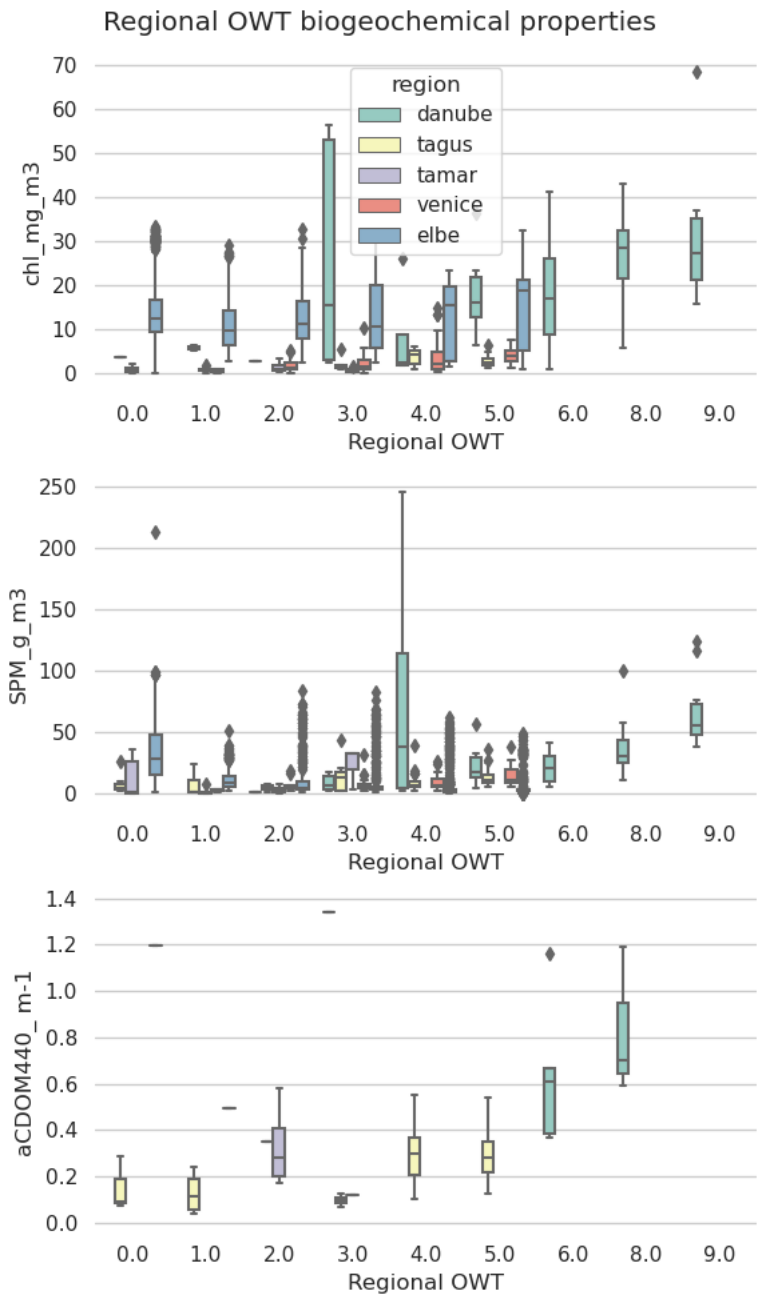

Figure 14: Biogeochemical properties (chlorophyll-a, suspended particulate matter, coloured dissolved organic matter) of regional OWT cluster sets without the extreme Curonian cluster set.

4.2 Wind and water conditions

Similar in form to analysis in the last section, Figure 15 compares regional OWT specific wind and water condition factors (wind speed, surface temperature, secchi depth, bottom visibility). Collection of these data in the historic datasets was very patchy, thus the classes are much less well characterised. One does see a drop in measured secchi depth with increasing OWT class across multiple sites.

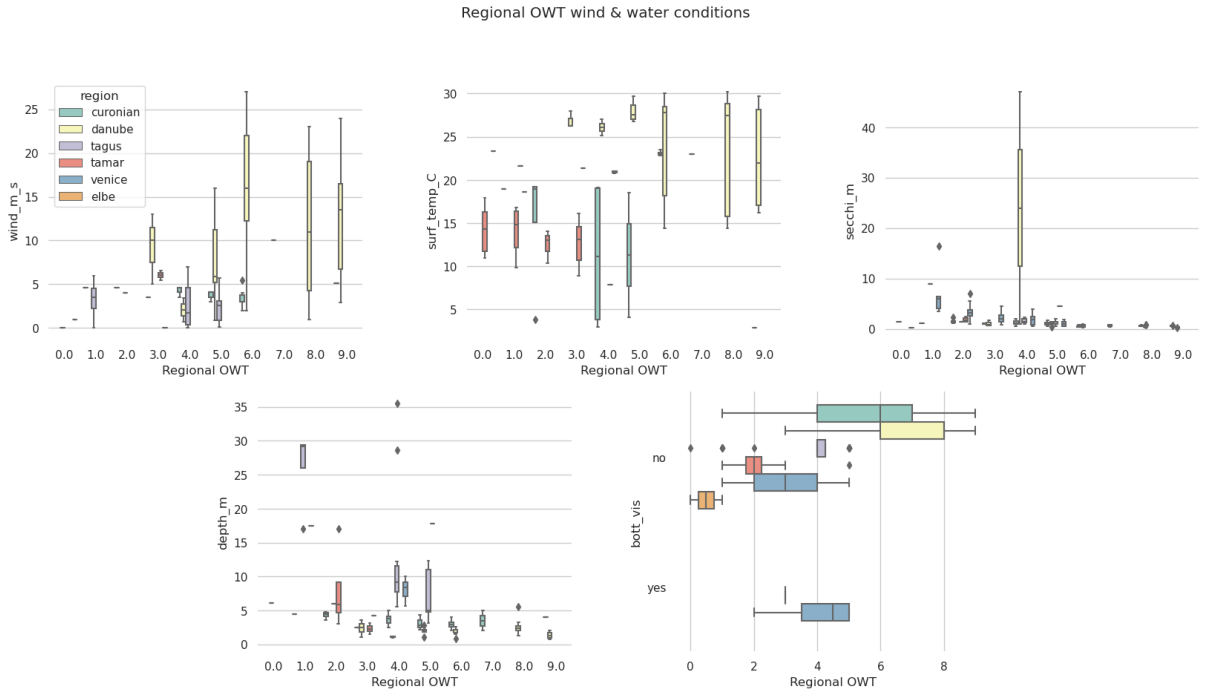

Figure 15: Wind and water condition properties (wind, surface temperature, secchi depth, water depth, bottom visible) of regional OWT cluster sets.

4.3 Reflectance ratio

This section considers whether particular regional OWT classes pick up band ratio signals useful for characterising areas prone to atmospheric correction errors. We would expect this question to be better addressed within WP5 and have thus focused solely on the green:NIR ratio used successfully in other projects such as HR-OC. High values of this ratio indicate an unrealistic atmospheric correction of the reflectance spectrum. One observes that relatively few regional OWT have a ratio value less than 10 (Figure 16), such as Elbe regional OWT 0 or Tagus regional OWT 0. There are quite large ratio values ($|abs| >> 20$, the cut-off used in the HR-OC algorithm) observed for certain regional OWT classes (e.g. Danube regional OWT 6 or Curonian regional OWT 8), which suggests that some of these regional OWT classes may very well be capturing that particular atmospheric correction error and thus the OWT method will be able to improve water quality algorithm performance in a similar way to HR-OC.

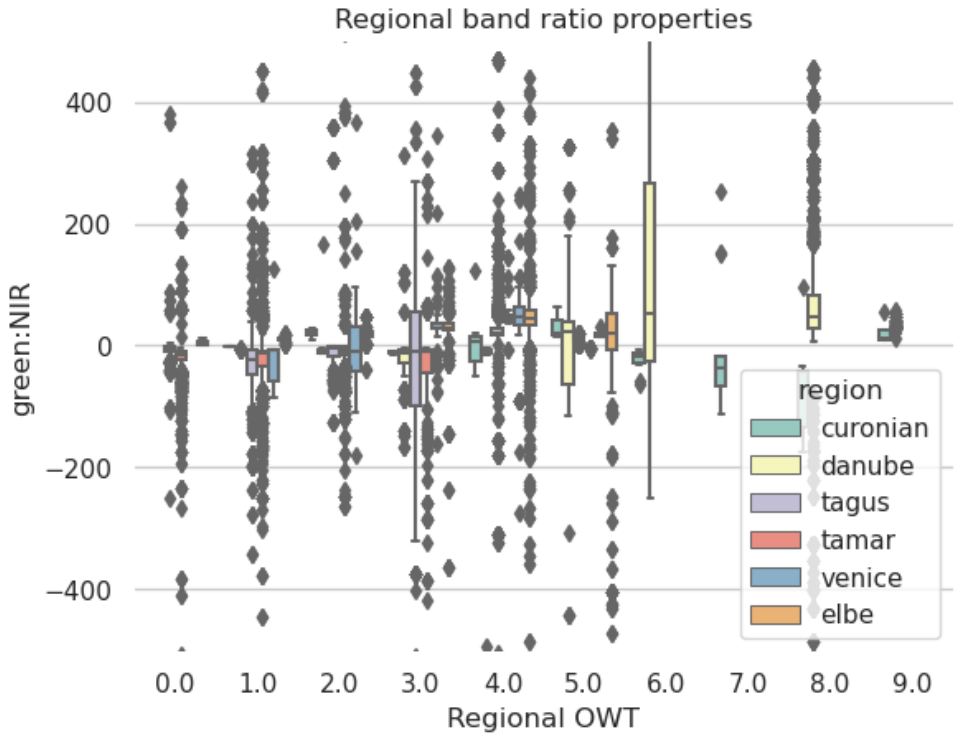

Figure 16: Band ratio (green OLCI_560: NIR OLCI_865) of regional OWT cluster sets where large absolute values (>>20) indicate atmospheric correction errors. Note that y-axis limit has been set to [-500,500] to allow better inter-region comparison.

5 Global cluster set characterisation

5.1 Biogeochemical parameters

Biogeochemical property characterisation of the global OWT classes is presented in Figure 17. A general small increasing trend is observed across SPM with increasing global OWT class, a similar but much smaller increasing trend is present across the Chl-a values. CDOM appears to decrease with increasing global OWT class but variability between classes is quite high.

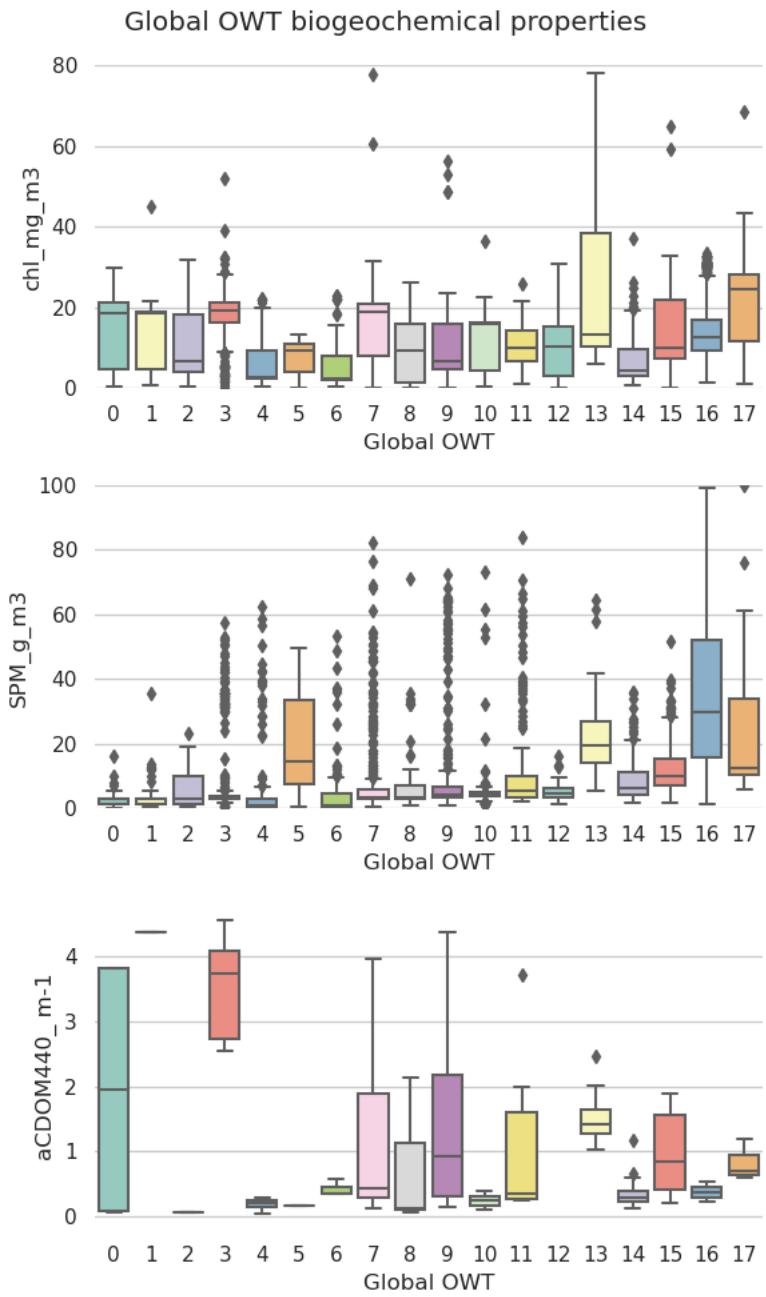

Figure 17: Biogeochemical properties (chlorophyll-a, suspended particulate matter, coloured dissolved organic matter) of the global OWT cluster set. Note the axes on chlorophyll-a and SPM have been adjusted to remove outliers, in order to better allow cluster comparison (global OWT {8, 13} had some chlorophyll-a values over 80 mg/m3, global OWT {12, 15} had SPM values over 100 g/m3)

5.2 Regional cluster set grouping assessment based on biogeochemical parameters

One can perform this comparison by either (1) comparing group regional OWT characteristics for a particular global OWT class (see Figure 18), or (2) comparing characteristics within a particular global OWT class separated out by region (see Figure 19). In the first instance, by comparing the boxplots one sees little indication of significant regional differences in SPM values based on the grouped regional OWT classes for a particular global OWT class. This is not always the case for chl-a, with the regional boxplots for global OWT {1, 2, 3, 8} suggesting very different ranges for each regional OWT class (Figure 18). The latter comparison, being based on the global OWT classes, has a higher number of representative points for each OWT class (Figure 19). The general pattern of SPM being less variable between regions remains consistent for the global OWT classes {1, 2, 4, 9, 10, 12) but displays high variability across

sites in some other classes (such as global OWT classes 5 or 8). The pattern observed for chl-a displays even higher variability. Comparisons for CDOM are difficult due to low sampling numbers but also show high variability across sites where comparison is possible.

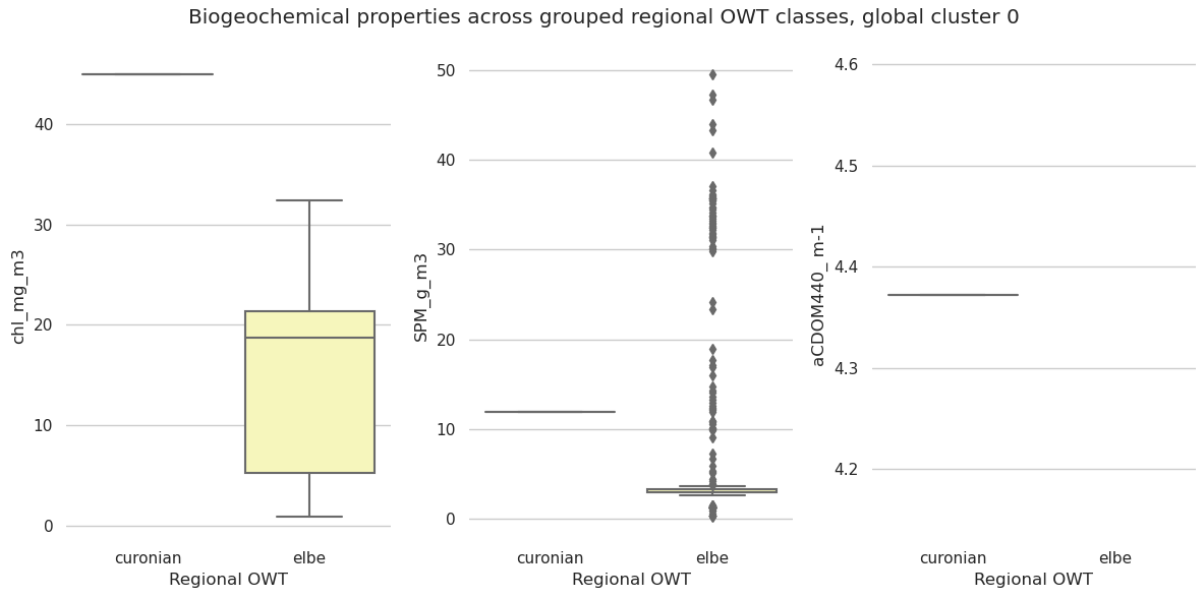

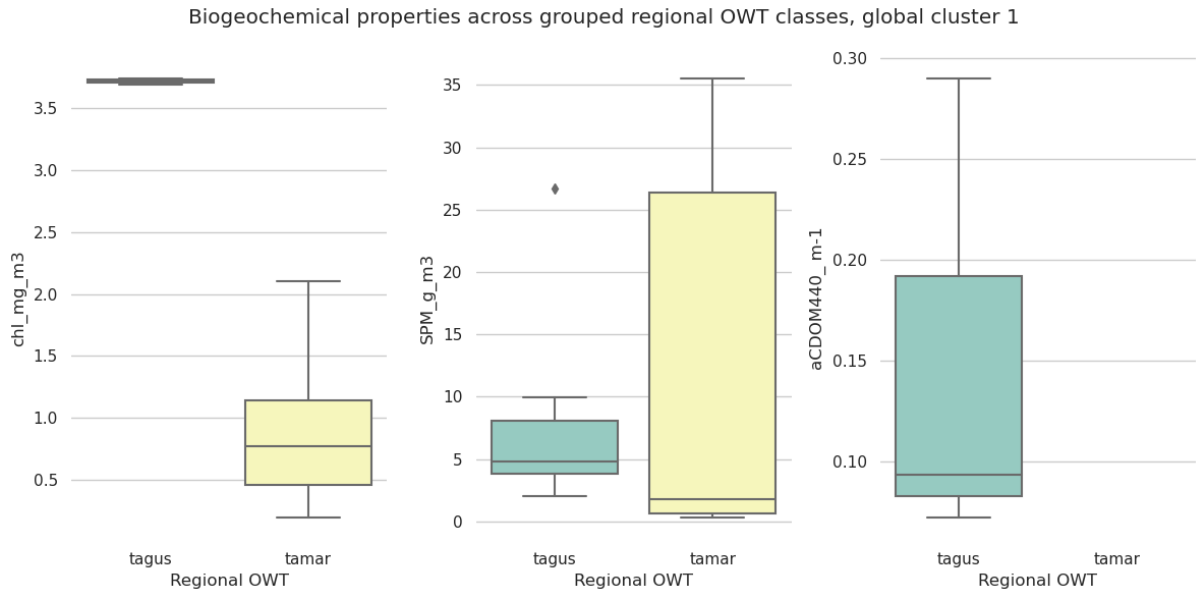

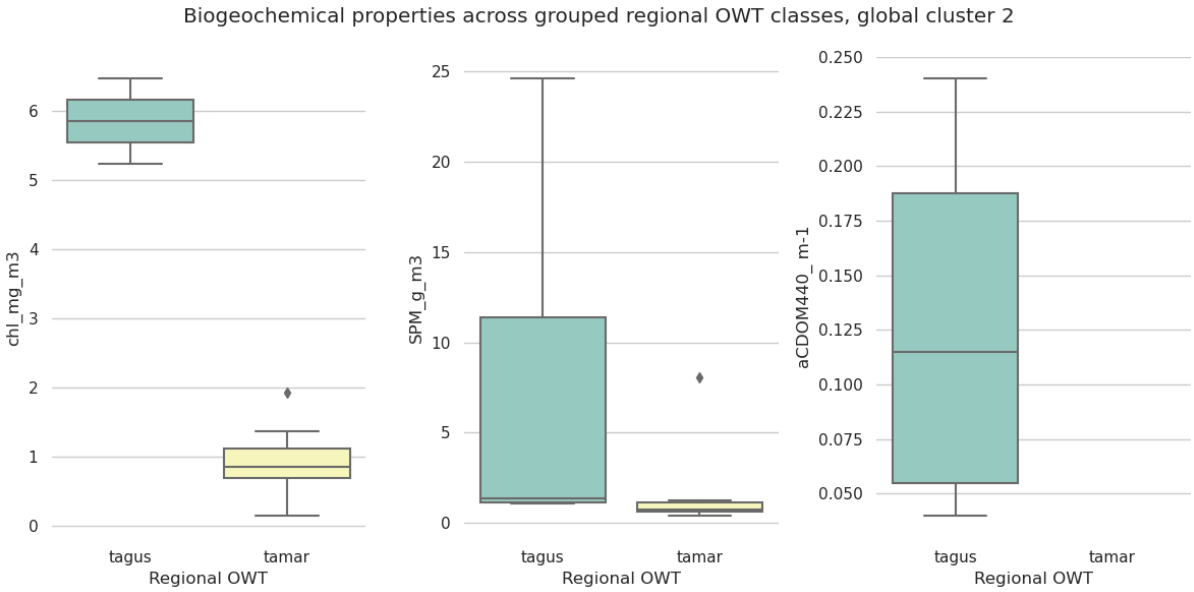
Biogeochemical properties across grouped regional OWT classes, global cluster 2
chl_mg_m3
SPM_g_m3
aCDOM440_ m-1
tagus
tamar
Regional OWT

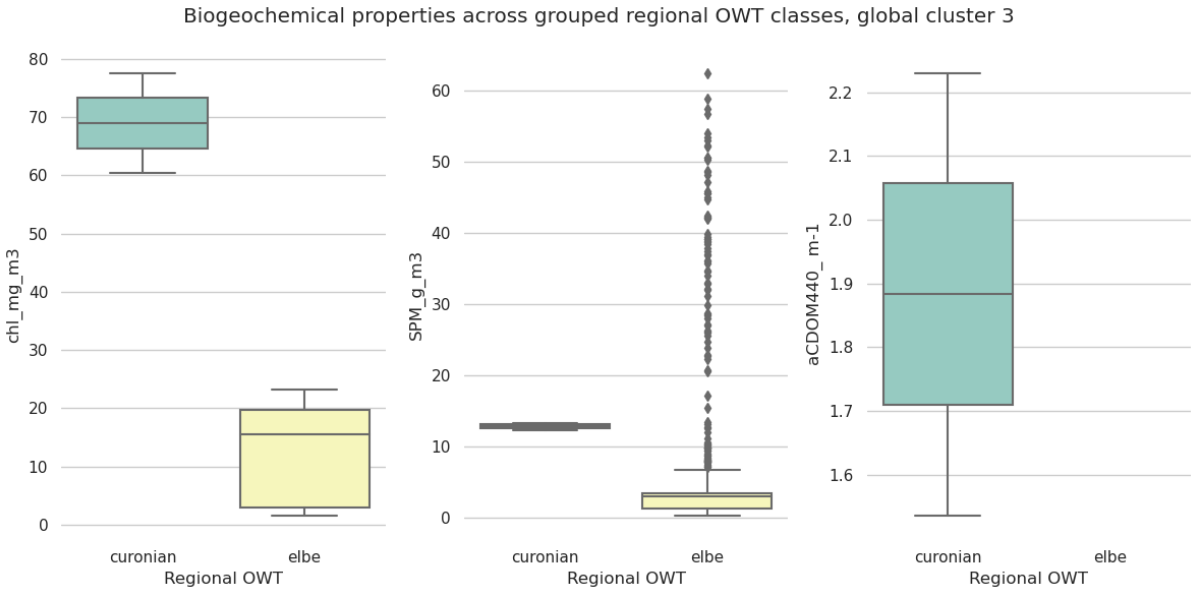
Biogeochemical properties across grouped regional OWT classes, global cluster 3
chl_mg_m3
SPM_g_m3
aCDOM440_ m-1
curonian
elbe
Regional OWT

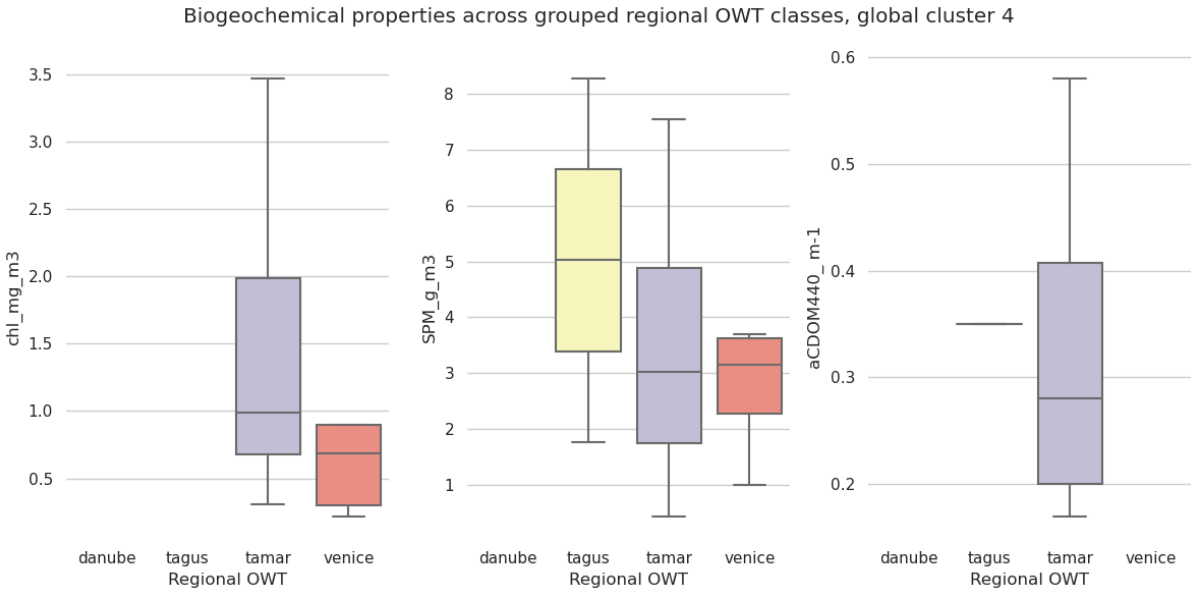
Biogeochemical properties across grouped regional OWT classes, global cluster 4
chl_mg_m3
SPM_g_m3
aCDOM440_ m-1
danube
tagus
tamar
venice
Regional OWT

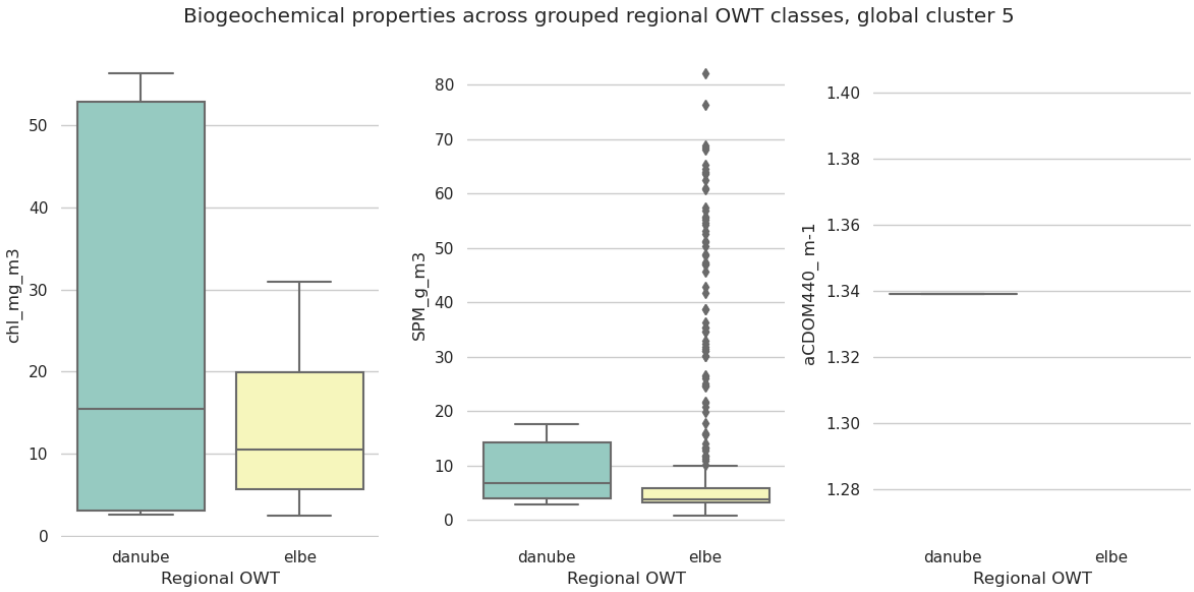
Biogeochemical properties across grouped regional OWT classes, global cluster 5
chl_mg_m3
SPM_g_m3
aCDOM440_ m-1
danube
elbe
Regional OWT


Biogeochemical properties across grouped regional OWT classes, global cluster 6
chl_mg_m3
SPM_g_m3
aCDOM440_ m-1
danube
tagus
tamar
Regional OWT

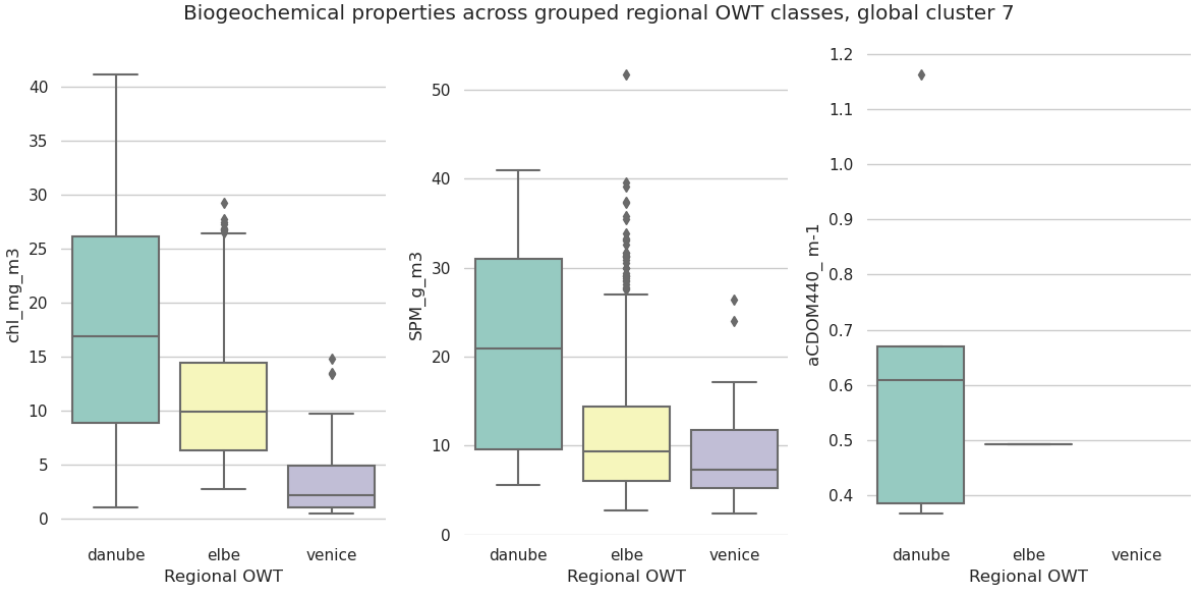
Biogeochemical properties across grouped regional OWT classes, global cluster 7
chl_mg_m3
SPM_g_m3
aCDOM440_ m-1
danube
elbe
venice
Regional OWT

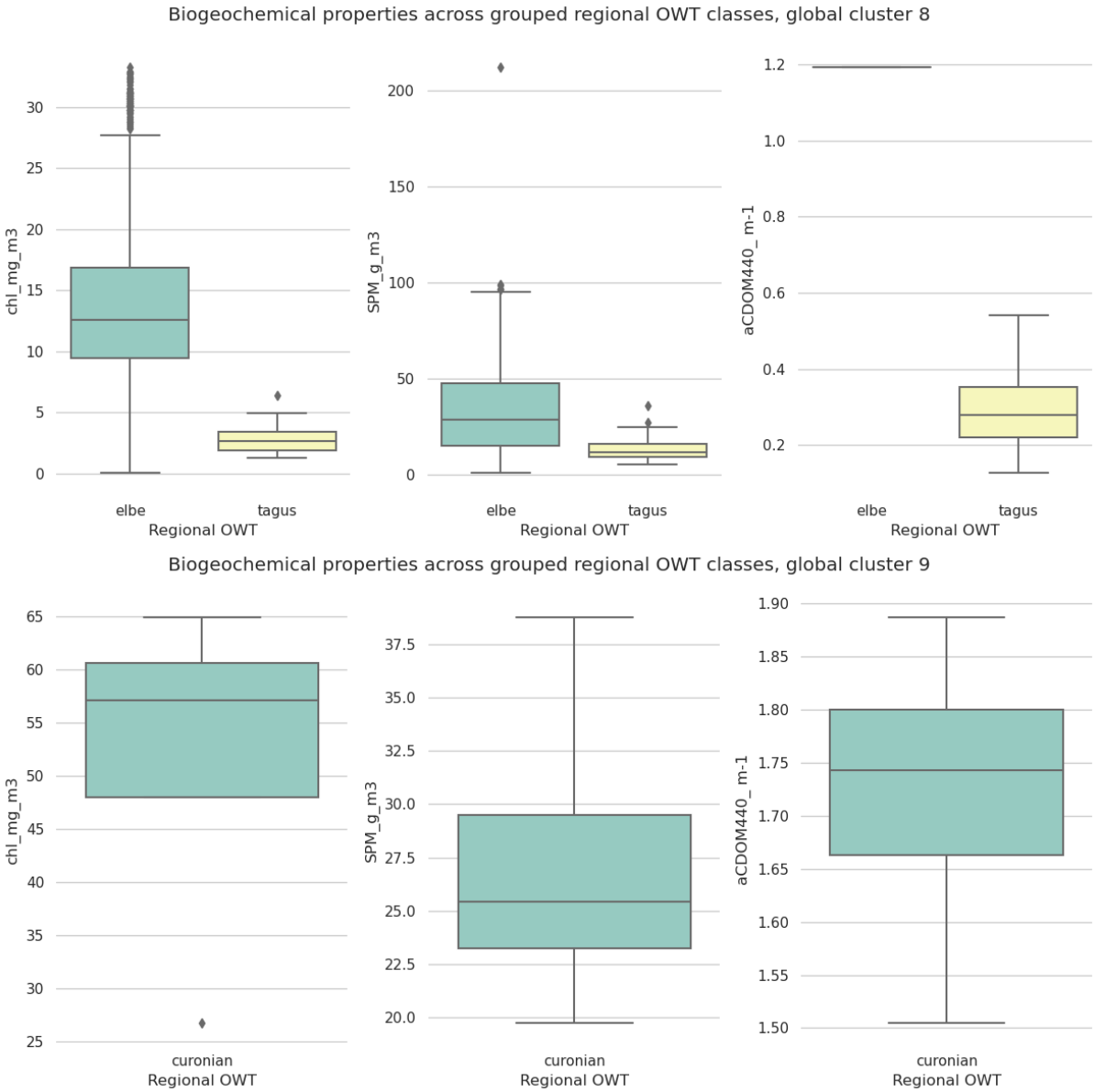

Figure 18: Comparative biogeochemical properties of grouped regional cluster set used as basis for global cluster creation. Only groups with sufficient comparison numbers are shown.

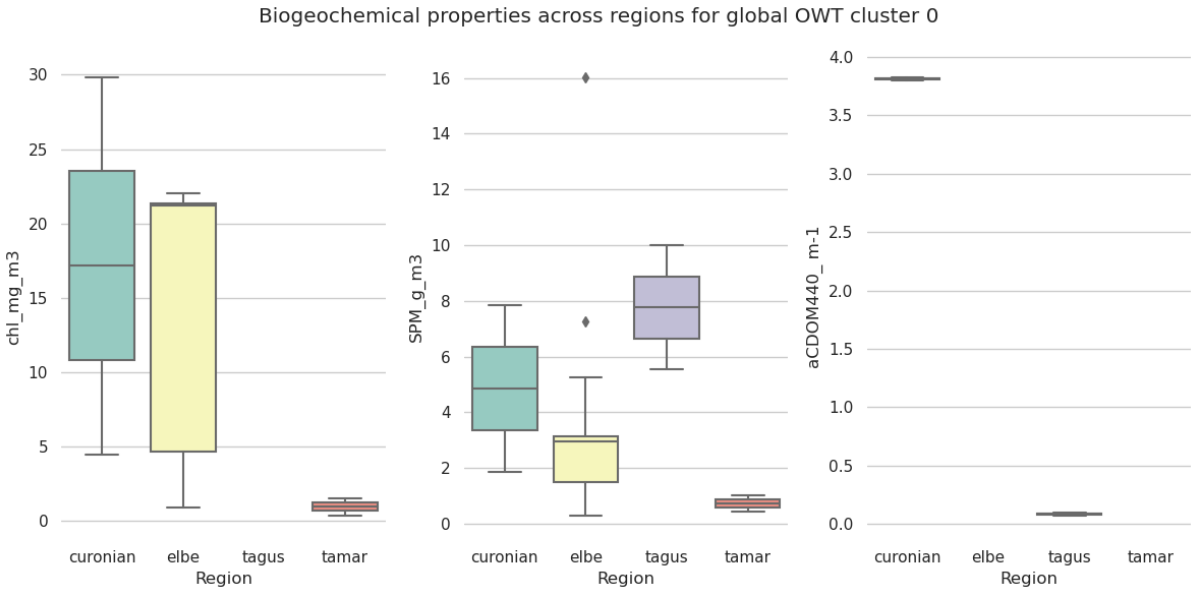
Biogeochemical properties across regions for global OWT cluster 0
chl_mg_m3
SPM_g_m3
aCDOM440_ m-1
curonian
elbe
tagus
tamar
Region

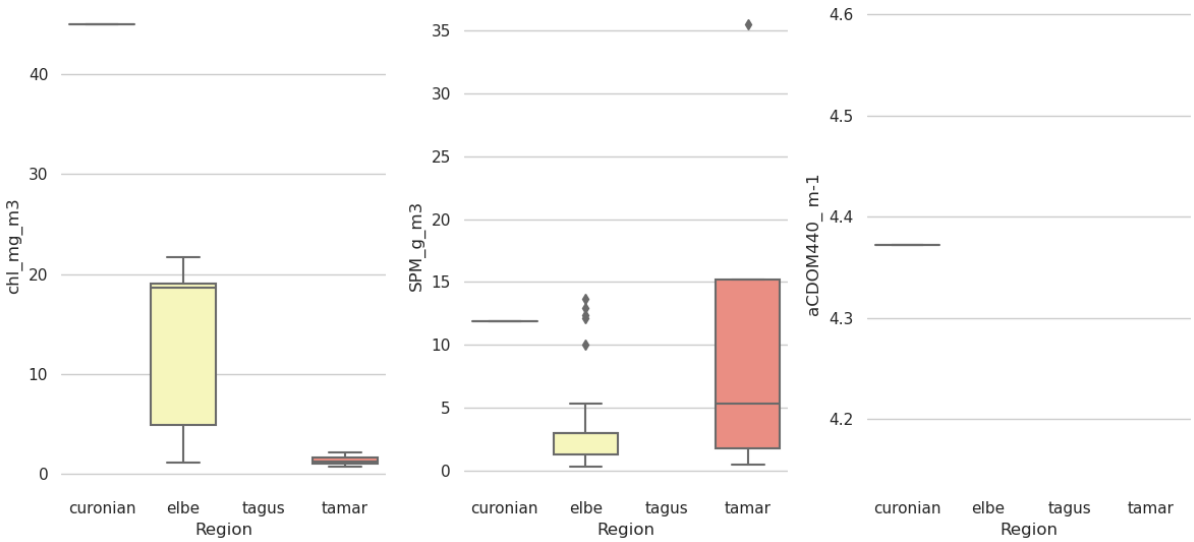
Biogeochemical properties across regions for global OWT cluster 1
chl_mg_m3
SPM_g_m3
aCDOM440_ m-1
curonian
elbe
tagus
tamar
Region

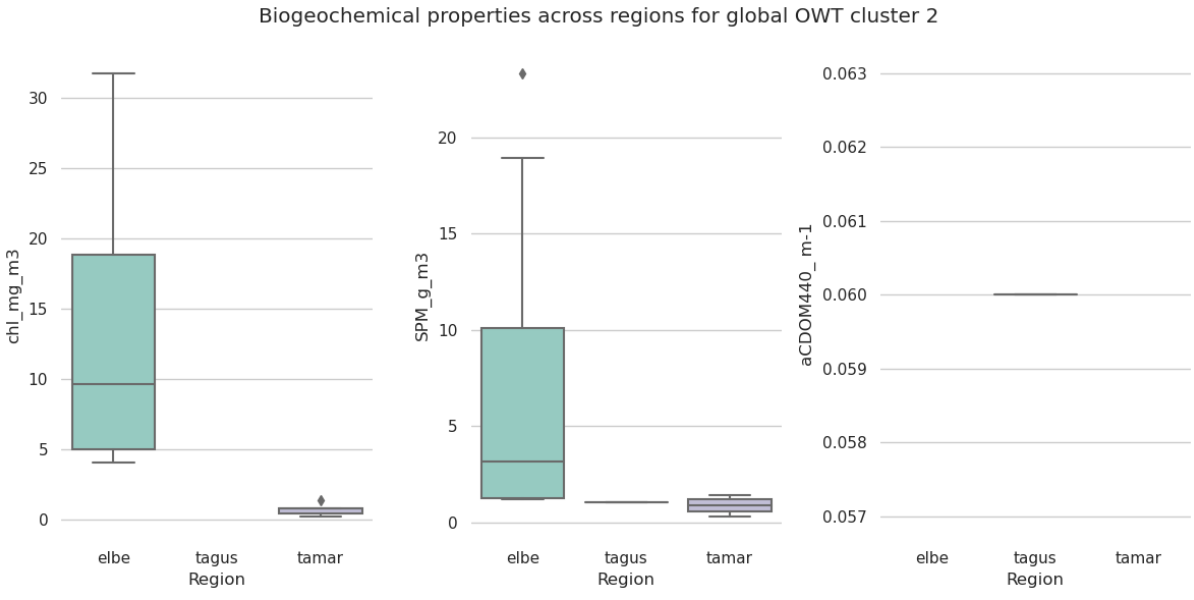
Biogeochemical properties across regions for global OWT cluster 2
chl_mg_m3
SPM_g_m3
aCDOM440_ m-1
elbe
tagus
tamar
Region

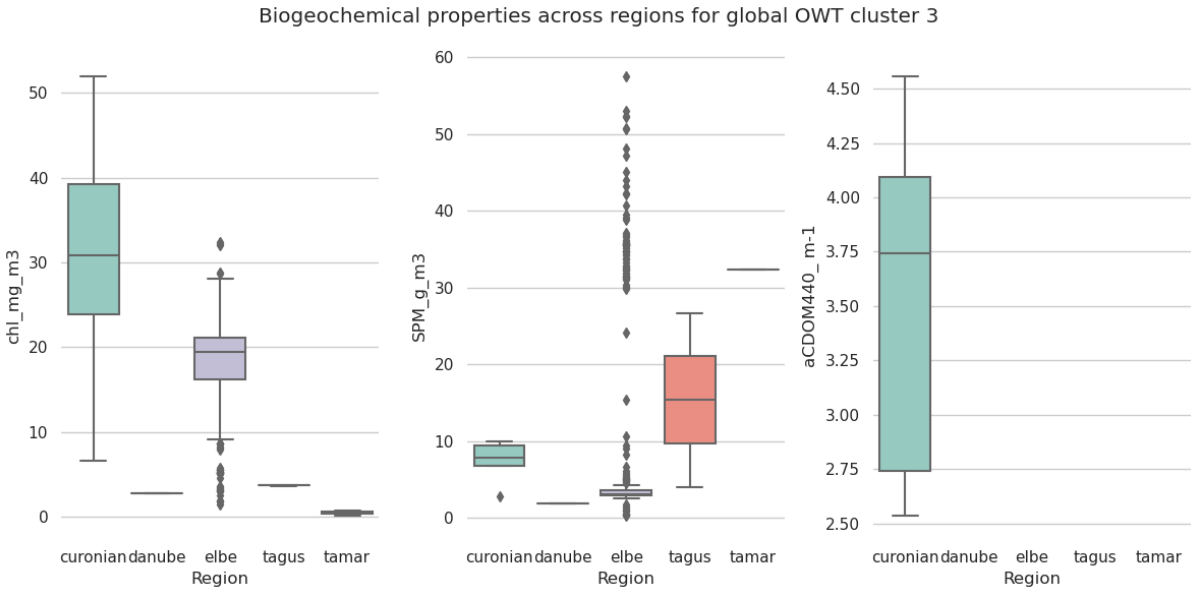
Biogeochemical properties across regions for global OWT cluster 3
chl_mg_m3
SPM_g_m3
aCDOM440_ m-1
curonian
danube
elbe
tagus
tamar
Region

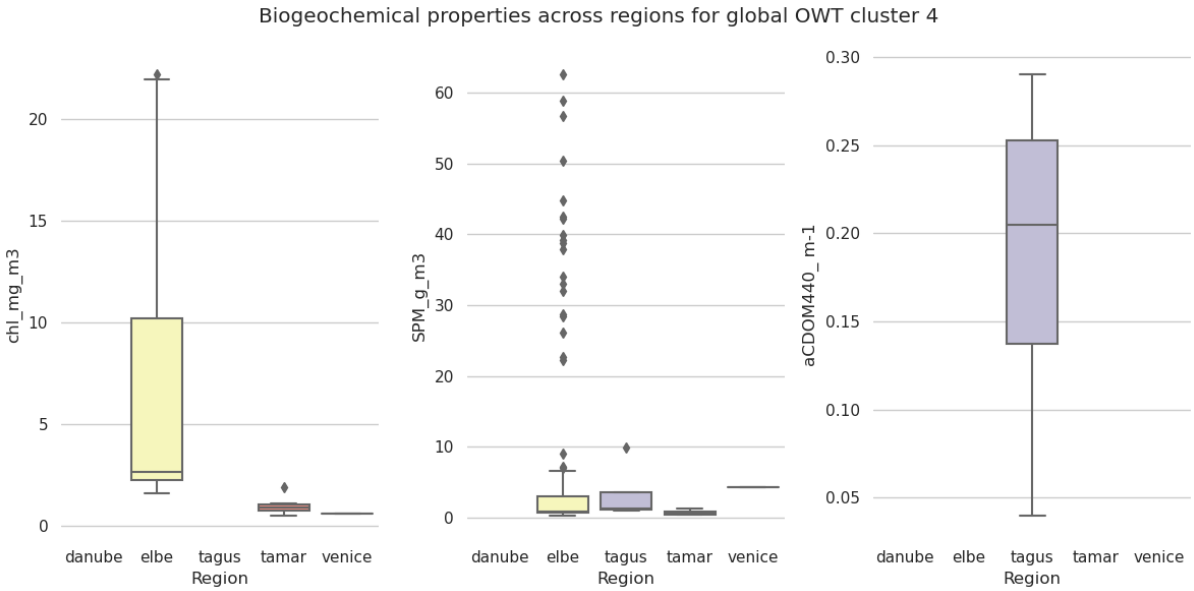
Biogeochemical properties across regions for global OWT cluster 4
chl_mg_m3
SPM_g_m3
aCDOM440_ m-1
danube
elbe
tagus
tamar
venice
Region

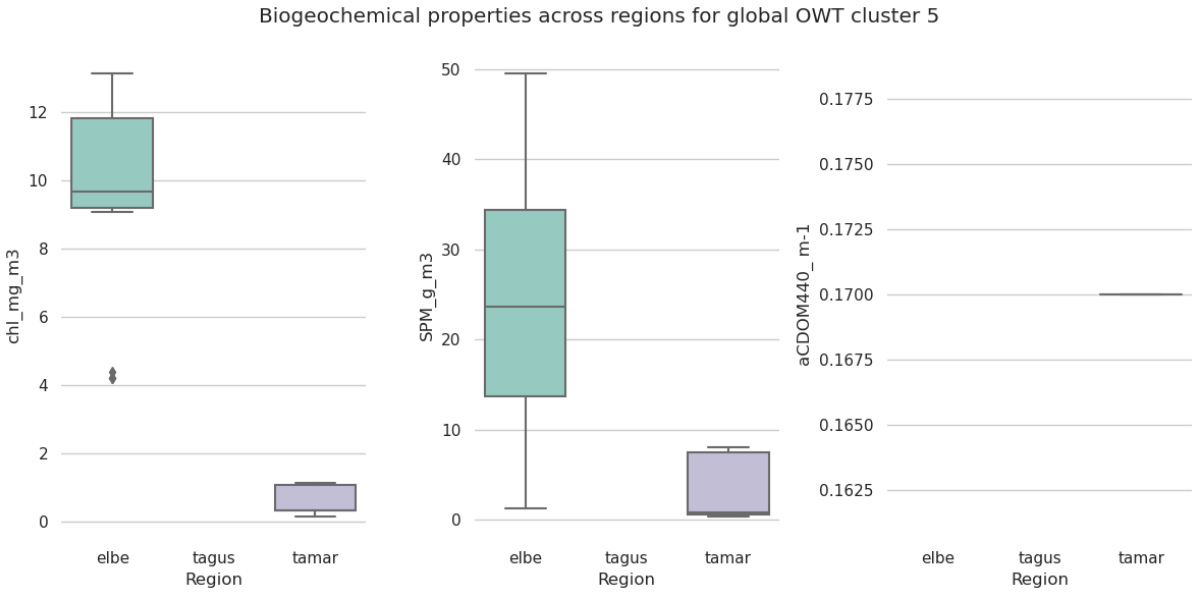
Biogeochemical properties across regions for global OWT cluster 5
chl_mg_m3
SPM_g_m3
aCDOM440_ m-1
elbe
tagus
tamar
Region

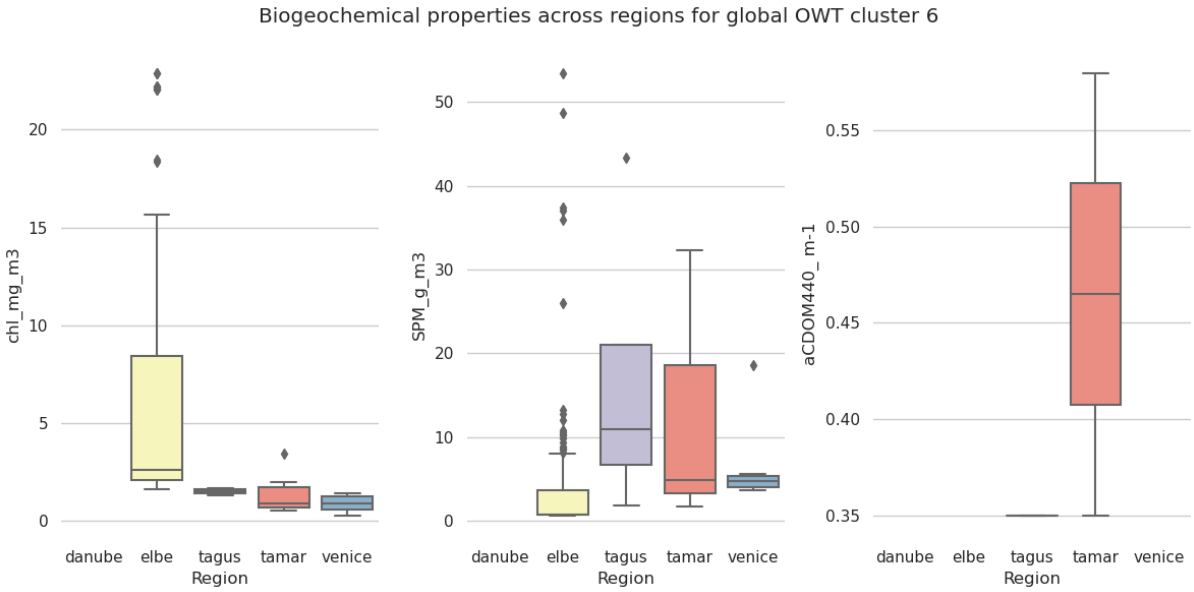
Biogeochemical properties across regions for global OWT cluster 6
chl_mg_m3
SPM_g_m3
aCDOM440_ m-1
danube elbe tagus tamar venice
Region

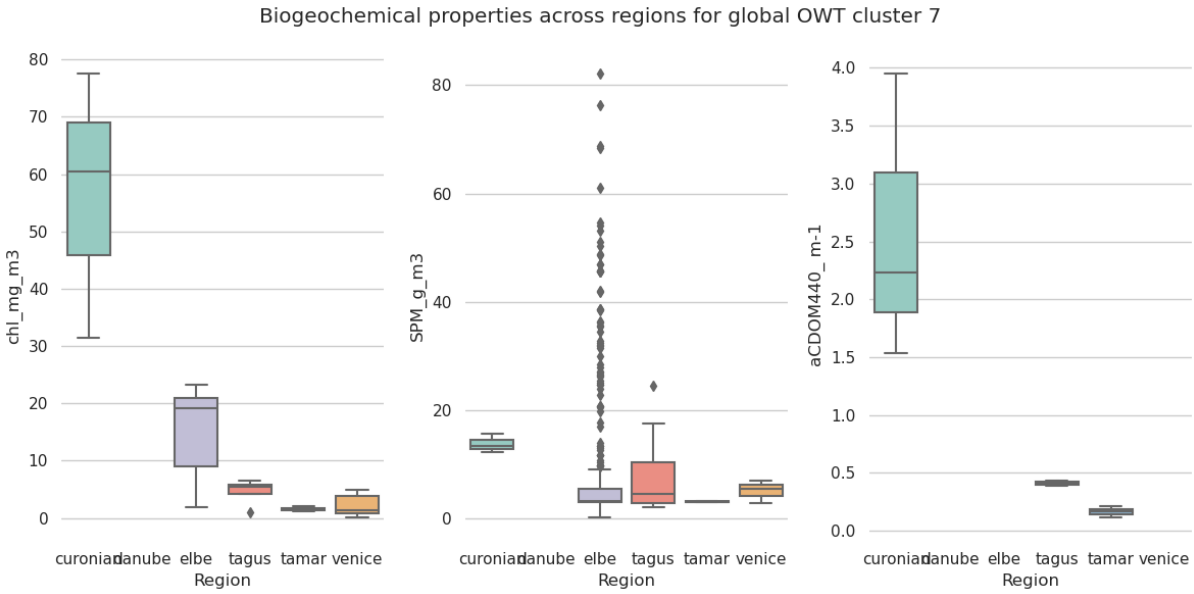
Biogeochemical properties across regions for global OWT cluster 7
chl_mg_m3
SPM_g_m3
aCDOM440_ m-1
curonian danube elbe tagus tamar venice
Region

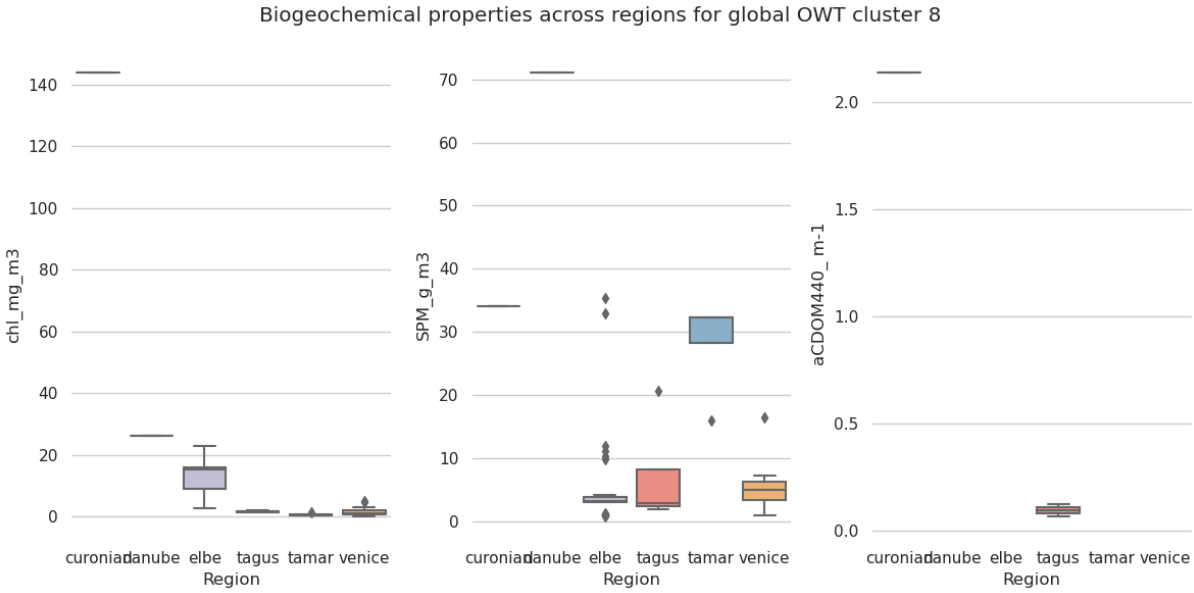
Biogeochemical properties across regions for global OWT cluster 8
chl_mg_m3
SPM_g_m3
aCDOM440_ m-1
curonian danube elbe tagus tamar venice
Region

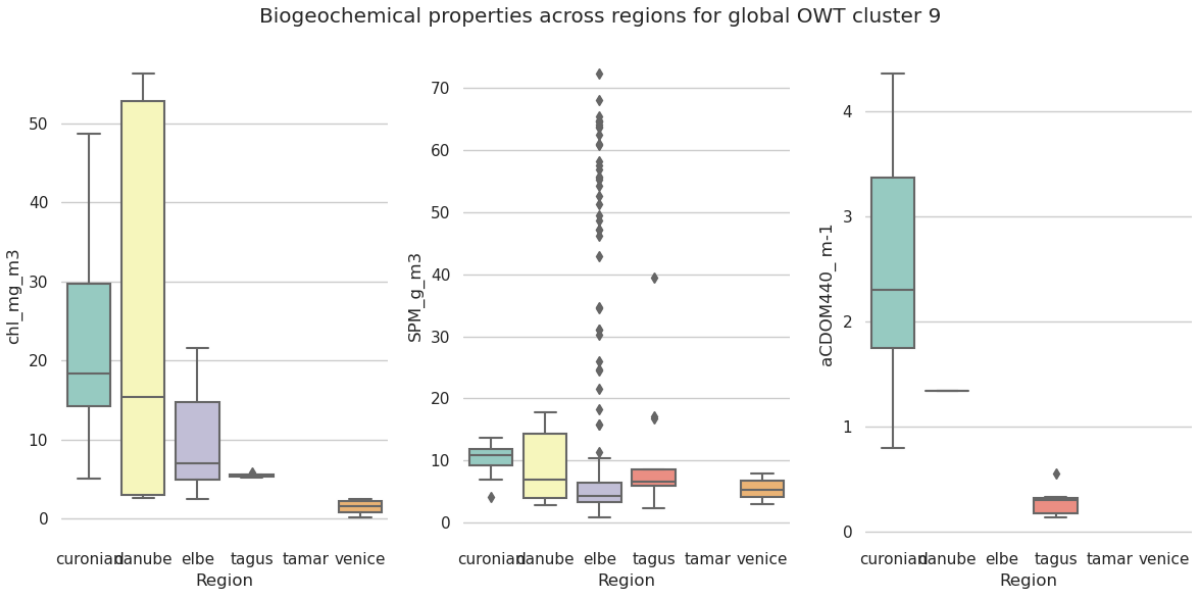
Biogeochemical properties across regions for global OWT cluster 9
chl_mg_m3
SPM_g_m3
aCDOM440_ m-1
curonian danube elbe tagus tamar venice
Region

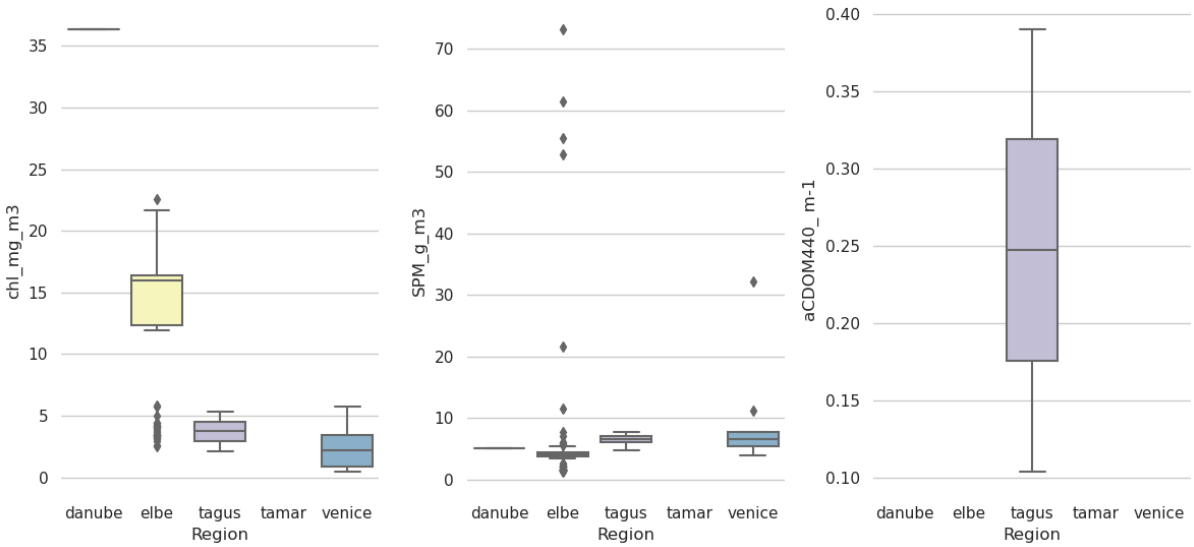
Biogeochemical properties across regions for global OWT cluster 10
chl_mg_m3
SPM_g_m3
aCDOM440_ m-1
danube elbe tagus tamar venice
Region

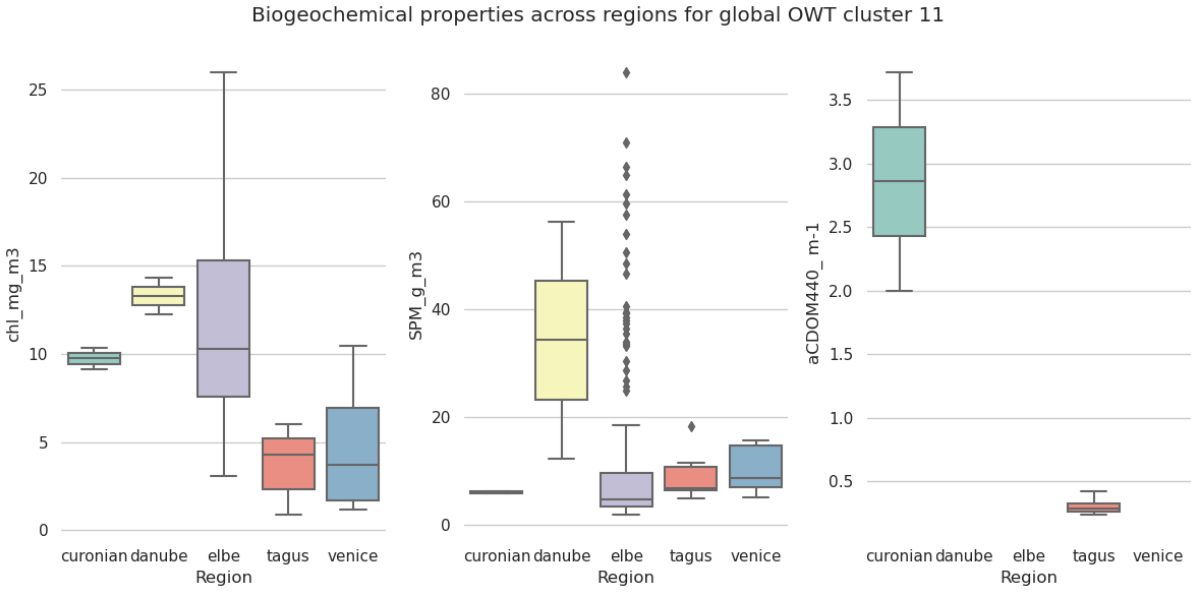
Biogeochemical properties across regions for global OWT cluster 11
chl_mg_m3
SPM_g_m3
aCDOM440_ m-1
curonian danube elbe tagus venice
Region

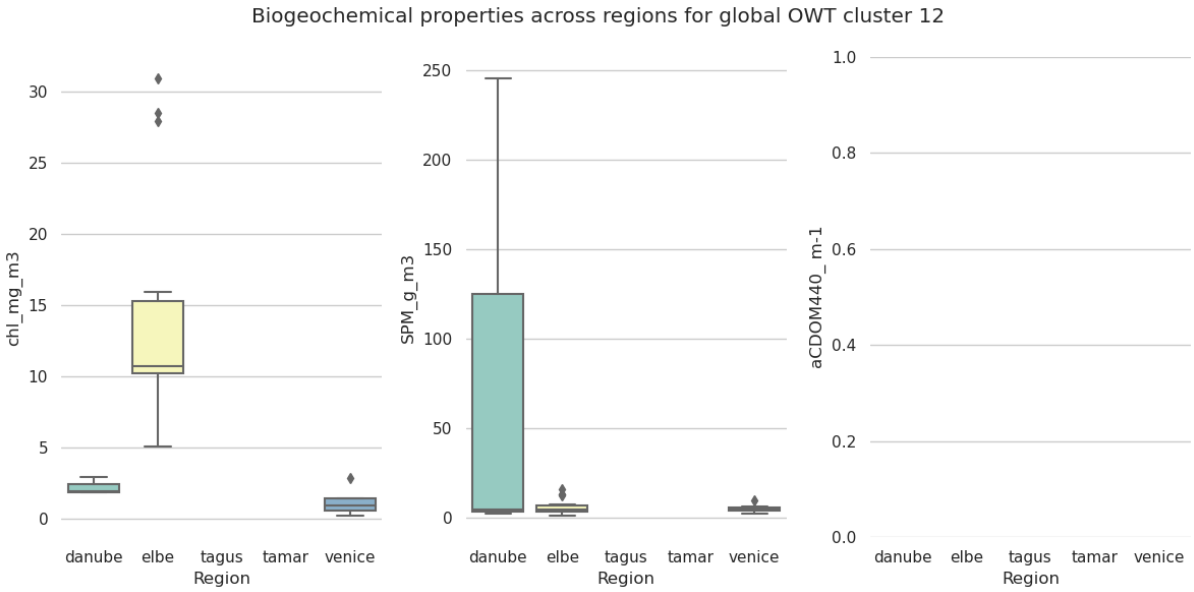
Biogeochemical properties across regions for global OWT cluster 12
chl_mg_m3
SPM_g_m3
aCDOM440_ m-1
danube
elbe
tagus
tamar
venice
Region

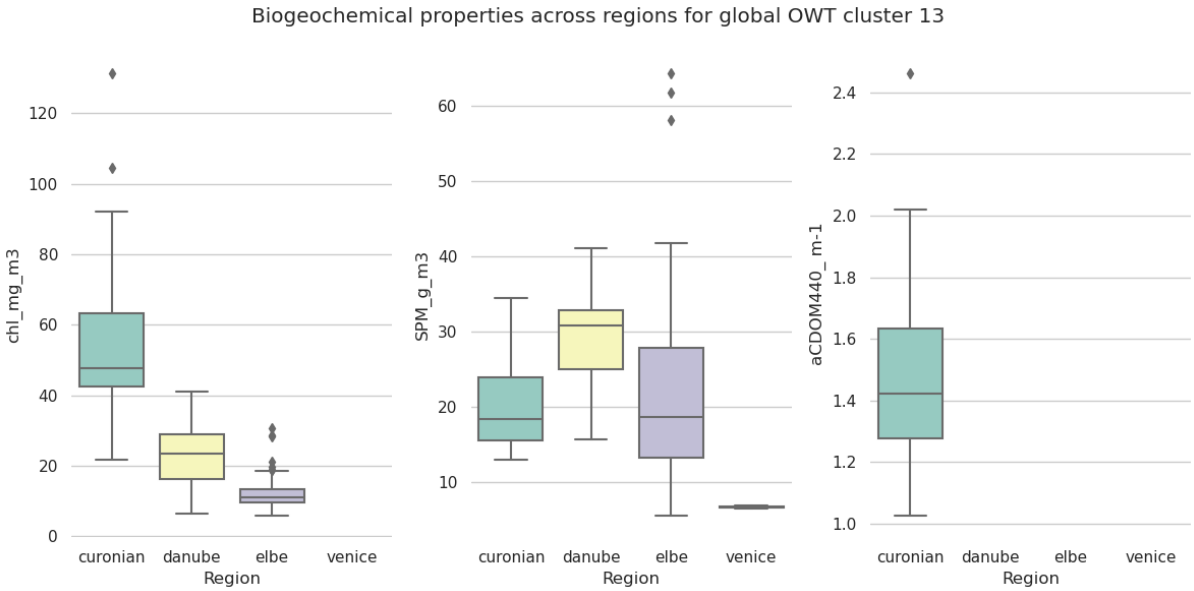
Biogeochemical properties across regions for global OWT cluster 13
chl_mg_m3
SPM_g_m3
aCDOM440_ m-1
curonian
danube
elbe
venice
Region

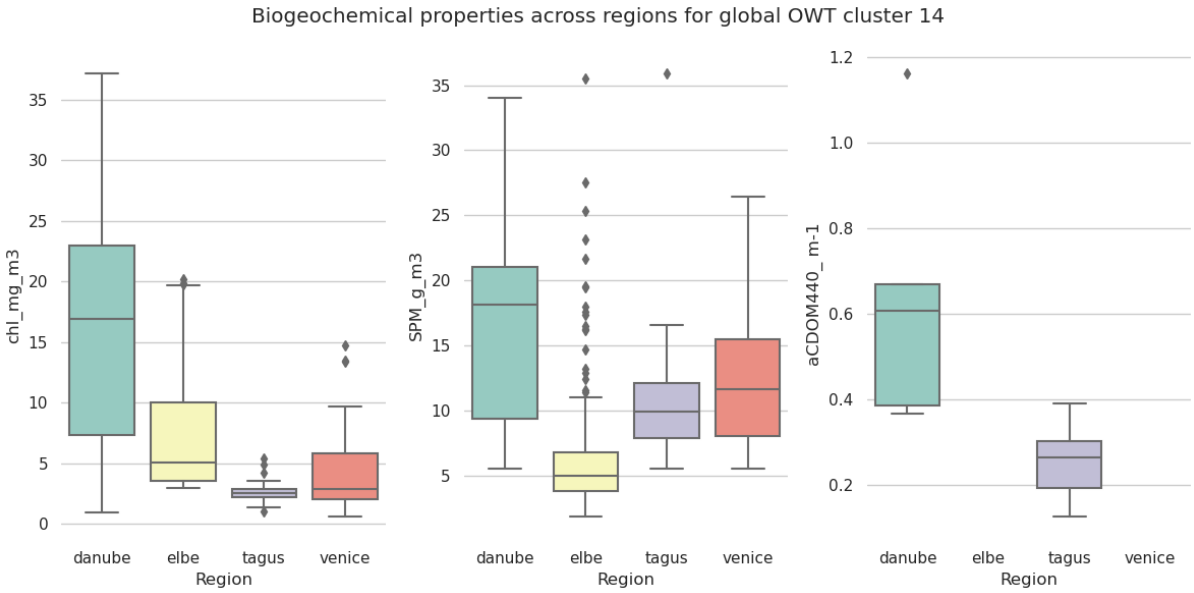
Biogeochemical properties across regions for global OWT cluster 14
chl_mg_m3
SPM_g_m3
aCDOM440_ m-1
danube
elbe
tagus
venice
Region

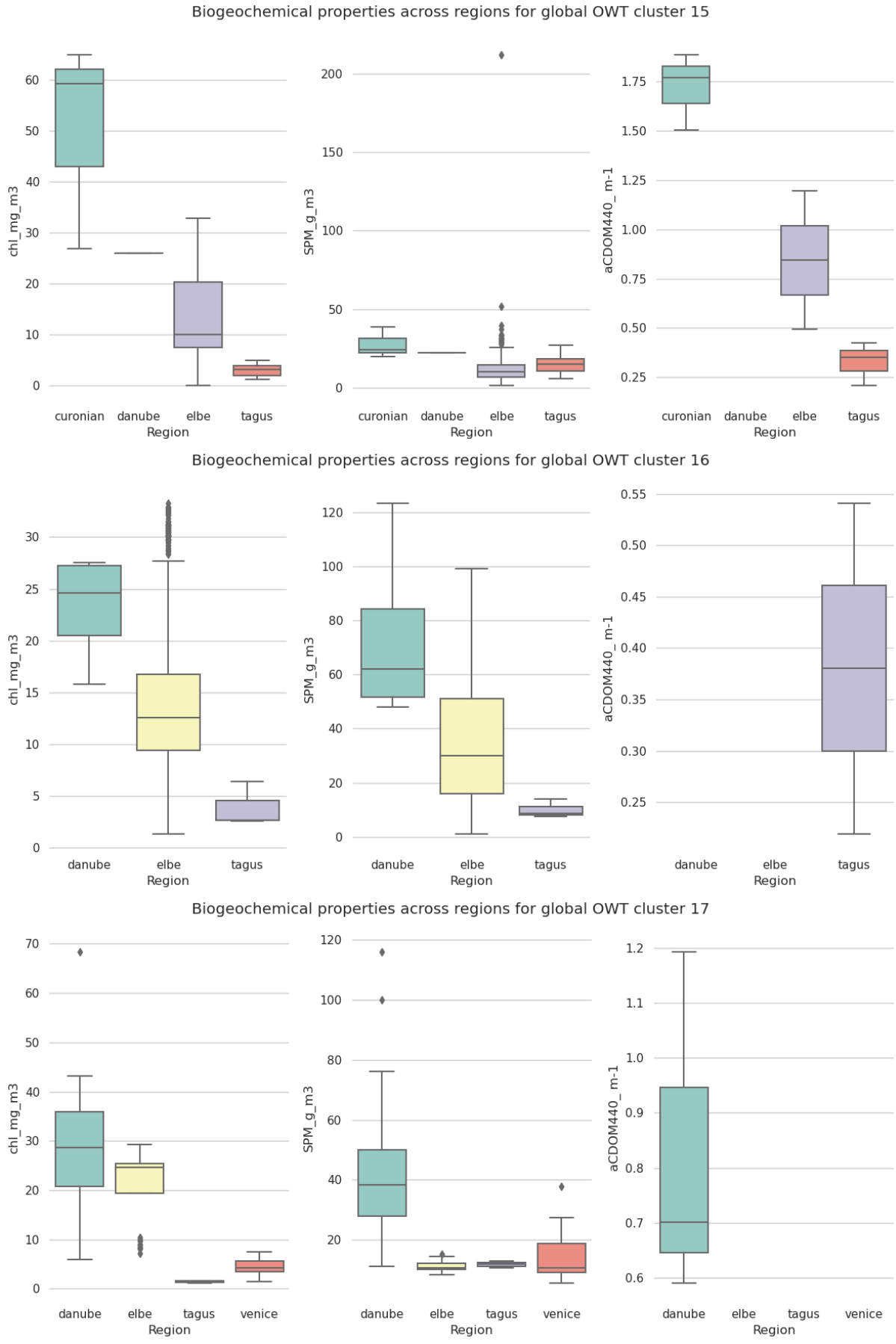

Figure 19: Comparison of biogeochemical properties for each global OWT class separated by region, shown for classes with sufficient sample numbers to allow regional comparison.

5.3 Wind and water conditions

Comparison of global OWT specific wind and water condition factors (wind speed, surface temperature, secchi depth, bottom visibility) is shown in Figure 20. Similar to the regional OWT cluster sets, a tendency of decreasing secchi depth with increasing OWT class is observed. A general increase in wind speed and surface temperature is also observed with increasing OWT class.

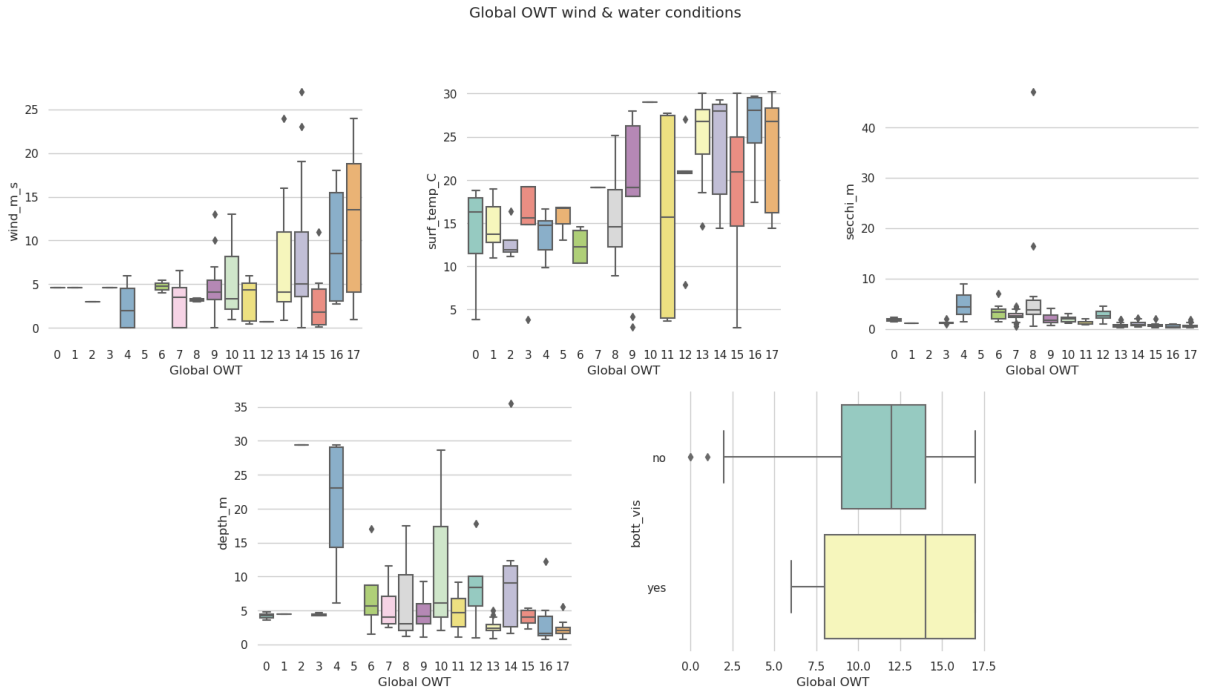

Figure 20: Wind and water condition properties (wind, surface temperature, secchi depth, water depth, bottom visible) of global OWT cluster set.

5.4 Reflectance ratio

Comparison of the band ratio considered in §4.3 for the global OWT classes is shown in Figure 21. It is interesting that this ratio is closer to zero with decreasing global OWT class (opposite to that observed for Sentinel-2 MSI). Global OWT classes {0, 5, 6, 8, 12, 13, 16} have green:NIR ratio median values (absolute value) less than 10, the lower bound cutoff in the HR-OC model. The global OWT classes {1, 2, 4, 7, 14} median ratio values are between 10 and 20, OWT class 11 median is almost exactly 20, and all other classes are well outside these bounds. Global OWT classes {0:2, 4:8, 12} have negative median ratio values, with OWT classes {3, 13} containing negative values within their lower quartile bound.

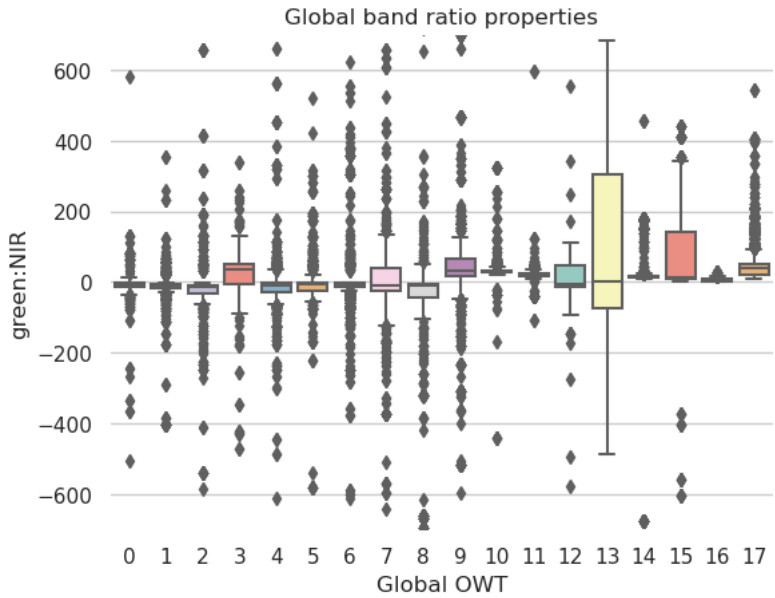

Figure 21: Band ratio (green OLCI_560: NIR OLCI_865) of the global OWT cluster set, where large absolute values (>>20) indicate atmospheric correction errors. (Note y-axis limit has been manually set to [-700,700] in order to allow better visual comparability between OWT classes.)

6 Round Robin Algorithm Assessment

The in-situ data matchups used in the characterization of the properties of the water types can also be used to assess the performance of different in-water algorithms, where the algorithm products match properties that have been measured in-situ. As there are multiple candidate in-water algorithms for some of the in-water products of interest to CERTO a round robin approach is used to compare the performance of the available algorithms and determine which can be considered as optimal.

6.1 Round Robin Overview

The methodologies used for the in-water algorithm round robin follow those of OC-CCI as given in the OC_CCI-PVASR (in water) documents. This schema is designed to perform a multi-metric assessment of the available in-water algorithms (those that derive an in-water product such as chlorophyll-a concentration from Rrs data) by comparing the performance of the algorithms against each other using in-situ measurements as the validation data.

6.2 Scoring Approach

The round robin scoring is a multi-metric assessment using the following univariate statistical tests, each of which is commonly used in comparisons between modelled and in-situ data (Doney et al., 2009; Friedrichs et al., 2009).

- Pearson correlation coefficient (r)
- Bias (δ)
- Centre-pattern (or unbiased) Root Mean Square Error (Δ)
- Slope (S) of a Type-2 regression
- Intercept (I) of a Type-2 regression
- Percentage of possible retrievals

Note that in some cases, variables (such as chl-a) are log-normally distributed at the global scale, meaning that for those variables the statistics and scoring should be performed on log-transformed values to allow the statistical relationships to hold true.

For each metric, the best model (and those that are statistically indistinguishable from it) score 2 points, those close to deviating from the performance of the best score 1 point, and those that were significantly different from the best would score 0 points. For each of the statistics this similarity is assessed slightly differently, as explained below.

6.2.1 Pearson correlation coefficient

The correlation coefficient *r* is calculated according to:

$$r = \frac{1}{N-1}\sum_{i=1}^{N}\left[\frac{X_i^M - \left(\frac{1}{N}\sum_{j=1}^{N} X_j^M\right)}{\left\{\frac{1}{N-1}\sum_{k=1}^{N}\left[X_k^m - \left(\frac{1}{N}\sum_{l=1}^{N} X_l^M\right)\right]^2\right\}^{0.5}}\right]\left[\frac{X_i^E - \left(\frac{1}{N}\sum_{m=1}^{N} X_m^E\right)}{\left\{\frac{1}{N-1}\sum_{n=1}^{N}\left[X_n^E - \left(\frac{1}{N}\sum_{o=1}^{N} X_o^E\right)\right]^2\right\}^{0.5}}\right] \quad (1)$$

where X is the variable and N is the number of samples. The superscript E denotes the estimated variable (from the algorithm) and the superscript M denotes the measured variable (from the in-situ dataset). Note that the Pearson correlation coefficient assumes a linear relationship between variables and normal distributions. The correlation coefficient may take any value between -1.0 and 1.0.

Scoring: The *r* scoring involved determining whether the *r*-value for each model was statistically lower than the model with an *r*-value closest to 1 (the best model). This was done using the z-score, which is used to determine if two correlation coefficients are statistically different from one another (Cohen and Cohen, 1983). Knowing the *r*-value for two respective models (r_1 and r_2, for model 1 and 2 respectively) and the number of samples used to determine the r-values (n_1 and n_2), one can determine the z-score using the Fisher's r-to-z transformation.

Making use of the sample size employed to obtain each coefficient, these z-scores of each *r*-value (z_1 and z_2) can be used to compute the overall z-score (Cohen and Cohen, 1983), such that:

$$z_1 = 0.5\log\left(\frac{1+r_1}{1-r_1}\right) \quad (2)$$

$$z_2 = 0.5\log\left(\frac{1+r_2}{1-r_2}\right) \quad (3)$$

$$z_{score} = \frac{z_1 - z_2}{\left(\left[\frac{1}{n_1-3}\right]\left[\frac{1}{n_2-3}\right]\right)^{0.5}} \quad (4)$$

Having determined the z-score, this can be converted into a p-value assuming a normal distribution. For the model comparison, a two-tailed test is used and the score for each model is based upon the p-value as follows:

- 0 points if p-value for the model tested < 0.01 (i.e statistically different to the best model)
- 1 point if p-value for the model tested is ≥ 0.01 (i.e statistically similar to the best model)
- 2 points if p-value for the model tested is ≥ 0.05 (i.e statistically very similar to the best model). This is not cumulative with a point for being ≥ 0.01.

6.2.2 Bias

The bias (δ) between model and measurement can be expressed according to:

$$\delta = \frac{1}{N}\sum_{i=1}^{N}(X_i^M - X_i^E) \tag{5}$$

Scoring: The closer the model bias (δ) is to the ideal value of zero, the better that model corresponds with the in-situ data. However, a model could have a δ close to the reference value of zero, when compared with another model, but have a much larger 95 % confidence interval, implying lower confidence in the retrieved δ. For both bias and centre-pattern Root Mean Square Error (§5.2.3) statistics, the 95% confidence interval is computed from the standard error of the mean and the t-distribution of the sample size such that:

$$Confidence\ Interval = t_{0.025,n-1}\frac{S_n}{\sqrt{n}}\,, \tag{6}$$

Where S_n is the standard deviation of the error, n is the number of matchups and t is the two-tailed t-distribution. The following points classification was introduced for the bias:

- 0 points = the 95 % confidence interval of δ for a particular model is higher than the 1.5 times the smallest 95 % confidence interval of any model. In addition to this, the 95% confidence interval around the modulus of the bias does not overlap with zero.
- 1 point = either the 95 % confidence interval of δ for a particular model is less than 1.5 times the smallest model 95 % confidence interval, or the 95% confidence interval around the modulus of the bias overlaps with zero, but not both cases.
- 2 points = the 95 % confidence interval of δ for a particular model is less than 1.5 times the smallest model 95 % confidence interval and the 95% confidence interval around the modulus of the bias overlaps with zero.

6.2.3 Centre-pattern Root Mean Square Error

The absolute centre-pattern (or unbiased) Root Mean Square Error (Δ) is related to the bias (δ) and RMSE (Ψ) as:

$$\Delta^2 = \Psi^2 - \delta^2 \tag{2}$$

It describes the error of the estimated values with respect to the measured ones, regardless of the average bias between the two distributions. In addition to computing Ψ and Δ for each model, it is possible to determine the confidence levels in the Ψ and Δ, which provide an indication of how confident one is in the statistics. The confidence intervals are computed from the standard error of the mean percentage and the t-distribution of the sample size. Confidence intervals provide a powerful way of highlighting differences and similarities between models.

Scoring: If the confidence intervals of two or more models overlap, then it can be assumed that the models have a statistically similar Ψ or Δ at the given confidence level. For each model,

the 90 % and 95 % confidence intervals are computed for both Ψ and Δ. Points for each model are awarded according to:

- 0 points = Ψ or Δ for the model tested is statistically higher than the Ψ or Δ for the best model (no overlap with a p-value of 0.01).
- 1 point = Ψ or Δ for the model tested is statistically similar to the Ψ or Δ for the best model (overlap with a p-value of 0.01).
- 2 points = Ψ or Δ for the model tested is statistically very similar to the Ψ or Δ for the best model (overlap with a p-value of 0.1.

6.2.4 Slope (S) and Intercept (I) of a Type-2 regression

The performance of a model with respect to in-situ data can be tested using linear regression between the estimated variable (from the model) and the measured variable (in-situ data), such that:

$$\mathrm{X}^{\mathrm{E}} = \mathrm{X}^{\mathrm{M}} S + I \tag{3}$$

In addition to computing the intercept (I) and the slope (S) from a Type-2 regression, it is possible to compute the standard deviation on *I* and *S*. The closer the intercept (*I*) is to the reference value of zero and the closer the slope (S) is to the reference value of one, the better the fit between variables.

Scoring: Similar to Bias, a model could have an intercept closer to the reference value of zero and a slope closer to the reference value of one, when compared with another model, but have a much larger standard deviation on its retrieved parameters, implying lower confidence in the fit. Therefore, to account for both these possibilities the following points classification is implemented for the slope (*S*) parameter:

- 0 points = the standard deviation of the S parameter for a particular model is higher than 1.5 times the smallest standard deviation in S. In addition to this, the S parameter ± its standard deviation does not overlap with 1.
- 1 point = either the standard deviation of the S parameter for a particular model is less than 1.5 times the smallest standard deviation or S ± its standard deviation overlaps with 1, but not both cases.
- 2 points = the standard deviation of the S parameter for a particular model is less than 1.5 times the smallest standard deviation and the S parameter ± its standard deviation overlaps with 1.

The following points classification was introduced for intercept (*I*) parameter:

- 0 points = the standard deviation of the I parameter for a particular model is higher than 1.5 times the smallest standard deviation in I. In addition to this, the I parameter ± its standard deviation does not overlap with that zero.
- 1 point = either the standard deviation of the I parameter for a particular model is less than 1.5 times the smallest standard deviation, or the I parameter ± its standard deviation overlaps zero, but not both cases.
- 2 points = the standard deviation of the I parameter for a particular model is less than 1.5 time the smallest standard deviation and the I parameter ± its standard deviation overlaps with zero.

6.2.5 Percentage of possible retrievals

The ability to reproduce measured product values is of limited utility if an algorithm only works for 1% of input pixels. Therefore, the percentage of possible retrievals (η) is an important criterion that should be considered in the comparison, calculated according to:

$$\eta = \frac{N^E}{N^M} 100 \quad (4)$$

where N^E represents the number of retrievals using the model and N^M represents the number of available matched in-situ data points.

Scoring: To compare the percentage of possible retrievals (η) between models, highest percentage and standard deviation of retrievals for all models was used. The following points criteria were set-up:

- 0 points = η of a model lies further than 1 standard deviation below the maximum algorithm η.
- 1 point = η of a model lies within 1 standard deviation of the maximum η.
- 2 points = η of a model is equal to the maximum η.

6.2.6 Bootstrapping and multi-metric scoring

To rank the performance of each model with reference to a particular variable, all points were summed over the set of statistical tests used. The total score for each model was then normalised to the highest score for a single model. A score of one indicates the model scored the highest total number of points across all tests, with values less than 1 showing the points score of each model relative to the highest achieved. Figure 22 shows a flow-chart illustrating the methodology of the scoring system used to compare models.

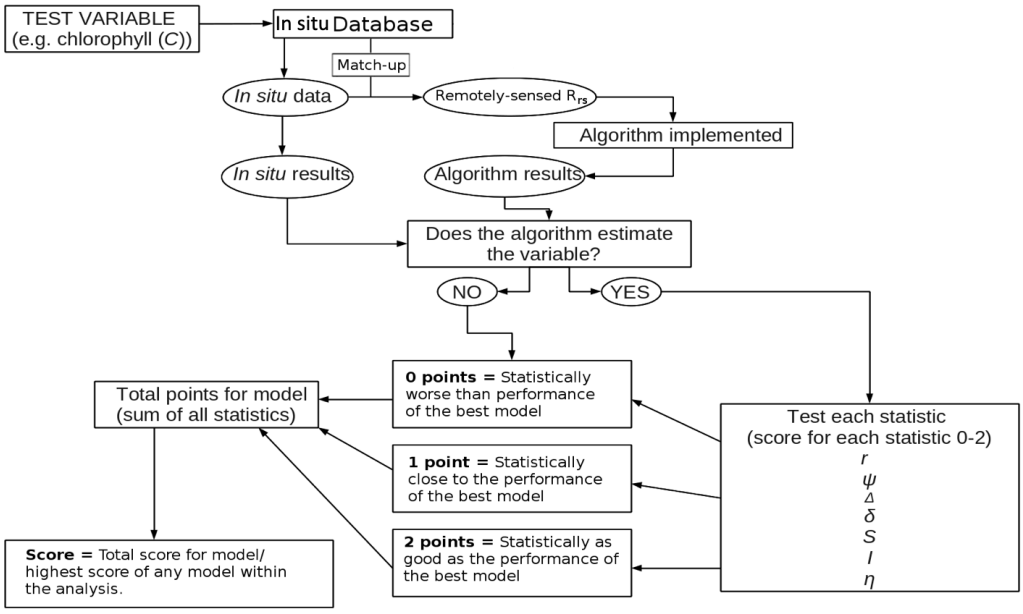

Figure 22: Flow chart of multi-metric scoring approach for Ocean Colour algorithm comparison

In order to try and account for the sensitivity of the scores to limited matchup samples, and check for stability in the scoring, the algorithms were tested with bootstrapping applied (Efron, 1979; Efron and Tibshirani, 1993). This involves using sampling with replacement to randomly re-sample the in-situ data to create 100 new datasets, each the same size as the original dataset.

The quantitative statistical methodology was then re-run for each new dataset (Monte-Carlo approach) and from the resulting distribution of scores, a mean score for each model was computed. Additionally, a 2.5 % and a 97.5 % interval on the bootstrap distribution is taken and assumed to be the confidence limits on the mean score for each model, rather than standard deviations on the bootstrap distribution, to avoid misinterpretation of results should the bootstrap distribution not follow a normal distribution or be skewed, for instance from the presence of outliers in the data.

6.3 Input data

The input data used in this assessment is the same as that described in section 2.1 with several quality filters applied after matchup between the in-situ data and satellite products. The additional filters used and the number of points they removed from the analysis are shown in Table 12.

Table 12: Filter criteria and number of points removed from analysis.

Filter name	Criteria for exclusion	Number of points removed
Invalid float values	float(chla) not valid or NaN	168280
Chl Min	Chl in-situ <0.01	3
Chl Max	Chl in-situ >100	525
Coefficient of variation	Coef_var of macro pixel > 0.2	Rrs443: 458 Rrs560: 61
Macro pixel completeness	Less than 40% of micropixel observed	26228

After this filtering, an initial investigation found that the historic data from the Elbe region had provided a large amount of data for which the chlorophyll-a estimated from the remote sensing data was significantly lower than the in-situ measurements. It can be seen in Figure 23 that the historic Elbe data have a significant concentration of high in-situ-chl-a data where the Rrs443/Rrs560 band ratio is at values we would expect at a much lower chlorophyll-a concentration (given the relationship seen in the rest of the CERTO dataset). Until the source of this anomaly is understood, we have excluded the historic Elbe data from further analysis as part of the round robin exercise.

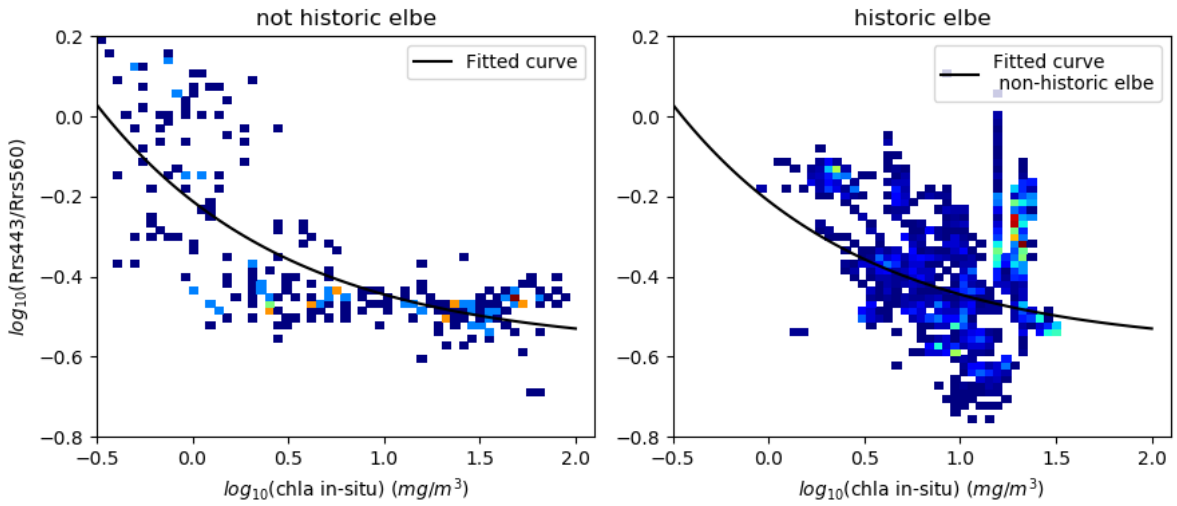

Figure 23: Comparison of the 443/560 band ratio as a function of chlorophyll-a concentration for the chlorophyll-a matchups in the Elbe historic component of the dataset with the rest of the CERTO dataset.

6.4 Assessment per optical water type

The above procedure can be run across all matchups, providing an estimate of algorithm performance across all water types, or on subsets of the matchup dataset. It is of particular interest to assess the performance of product algorithms for each of the available optical water types as this can allow a multi-algorithm blending approach similar to that used by the OC-CCI, Lakes-CCI and Copernicus Climate Change Ocean Colour data production chains. A number of approaches can be used to designate which matchups are used for the assessment of algorithms for each water class. One possible approach is to calculate the 'dominant water class' for each matchup, this being the class to which they have the highest membership score. This is not ideal as one can imagine a situation in which the membership value to two or more classes are high and similar, meaning that the single class designated as dominant is the only one using the matchup data, despite it having similar memberships to multiple classes. A second approach is to set a threshold membership value and use all matchup points with a membership to a given class above that threshold in the assessment of that class. A hybrid approach is to normalise the membership values to each class to the maximum for each point (dividing all memberships by the maximum) and setting a threshold such that the 'dominant' class is selected as one for which the matchup is used for assessment but also for any classes for which the membership is close to this dominant value. Figure 24 shows that distribution of membership values after normalising to the maximum value (giving a normalised membership of 1 for the highest membership on the right of the plot). For most of the matchup points the second highest membership value (at index 16 in the plot) usually falls between 35 and 90% of the membership to the dominant class (mean of around 0.6).

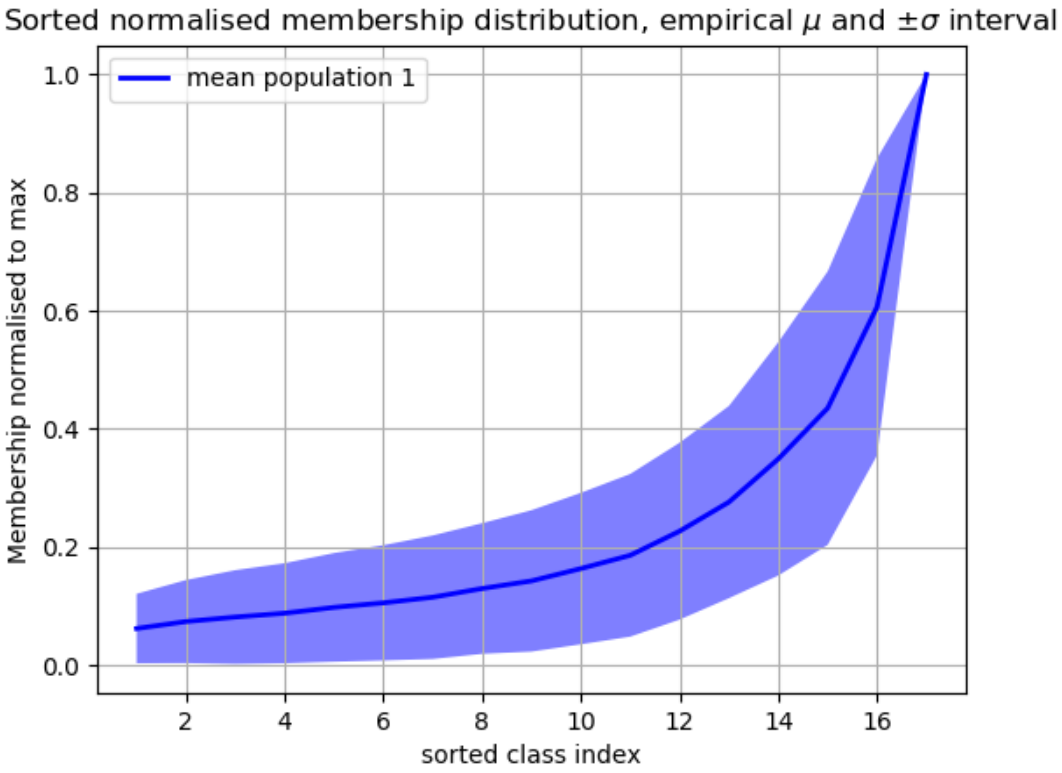

Figure 24: Distribution of normalised membership values for matchup points. Memberships are divided by the maximum value (per matchup) and then sorted numerically from lowest to highest (sorted class index on the x axis). Mean values across the dataset are shown by the hard blue line and the standard deviation is shown as a shaded region. Note that 'sorted class index' just puts the memberships per point in increasing order, the actual optical water type class at each index changes with every matchup point.

A range of threshold values were tested using the matchup dataset to see the impact on the number of clusters that each matchup point would contribute towards. This is shown in Figure 25 where with a threshold of 0.6, some of the matchup points are contributing to > 4 OWT class assessments. With incremental increases in the threshold, the number of points contributing to > 2 water class assessments falls and a value of 0.7 has been chosen for the final assessment as this allows for some shared contributions without a significant number of points contributing to > 4 assessments.

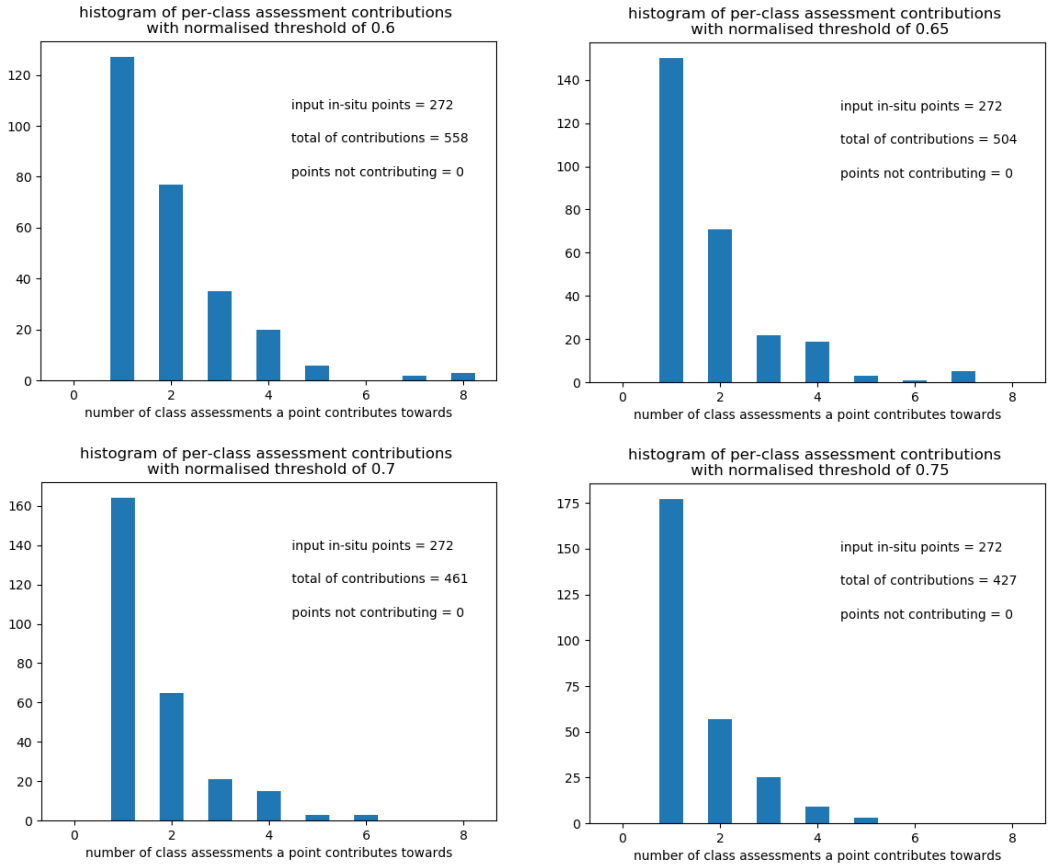

Figure 25: Histogram of the number of classes that the matchup points contribute to given different threshold for the normalised membership values.

The number of points that would be available for a per-OWT class assessment are also shown in Table 13, highlighting that using the dominant and thresholds (without normalisation) potentially underutilises the available in-situ data.

Table 13: Number of matchups passing criteria for contributing to per-optical water type class assessment.

Criteria / Water class	Dominant Class	Membership >0.3	Normalised Membership > 0.7
1	5	1	11
2	4	2	10
3	7	6	13
4	9	2	17
5	8	6	12
6	5	3	6

7	7	4	13
8	11	5	26
9	17	8	20
10	21	5	35
11	14	5	28
12	18	9	35
13	12	5	15
14	36	7	59
15	50	27	80
16	23	4	44
17	25	1	37
Total	272	100	461

6.5 Algorithms

There are two kinds of chlorophyll-a algorithms included in this intercomparison exercise: 1) empirical algorithms that make use of a formulated relationship between reflectance and chlorophyll-a concentration, derived from in-situ data; 2) quasi-analytical algorithms that make assumptions about the optical properties of some components of the marine system and then invert the measured remote sensing reflectance to derive the chlorophyll-a concentration.

Most of the empirical algorithms have an equation form with coefficients that are set for a given sensor. As OLCI is a recent ocean colour sensor, particularly OLCI 3B, there is not always a dedicated empirical parameterisation available. Additionally, some of the empirical equation coefficients were derived using a different atmospheric correction scheme to the one used within CERTO (POLYMER). Therefore, some of the algorithms implemented in the round robin make use of 'OLCI' parameterisations and some have to fall back on 'MERIS' parameterisations (as MERIS is the most OLCI-like sensor from the historical record).

The algorithms are all summarised below with references given for further information.

The NASA Ocean Colour 2 (OC2) algorithm

The NASA OC2 chlorophyll algorithm (O'Reilly et al., 2019) uses a polynomial relationship between a log-transformed two band ratio (X) and the chlorophyll-a concentration. The band ratio is taken with a blue wavelength (closest to 490nm) and a green wavelength (usually the instrument band that falls within 545nm to 570nm). For OLCI the blue and green wavelengths are 490nm and 560nm respectively.

$$X = log_{10}\left(\frac{R_{rs}(\lambda_b)}{R_{rs}(\lambda_g)}\right) \tag{12}$$

The polynomial fit to the data is then of the form:

$$log_{10}(Chl) = a_0 + a_1X + a_2X^2 + a_3X^3 + a_4X^4 \tag{13}$$

where a_0 to a_4 are the fitted coefficients and for OLCI these are 0.1731,-3.963,-0.562,4.5008,-3.002 respectively (Warren et al 2021).

The NASA Ocean Colour 3 (OC3) algorithm

The NASA OC3 chlorophyll-a algorithm uses the same polynomial form as the OC2 but uses three wavebands for the calculation of X such that the blue wavelength is the maximum R_{rs}

value over a defined range. For OLCI this is range includes the 443 and 490nm bands such that:

$$X = log_{10}\left(\frac{\max[R_{rs}(\lambda_{b1}), R_{rs}(\lambda_{b2})]}{R_{rs}(\lambda_g)}\right) \quad (14)$$

Where λ_{b1} is 443nm and λ_{b2} is 490nm. The values of a_0 to a_4 for OLCI are then 0.2521,-2.2146,1.5193,-0.7702,-0.4291 respectively (Warren et al 2021).

The NASA Ocean Colour 4 (OC4) algorithm

The NASA OC4 chlorophyll-a algorithm also uses the same polynomial form as the OC2 and OC3, but uses four wavebands for the calculation of *X* such that the blue wavelength is the maximum R_{rs} value over a defined range. For OLCI this is range includes the 443nm, 490nm and 510nm bands such that:

$$X = log_{10}\left(\frac{max[R_{rs}(\lambda_{b1}), R_{rs}(\lambda_{b2}), R_{rs}(\lambda_{b3})]}{R_{rs}(\lambda_g)}\right) \quad (15)$$

where λ_{b1} is 443nm, λ_{b2} is 490nm and λ_{b3} is 510nm. Two parameterisations of the OC4 algorithm were tested 1) using the older SeaDAS MERIS coefficient values of 0.3255, -2.7677, 2,4409, -1.1288, and -0.4990 for a_0 to a_4 and 2) the OC4_v7 OLCI parameterisation with 0.42540,-3.21679,2.86907,-0.62628,-1.09333 (O'Reilly & Werdell 2019).

The OC4 Mediterranean parameterisation (OC4_Med) algorithm

The OC4_Med algorithm in this round robin uses the OC4 equation given above but with the coefficients of a_0 to a_4 are set as 0.131,-3.873,3.901,-1.689,-0.369 following Volpe et al (2019) optimisation for MERIS.

The Ocean Colour 5 band (OC5) algorithm

Within this round robin there are two algorithms that have been named OC5. This first of these is named OC5_NASA from here onwards and is documented by O'Reilly et al. (2019) which follows the same form as OC2, OC3 and OC4 algorithms with the addition of $R_{rs}(\lambda_{b4})$ to the consideration of maximum band ratio where λ_{b4} is 413nm. The coefficients for a_0 to a_4 are 0.43213,-3.13001,3.05479,-1.45176,-0.24947.

The second OC5 algorithm (called simply OC5 from here on) refers to that of Gohin et al. (2002). This algorithm determines chlorophyll-a concentrations from triplet values of OC4 (as parameterised for MERIS) maximum band ratio, nLw(412) and nLw(560), using a Look Up Table (LUT), based on the relationships between measured Chl-a and satellite $R_{rs}(\lambda)$ from observations in the English Channel and Bay of Biscay (Gohin et al., 2002). The method has also been extended to the Mediterranean Sea and applied to MODIS-Aqua and MERIS (Gohin, 2011).

The NASA Ocean Colour 6 (OC6) algorithm

The NASA OC6 chlorophyll-a algorithm uses the same polynomial form as all the OC(x) algorithms, but uses six wavebands for the calculation of *X* such that numerator (blue wavelength) is the maximum R_{rs} value over a defined range (413,443,490,510nm) and the denominator is now the mean of the green and red bands (560nm and 665nm).

$$X = log_{10}\left(\frac{max[R_{rs}(\lambda_{b1}), R_{rs}(\lambda_{b2}), R_{rs}(\lambda_{b3}), R_{rs}(\lambda_{b4})]}{mean(R_{rs}(\lambda_g), R_{rs}(\lambda_r))}\right) \quad (15)$$

The OC6 OLCI parameterisation from O'Reilly & Werdell (2019) sets a_0 to a_4 as 0.95039,-3.05404,2.17992,-1.12097,0.15262 for OLCI.

The Ocean Colour Index (OCI) algorithm

The Ocean Colour Index (OCI) chlorophyll algorithm was developed by Hu et al. (2012). This empirical algorithm was designed to improve the estimate of chlorophyll (C) in the global ocean at chlorophyll-a concentrations ≤0.25 mg m^{-3}. It was slightly reformulated and reparametrised for OLCI in Cazzaniga et al (2018). Firstly, a colour index (CI) is calculated according to:

$$CI = R_{rs,\lambda_2} - \left[R_{rs,\lambda_1} + \left(\frac{\lambda_2 - \lambda_1}{\lambda_3 - \lambda_1}\right)\left(R_{rs,\lambda_3} - R_{rs,\lambda_1}\right)\right], \quad (16)$$

where for OLCI λ_1, λ_2, and λ_3 are 443, 560 and 665.

$$Chl_{CI} = 10^{aCI+b} \quad (17)$$

where *a is* 180.9642 and *b* is -0.5379.

There then follows a blending of the CI estimate of chlorophyll-a at low chlorophyll-a concentrations with the NASA OCx algorithm at higher concentrations occurs between chlorophyll-a concentrations of 0.12 and 0.2 mg m^{-3}, meaning that:

$$Chl_{OCI} = \begin{cases} Chl_{CI} & if\ Chl_{CI} < 0.12 \\ \left(Chl_{OCx}\left(\frac{Chl_{mean} - 0.12}{0.08}\right)\right) + \left(Chl_{CI}\left(1 - \left(\frac{Chl_{mean} - 0.12}{0.08}\right)\right)\right) & if\ 0.12 < Chl_{CI} < 0.2 \\ Chl_{OC_x} & if\ Chl_{CI} > 0.2 \end{cases} \quad (18)$$

Where Chl_{mean} is the average of the two algorithm estimates.

The Ocean Colour Index 2 (OCI2) algorithm

The OCI2 algorithm is the updated version of the OCI algorithm as specified in Hu et al. 2019. This follows the same formulation as the OCI algorithm above but the coefficients *a* and *b* in equation 17 are set to 230.47 and -0.4287 such that:

$$Chl_{CI2} = 10^{230.47CI - 0.4287}, \quad (19)$$

and the blending thresholds are updated in equation 18 to give:

$$Chl_{OCI2} = \begin{cases} Chl_{CI2} & if\ Chl_{CI} < 0.25 \\ \left(Chl_{CI2}\left(\frac{0.4 - Chl_{CI2}}{0.15}\right)\right) + \left(Chl_{OC_x}\left(\frac{Chl_{CI2} - 0.25}{0.15}\right)\right) & if\ 0.25 < Chl_{CI} < 0.4 \\ Chl_{OC_x} & if\ Chl_{CI} > 0.4 \end{cases} \quad (20)$$

The Ocean Colour 5 band plus Colour Index (OC5CI) algorithm

The OC5CI algorithm is a blended algorithm which follows equation 17 but blends the CI Chlorophyll-a estimate with that of the OC5 algorithm described above and the blending window is set to 0.1 to 0.15 mg m^{-3}. This yields:

$$Chl_{OC5CI} = \begin{cases} Chl_{CI} & if\ Chl_{CI} < 0.1 \\ \left(Chl_{CI} \times \left(\frac{0.15 - Chl_{CI}}{0.05}\right)\right) + \left(Chl_{OC5} \times \left(\frac{Chl_{CI} - 0.1}{0.05}\right)\right) & if\ 0.1 < Chl_{CI} < 0.15 \\ Chl_{OC5} & if\ Chl_{CI} > 0.15 \end{cases} \quad (21)$$

The OCx band ratio algorithm

The NASA OCx algorithm (O'Reilly et al., 2000) as implemented in SeaDAS 7.5.3 implements the OC2, OC3 or OC4 algorithms depending upon which sensor is being processed. As we are processing data that is band shifted and bias corrected to appear as OLCI data, this algorithm is functionally identical to the OC4 algorithm in this case.

Two band NIR algorithm (Gdal)

This algorithm refers to the two-band ratio algorithm of Dall'Olmo et al. (2003), originally proposed by Gitelson and Kondratyev (1991) and later adapted to MERIS/OLCI bands. This is an empirical formula based on a linear relationship between in-situ Chla and the ratio of MERIS NIR and Red band remote sensing reflectance:

$$Chl = a\left(\frac{R_{rs}(709)}{R_{rs}(665)}\right) + b, \quad (22)$$

Where a and b are 61.324 and -37.94 respectively.

Three Band Gitelson Algorithm

This algorithm was developed by Moses er al (2009) and updated by Gitelson et al (2011). Chl is estimated using a relationship between bands in the Red/NIR range following:

$$Chl = a\left(R_{rs}(754)\left(\frac{1}{R_{rs}(665)} - \frac{1}{R_{rs}(709)}\right)\right) + b, \quad (23)$$

Where a and b are 232.329 and 23.174 respectively.

Two Band algorithm of Gurlin

This algorithm is the two-band algorithm of Gurlin et al (2011) and estimates Chl following:

$$Chl = a\left(\frac{R_{rs}(709)}{R_{rs}(665)}\right)^2 + b\left(\frac{R_{rs}(709)}{R_{rs}(665)}\right) + c, \quad (24)$$

Where a, b and c are 25.28, 14.85 and-15.18 respectively.

Three Band Algorithm of Gurlin

This algorithm is the two-band algorithm of Gurlin et al (2011) and estimates Chl following:

$$Chl = a\left(R_{rs}(754)\left(\frac{1}{R_{rs}(665)} - \frac{1}{R_{rs}(709)}\right)\right)^2 + b\left(R_{rs}(754)\left(\frac{1}{R_{rs}(665)} - \frac{1}{R_{rs}(709)}\right)\right) + c, \quad (25)$$

Where a, b and c are 315.5, 215.95 and 25.66 respectively.

Two band semi analytical algorithm of Gilerson

This algorithm refers to the two-band algorithm of Gilerson et al (2010) and estimates Chl following:

$$Chl = \left(a\left(\frac{R_{rs}(709)}{R_{rs}(665)}\right) + b\right)^c, \quad (26)$$

Where a, b and c are 35.745, -19.295 and 1.124 respectively.

Three band semi analytical algorithm of Gilerson

This algorithm refers to the three-band algorithm of Gilerson et al (2010) and estimates Chl using NIR and red bands along with estimates of water and phytoplankton absorption. Following Neil et al (2019) this can be represented as:

$$Chl = \left(a\left(R_{rs}(753)\left(\frac{1}{R_{rs}(665)} - \frac{1}{R_{rs}(709)}\right)\right) + b\right)^c, \quad (27)$$

Where a, b and c are 113.36, 16.45 and 1.124 respectively.

Three band semi analytical algorithm of Gilerson

This algorithm refers to the three-band algorithm of Gilerson et al (2010) and estimates Chl using NIR and red bands along with estimates of water and phytoplankton absorption. Following Neil et al (2019) this can be represented as:

$$Chl = \left(a\left(R_{rs}(753)\left(\frac{1}{R_{rs}(665)} - \frac{1}{R_{rs}(709)}\right)\right) + b\right)^c, \quad (28)$$

Where a, b and c are 113.36, 16.45 and 1.124 respectively.

Band index algorithm of Yang

This algorithm refers to the three-band algorithm of Yang et al (2010) and estimates Chl using NIR and red bands:

$$Chl = a\frac{\left(\frac{1}{R_{rs}(665)} - \frac{1}{R_{rs}(708)}\right)}{\left(\frac{1}{R_{rs}(753)} - \frac{1}{R_{rs}(708)}\right)} + b, \quad (29)$$

Where a, b are 161.24, and 28.04 respectively.

Normalised difference chlorophyll index (NDCI) algorithm of Mishra
This algorithm refers to the two-band algorithm of Mishra and Mishra (2012) and estimates Chl using NIR and red bands:

$$Chl = a + b\frac{(R_{rs}(709) - R_{rs}(665))}{(R_{rs}(709) + R_{rs}(665))} + c\left(\frac{\left(R_{rs}(709) - R_{rs}(665)\right)}{\left(R_{rs}(709) + R_{rs}(665)\right)}\right)^2, \qquad (30)$$

Where a, b and c are 42.197, 236.5 and 314.97 respectively.

There is also a version of this algorithm parameterised using a, b and c values of 14.039, 86.115 and 194.325 which is referred to here as NDCI2.

Maximum Peak Height (MPH) algorithm of Matthews
This algorithm refers to the five-band algorithm of Matthews et al. (2012). This algorithm selects the maximum reflectance across 3 bands and compares it to a baseline determined across a wider spectral range. This peak height is then used to derive a chlorophyll estimate.

$$MPH = max[R_{rs}(\lambda_{b1}), R_{rs}(\lambda_{b2}), R_{rs}(\lambda_{b3})] - R_{rs}(\lambda_{b1}) - \left((R_{rs}(\lambda_{b4}) - R_{rs}(\lambda_{b1}))\left(\frac{\lambda_{max} - \lambda_{b1}}{\lambda_{b4} - \lambda_{b1}}\right)\right), \qquad (31)$$

Where λ_{b1} is 665nm, λ_{b2} is 681nm, λ_{b3} is 709nm and λ_{b4} is 865nm.

Then chl is calculated as:

$$Chl = aMPH^4 + bMPH^3 + cMPH^2 + dMPH + e\,, \qquad (32)$$

Where a, b, c, d and e are $5.24\text{x}10^9$, $-1.95\text{x}10^8$, $2.46\text{x}10^6$, $4.02\text{x}10^3$, and 1.97 respectively.

6.6 Results

Across the 17 OWT classes assessed as part of the round robin exercise, a range of candidate algorithms could be considered as optimal.

Table 14 shows a summary of those algorithms that performed well in each OWT class. Those algorithms performing best were considered prime (P) and those who also performed reasonably (but worse than the prime algorithms) were considered secondary (S).

When considering all the results below, it is worth noting that the matchups that made it through the filtering process biased the samples to relatively high chl-a concentrations, with all in-situ chl-a measurements > 0.1 mg/m^3 and most of the measurements > 1.0 mg/m^3 as shown in Figure 26.

In some cases, multiple algorithms performed indistinguishably well and so there is not a single P or S given in the table. Water class 6 had insufficient in-situ data to make any clear decisions on algorithm performance. A subset of the algorithms performed poorly in almost all cases (never achieving an S or P status) and these are OC6, GilSA3, Yang and MPH.

It is also of note that some of the algorithms provided significantly fewer matchups (around half of the 283 matchups) due to the creation of negative or invalid (not-a-number NaN) chl-a estimates (Gdal, OC5, Git and GilSA3).

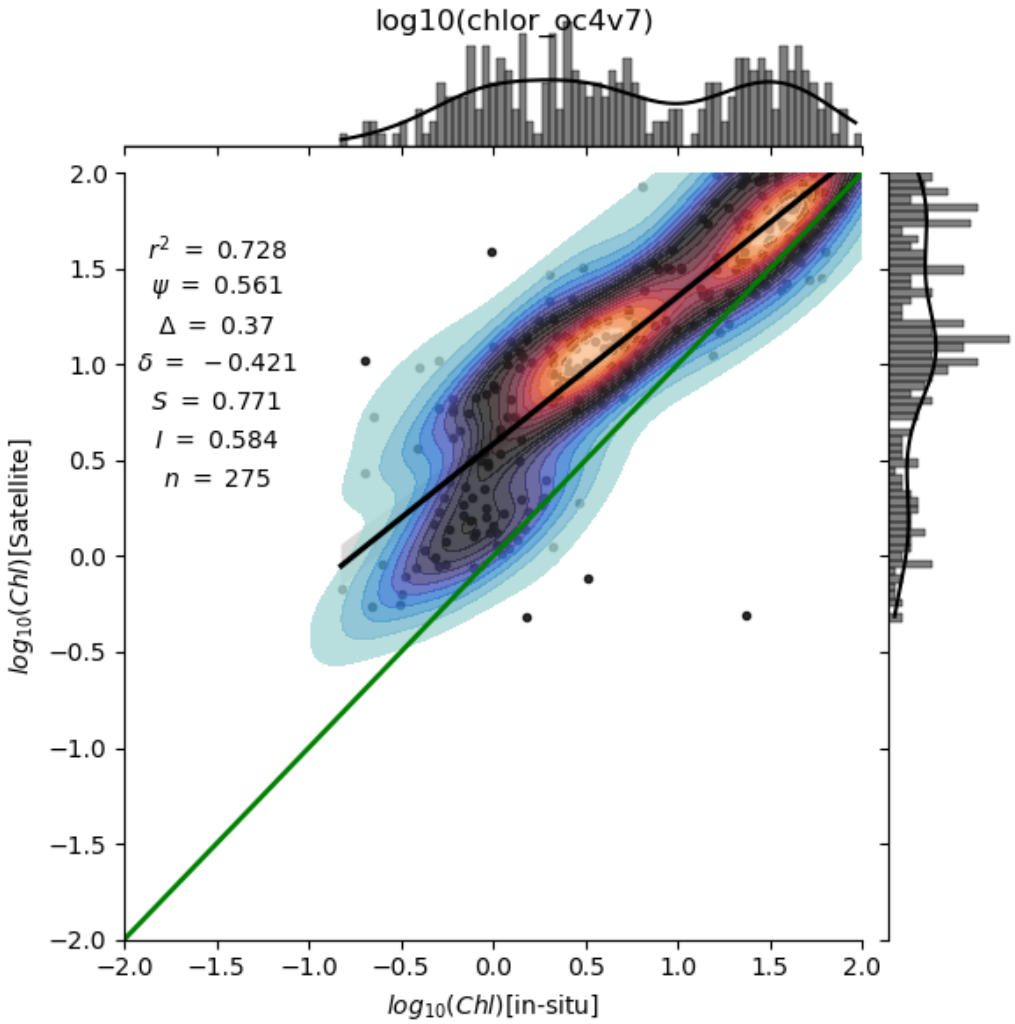

Figure 26: Performance of the OC4V7 algorithm using the CERTO matchups against POLYMER processed OLCI data across all optical water types.

Table 14: Summary of Prime (P) and Secondary (S) algorithms for each optical water type class.

Waterclass ->	1	2	3	4	5	6	7	8	9	10	11	12	13	14	15	16	17
Algorithm																	
ocx			S				S						S				
oc2									S	S							P
oc3			S				S						S				
oc4			P														
oc4v7			P		P												
oc5nasa	P	P															
oc6																	
oc4med	S			S	P		S		P								P
oci			S				S						S				
oci2							P						P				S
oc5	S	S		S	P							P		S			
oc5ci	S	S		S	P							P					
Gdal	S			P				P		P				P	S	S	
Git										P	P						P
Gur2										S	S				P	P	S
Gur3												S		S			
GilSA2				S				P						S	S	P	S
GilSA3																	
Yang																	
NDCI											P	S			P		
NDCI2														P			
MPH																	

In order to provide some insight into why these algorithms might be producing so many invalid results, we looked at the average Rrs spectra for those matchups that provided valid and invalid values for each of the 4 algorithms mentioned above. These are shown in Figure 27 to 30. Note in these figures that the Git, GilSA3 and Gdal algorithms seem to fail more often when there is a less significant red chl-a peak and the OC5 algorithm seems to fail when there is a stronger red chl-a peak.

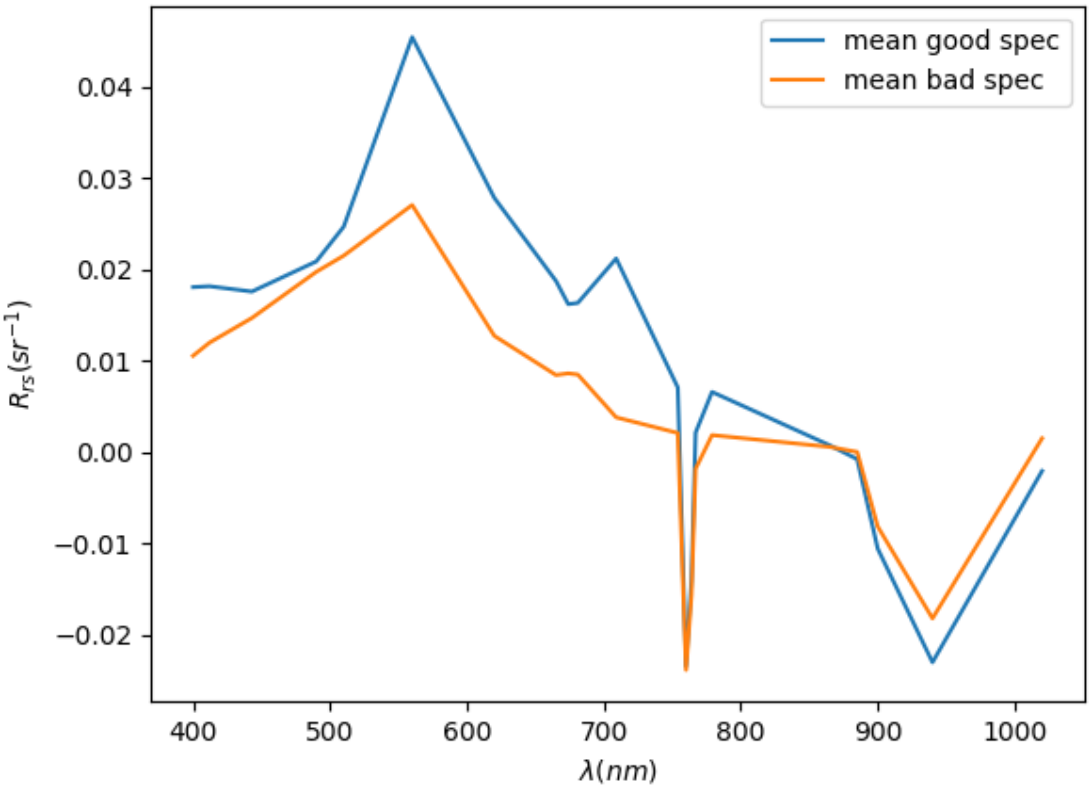

Figure 27: Mean spectra from the valid and invalid chl-a results using the Gdal Algorithm

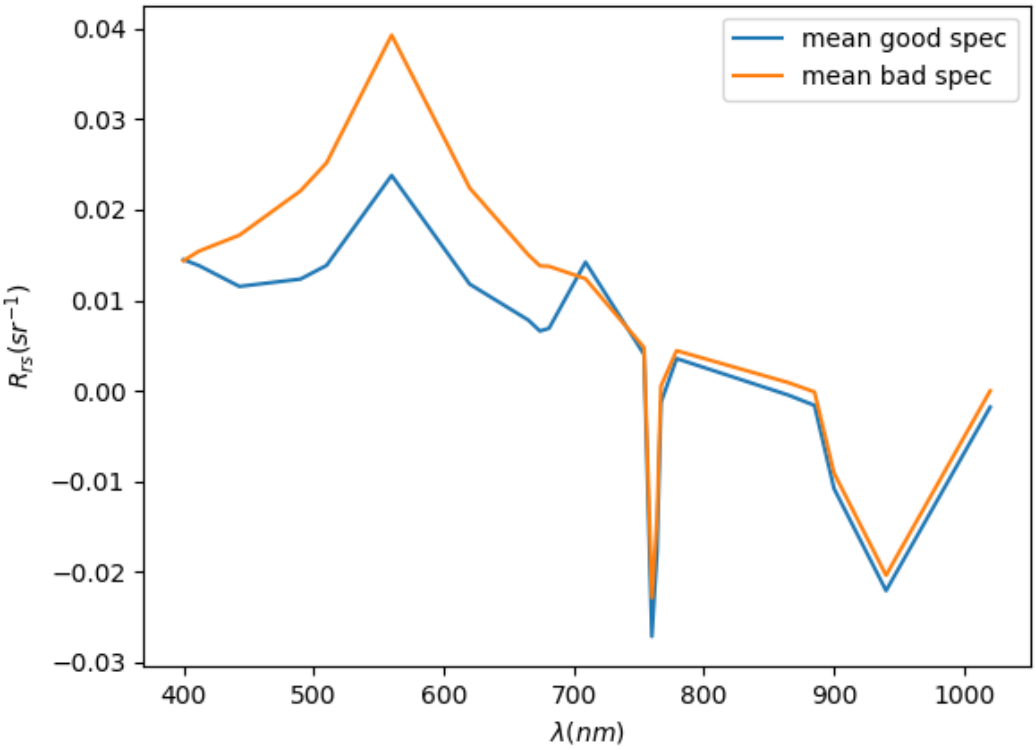

Figure 28: : Mean spectra from the valid and invalid chl-a results using the GilSA3 Algorithm

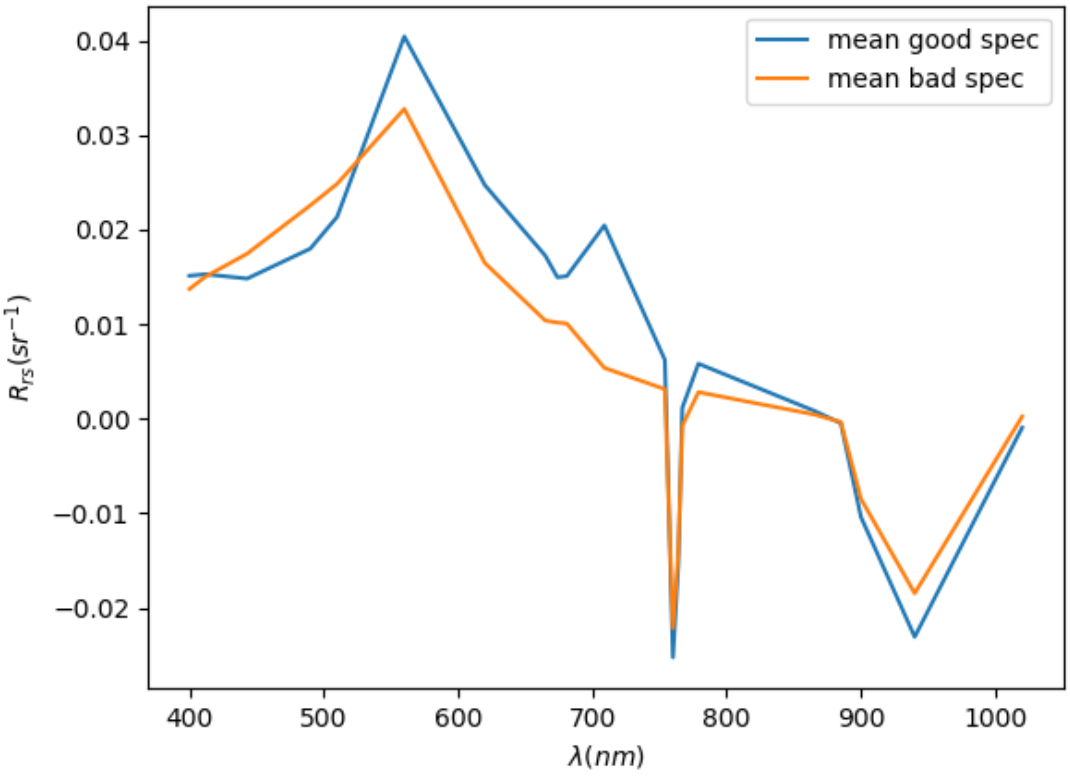

Figure 29: Mean spectra from the valid and invalid chl-a results using the Git Algorithm

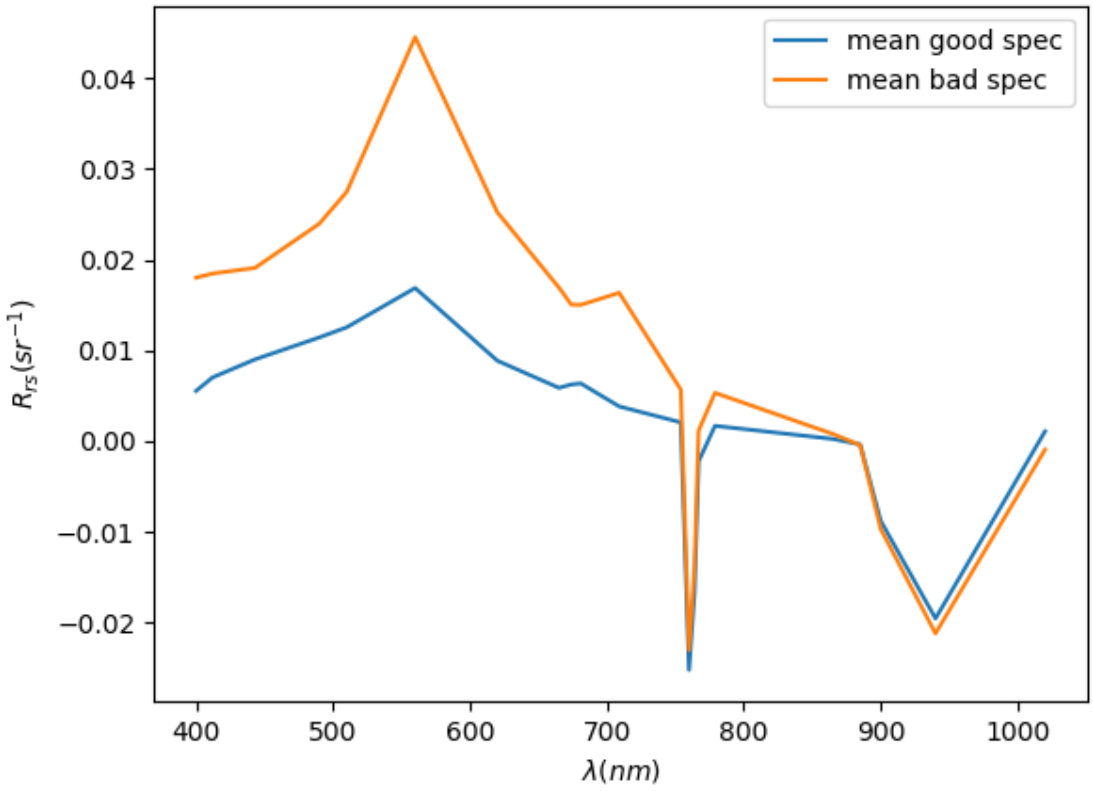

Figure 30: Mean spectra from the valid and invalid chl-a results using the OC5 Algorithm

Where multiple prime algorithms were suggested by the automated round-robin process, further analysis was performed by inspection of the matchup results with a focus on reducing largely anomalous values that could significantly impact blended results, which is done through increasing the importance of the RMSE and slope metrics in the analysis.

6.7 Recommendations

The following table gives the recommended algorithm to use for the estimation of chlorophyll-a in each of the optical water type classes within the CERTO set. Nine algorithms may seem a lot to consider across a range of 17 OWT classes but this is perhaps a reflection of the range in optical water conditions that the CERTO project covers.

Table 15. Recommended algorithm to use for the estimation of chlorophyll-a in each of the optical water type classes within the CERTO set.

Optical Water Type Class	Recommended Algorithm
1	OC5NASA
2	OC5NASA
3	OC4v7
4	Gdal
5	OC4med
6	OC4med
7	OCi2
8	Gdal

9	OC4med
10	Gdal
11	NDCI
12	OC5ci
13	OCI2
14	Gdal
15	Gur2
16	Gur2
17	Git

The matchup performance plot for each of the optimal algorithms is shown below (Figure 31 to Figure 46).

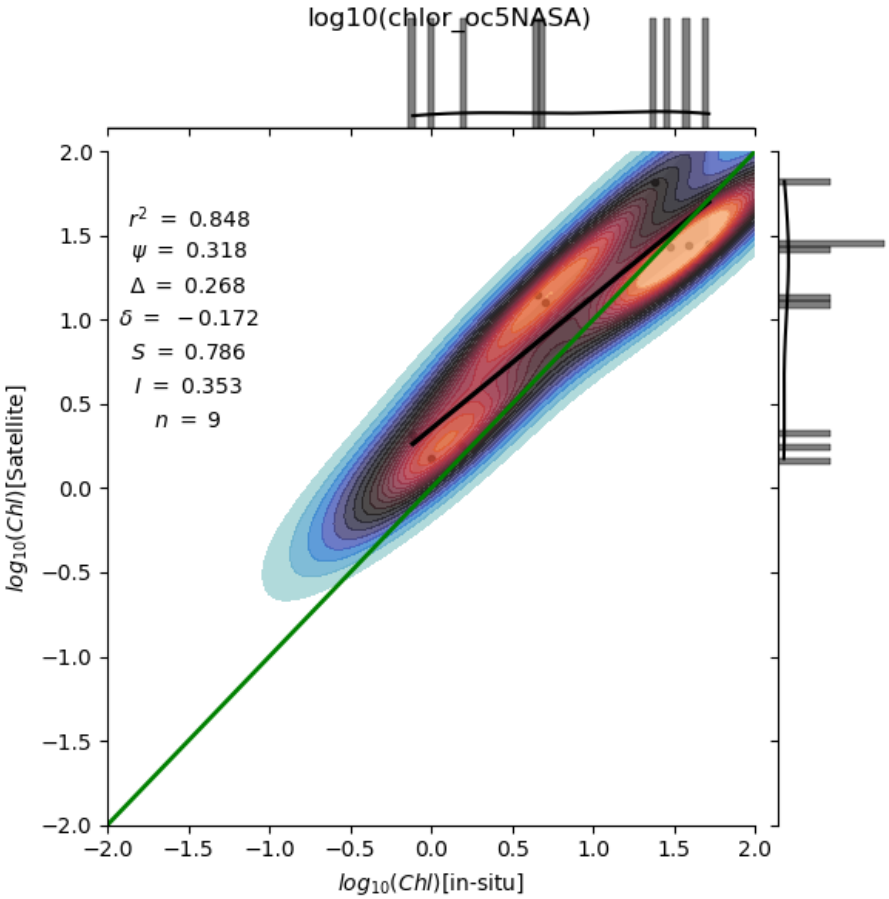

Figure 31: Optical Water Type class 1 optimal algorithm (OC5NASA) performance plot

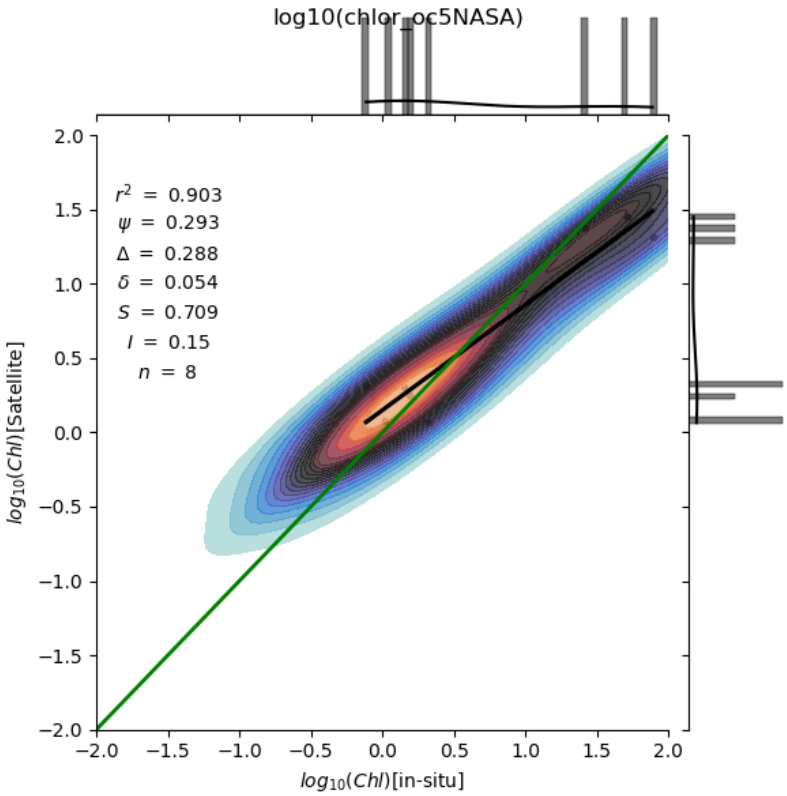

Figure 32: Optical Water Type class 2 optimal algorithm (OC5NASA) performance plot

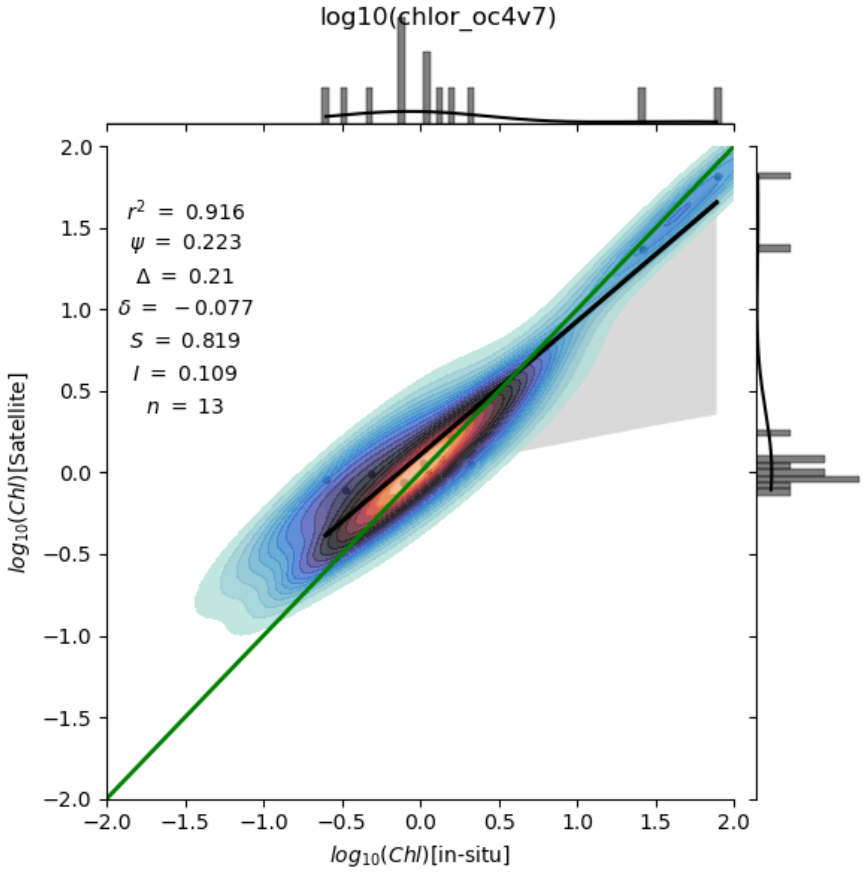

Figure 33: Optical Water Type class 3 optimal algorithm (OC4v7) performance plot

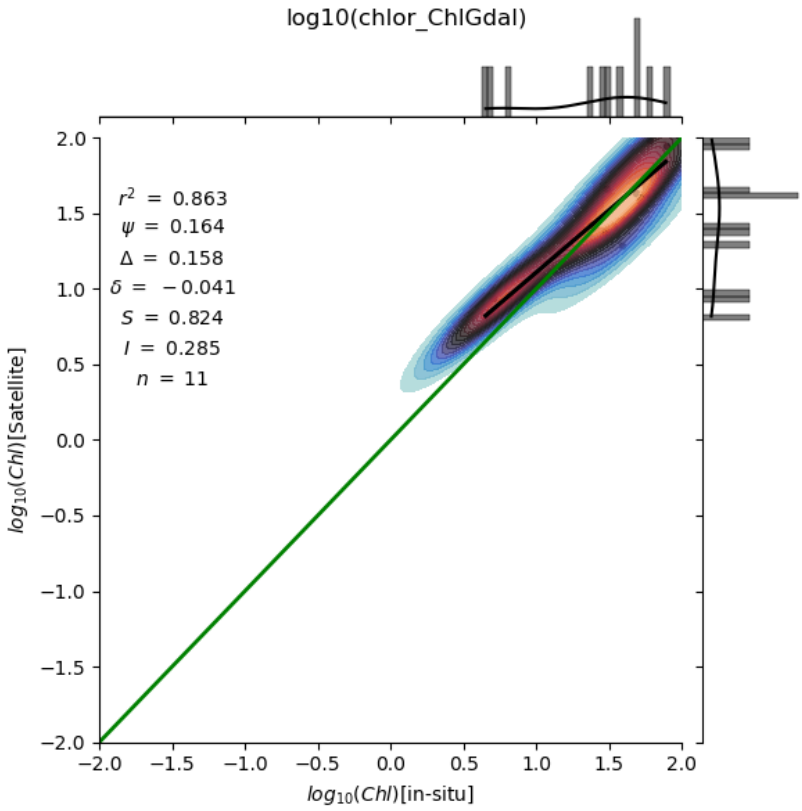

Figure 34: Optical Water Type class 4 optimal algorithm (Gdal) performance plot

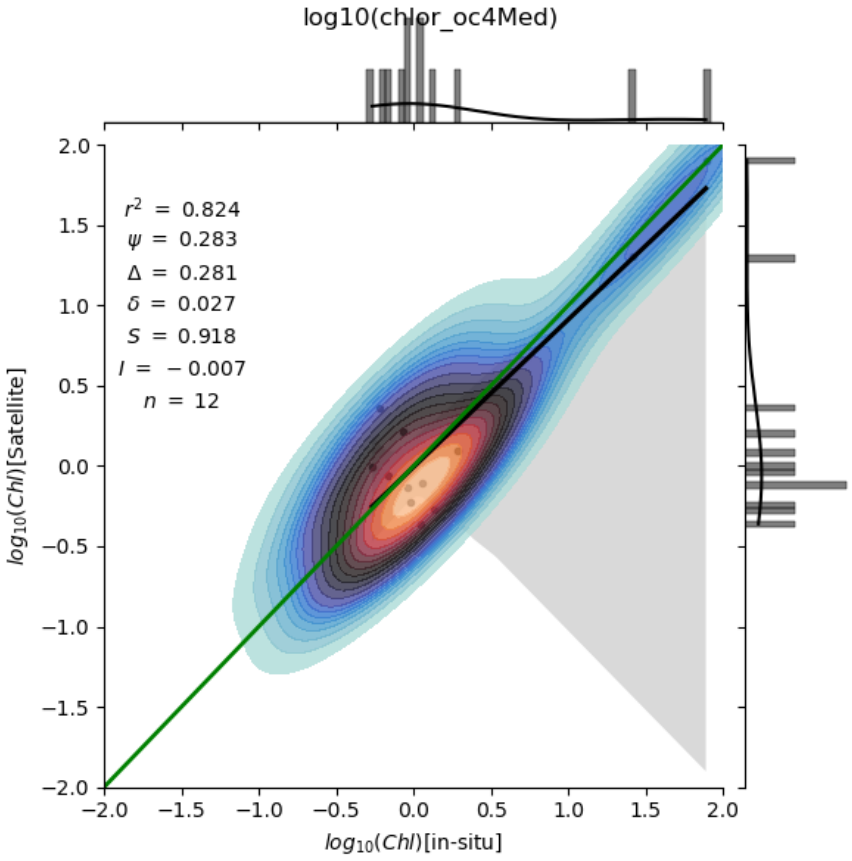

Figure 35: Optical Water Type class 5 optimal algorithm (OC4med) performance plot

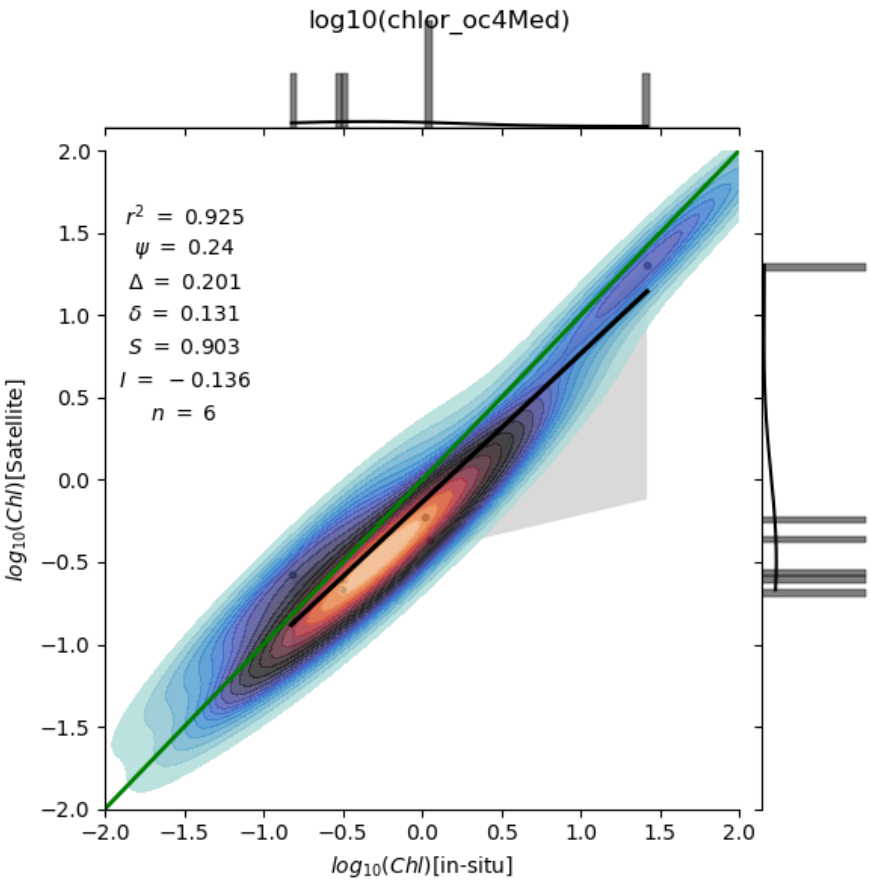

Figure 37: Optical Water Type class 6 optimal algorithm (OC4med) performance plot

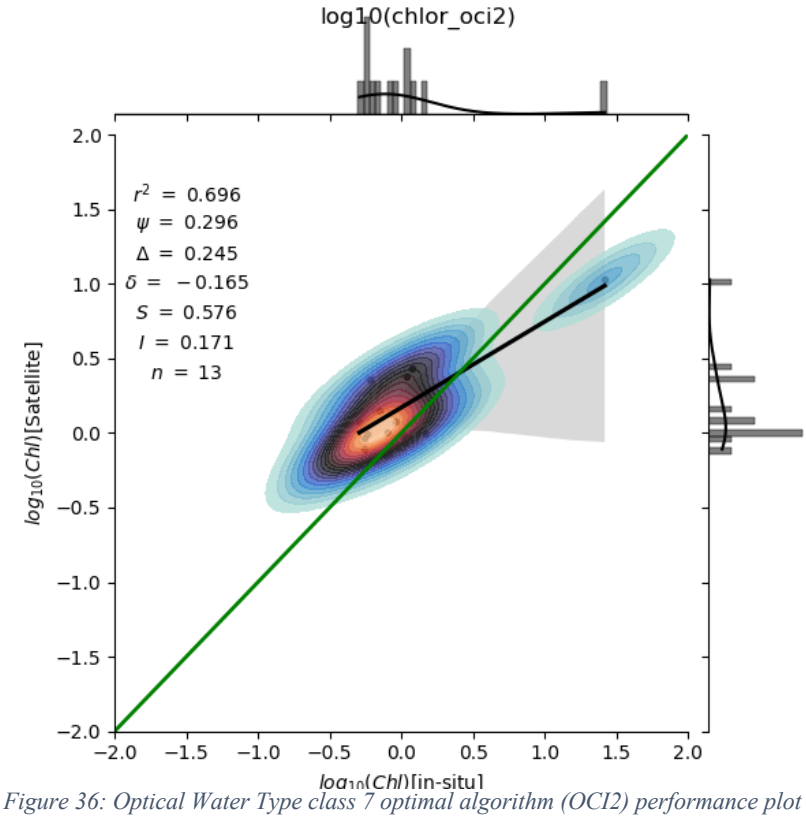

Figure 36: Optical Water Type class 7 optimal algorithm (OCI2) performance plot

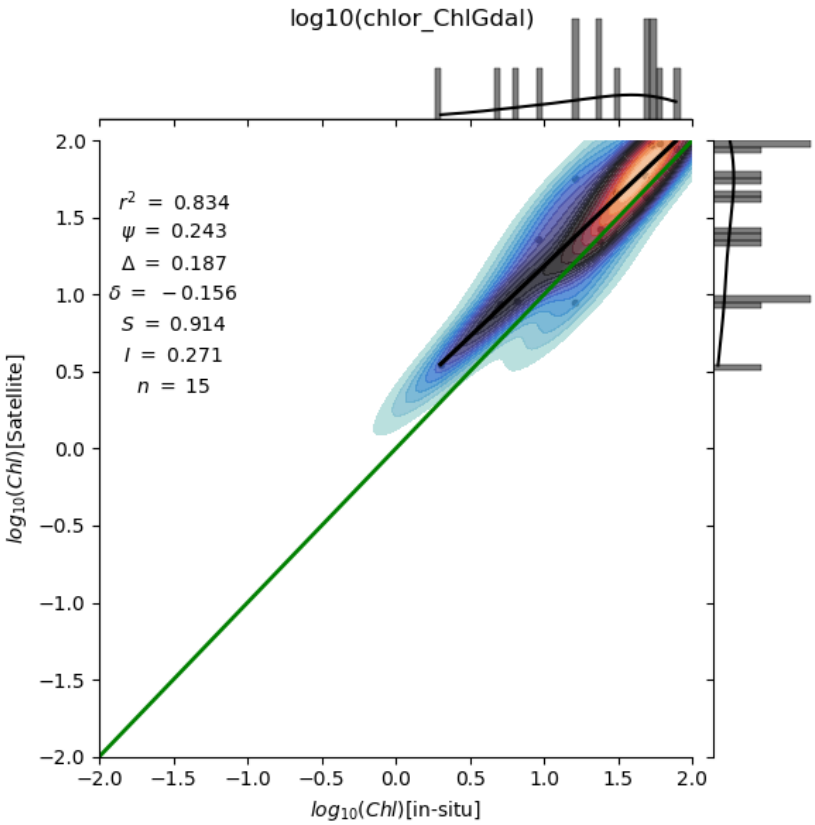

Figure 39: Optical Water Type class 8 optimal algorithm (Gdal) performance plot

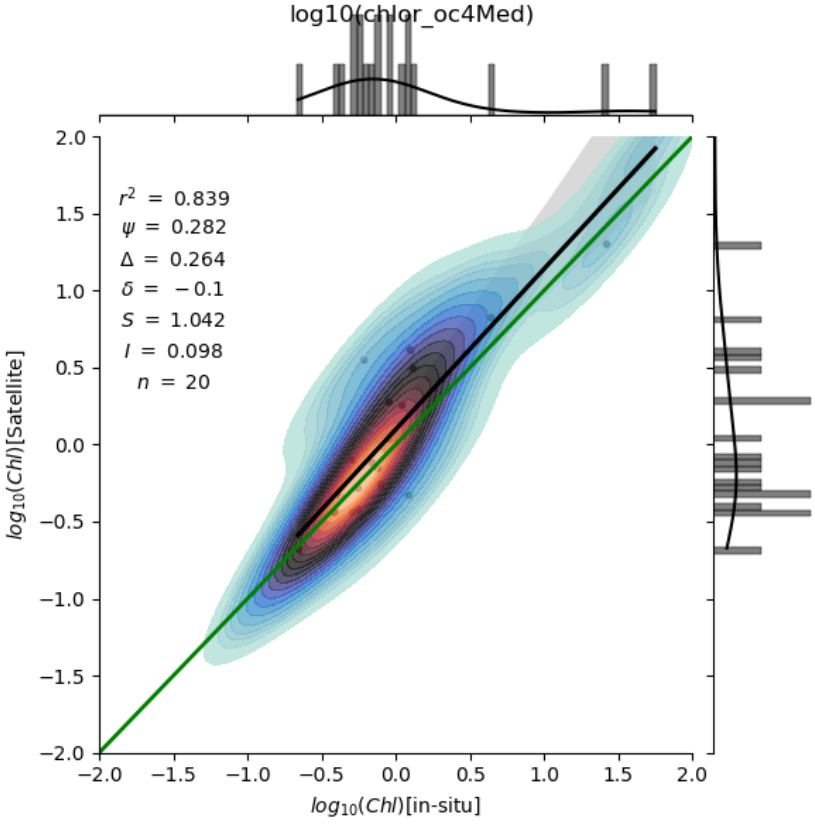

Figure 38: Optical Water Type class 9 optimal algorithm (OC4med) performance plot

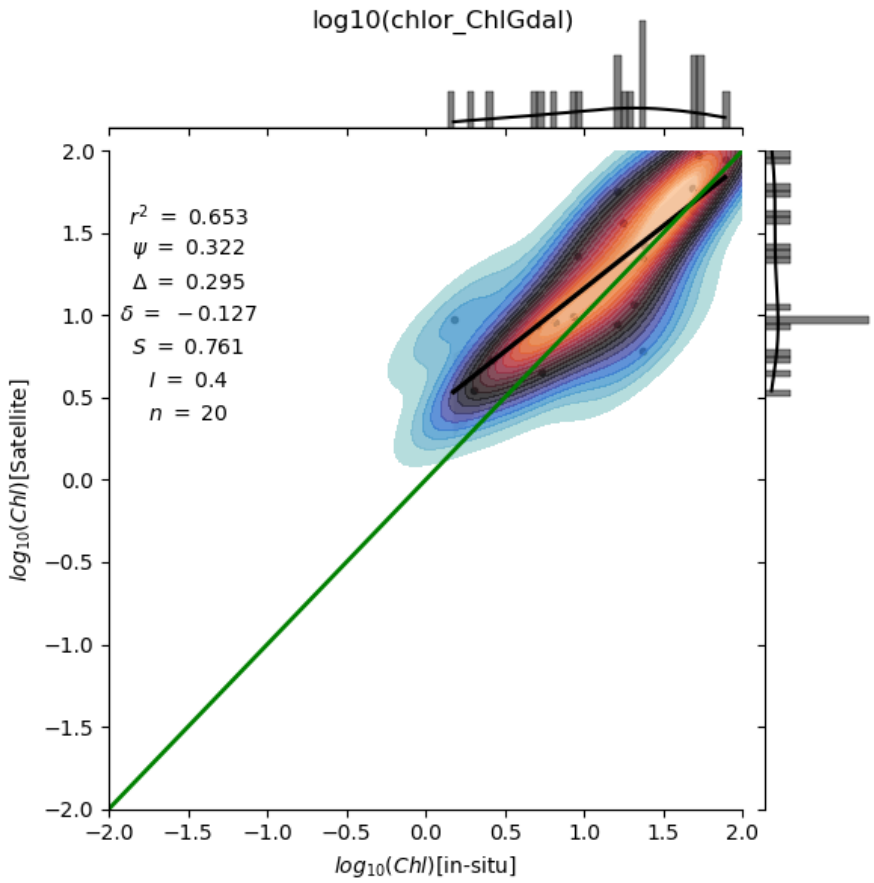

Figure 41: Optical Water Type class 10 optimal algorithm (Gdal) performance plot

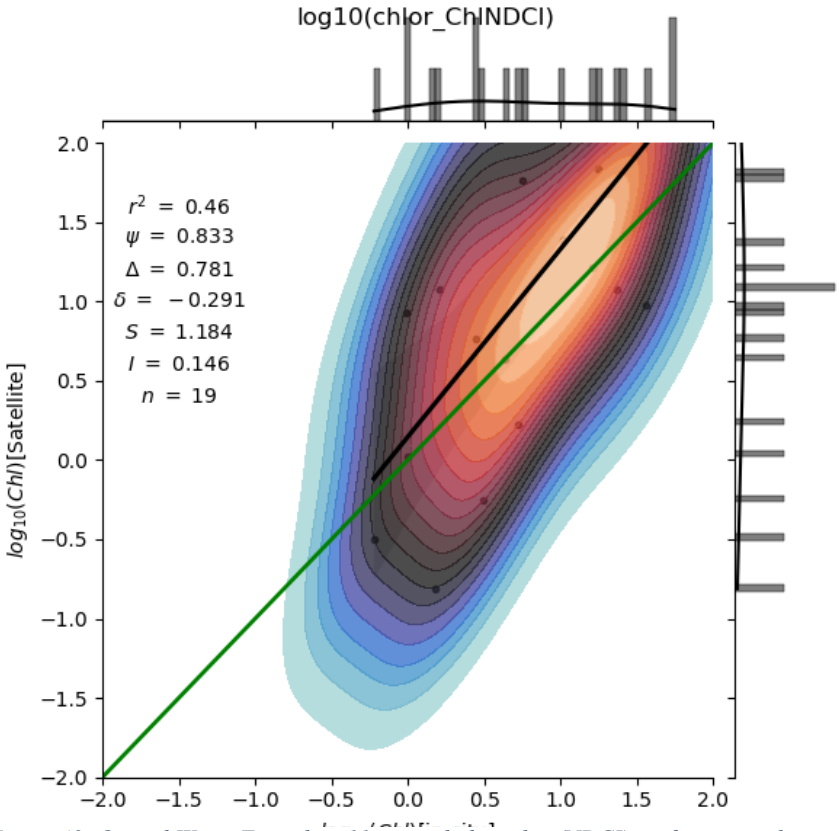

Figure 40: Optical Water Type class 11 optimal algorithm (NDCI) performance plot

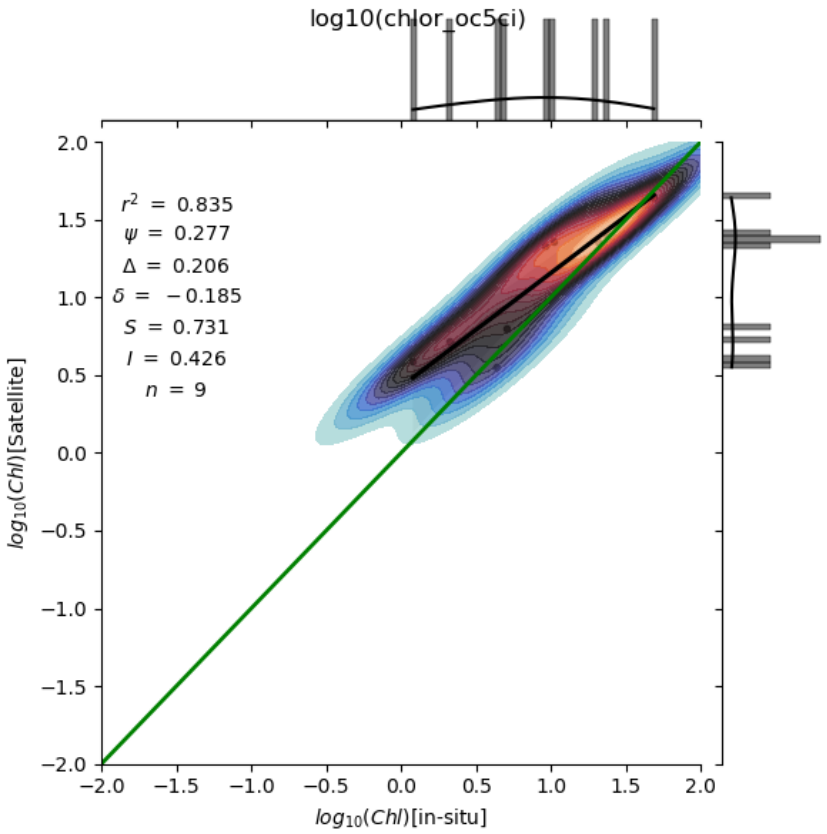

Figure 43: Optical Water Type class 12 optimal algorithm (OC5CI) performance plot

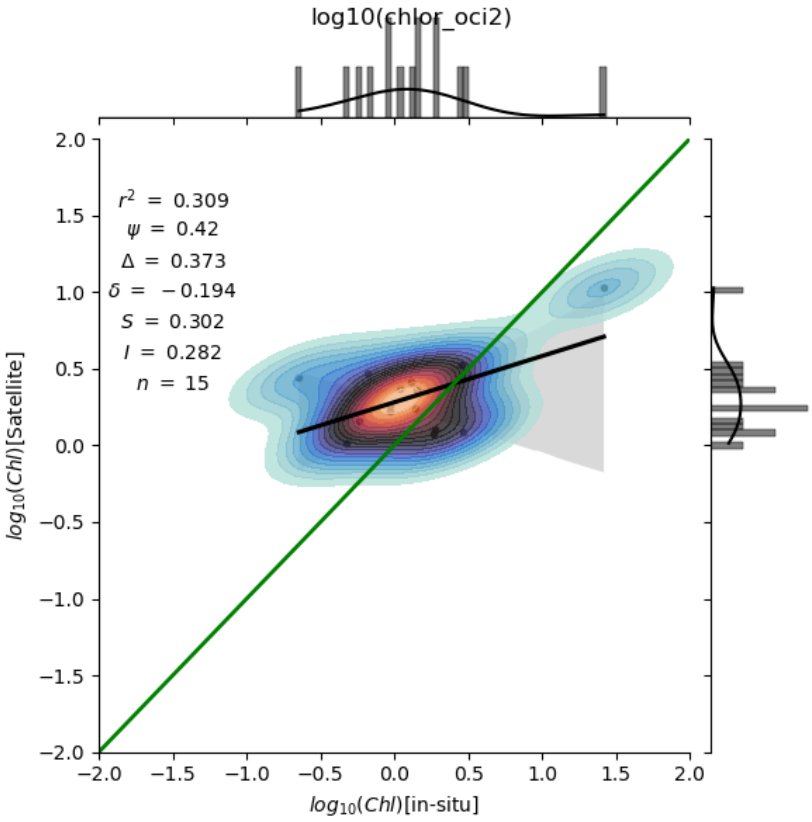

Figure 42: Optical Water Type class 13 optimal algorithm (OCI2) performance plot

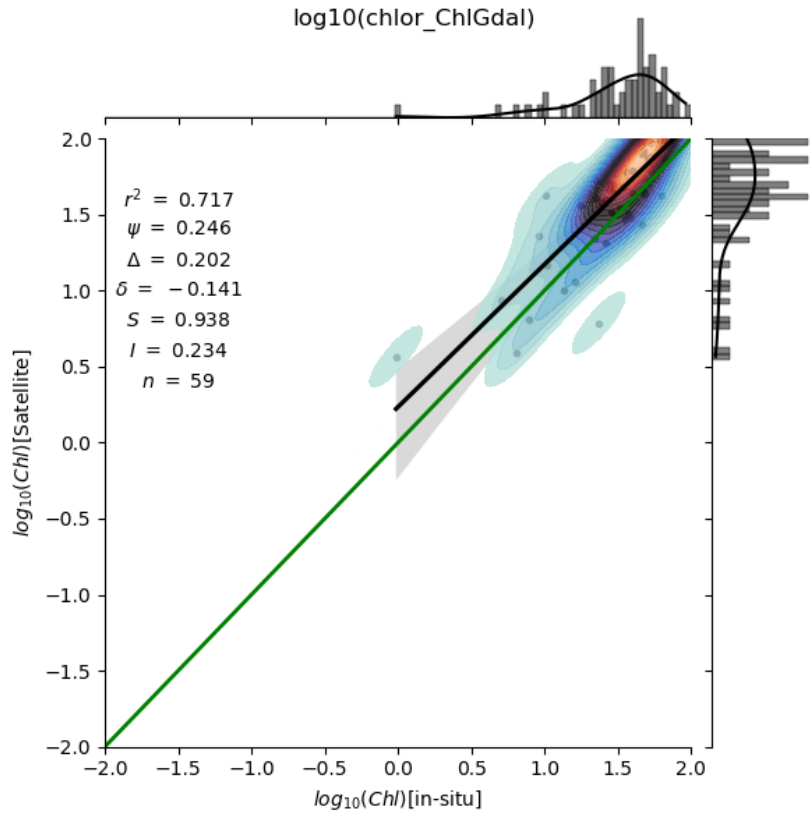

Figure 45: Optical Water Type class 14 optimal algorithm (Gdal) performance plot

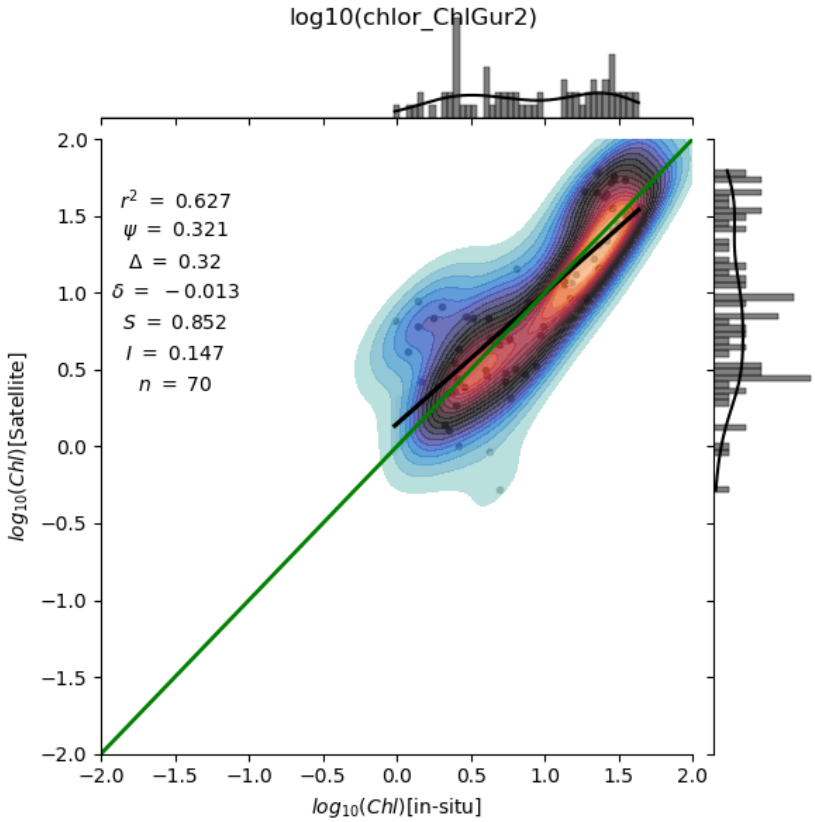

Figure 44: Optical Water Type class 15 optimal algorithm (Gur2) performance plot

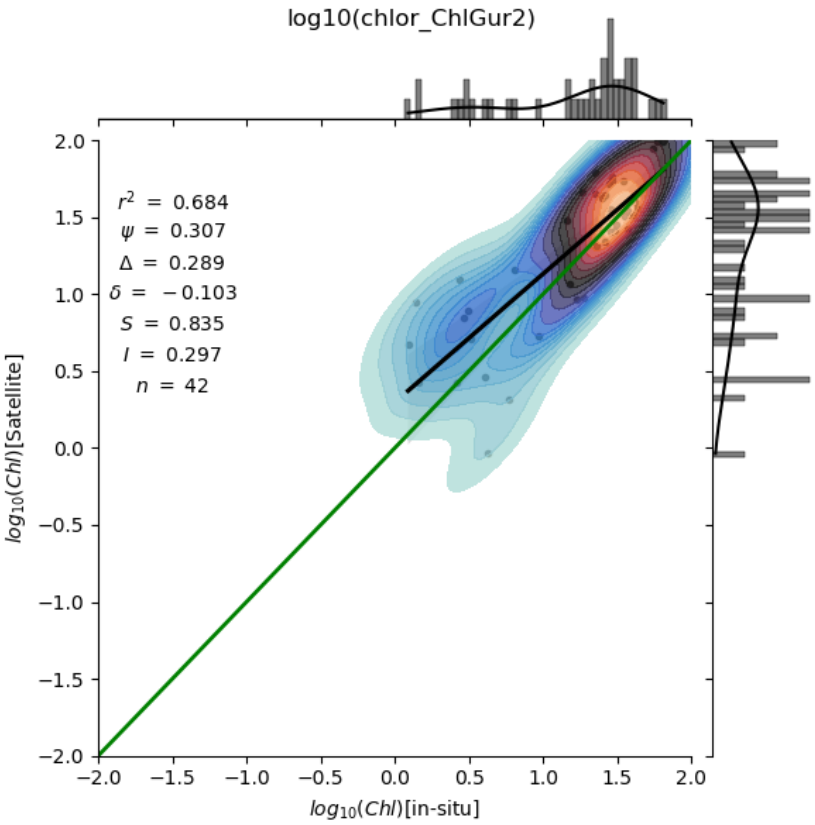

Figure 47: Optical Water Type class 16 optimal algorithm (Gur2) performance plot

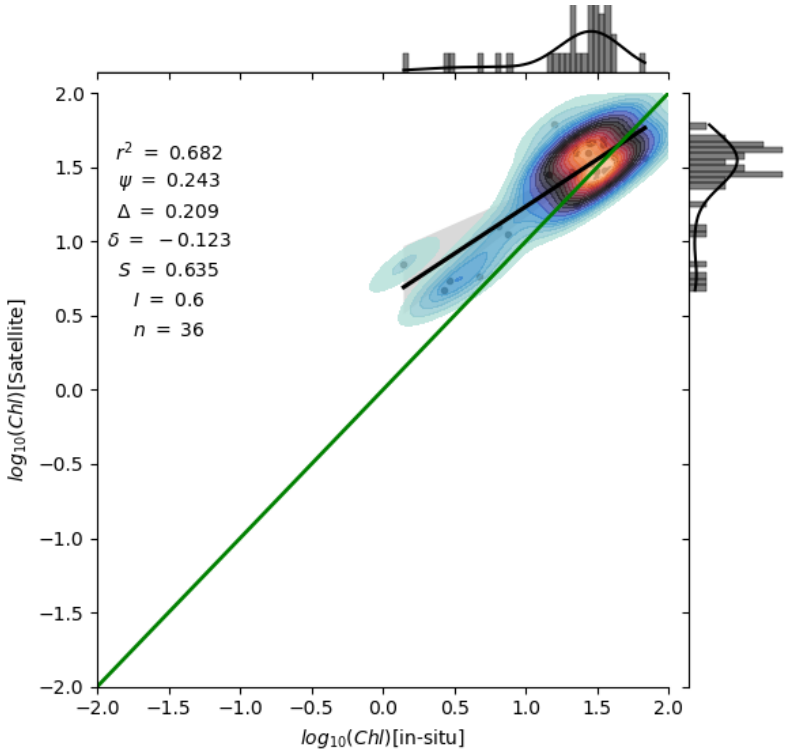

Figure 46: Optical Water Type class 17 optimal algorithm (Git) performance plot

7 References

Cazzaniga, I., Kwiatkowska, E., Obligis, E., (2018) Sentinel-3 OLCI Chlorophyll Index switch for low-chlorophyll waters Algorithm Theoretical Basis Document. Last accessed Dec 2022: https://www.eumetsat.int/media/47752

Dall'Olmo, G., Gitelson, A. A., & Rundquist, D. C. (2003). Towards a unified approach for remote estimation of chlorophyll-a in both terrestrial vegetation and turbid productive waters. *Geophysical Research Letters*, *30*(18).

Gilerson, A, Gitelson, A., Zhou, J., Gurlin, D., Moses, W., Ioannou, I, and Ahmed, S. (2010) Algorithms for remote estimation of chlorophyll-a in coastal and inland waters using red and near infrared bands, Opt. Express 18, 24109-24125

Gitelson, A. , Gurlin, , Moses, W. and Yacobi, Y. Q. Weng (Ed.), Advances in Environmental Remote Sensing: Sensors, Algorithms, and applications, 9781420091755, CRC Press, Taylor and Francis Group (2011), pp. 449-478

Jiang D, Matsushita B, Yang W (2020) A simple and effective method for removing residual reflected skylight in above-water remote sensing reflectance measurements. ISPRS Journal of Photogrammetry and Remote Sensing 165, 16-27. doi.org/10.1016/j.isprsjprs.2020.05.003

Matthews, M.W., Bernard, S., and Robertson, L. (2012) An algorithm for detecting trophic status (chlorophyll-*a*), cyanobacterial-dominance, surface scums and floating vegetation in inland and coastal waters Remote Sens. Environ., 124, pp. 637-652

Mishra, S. and Mishra, D.R. (2012) Normalized difference chlorophyll index: a novel model for remote estimation of chlorophyll-*a* concentration in turbid productive waters. Remote Sens. Environ., 117 (2012), pp. 394-406

Moses, W. J. , Gitelson, A. A., Berdnikov, S. and Povazhnyy, V., (2009) Satellite Estimation of Chlorophyll-a Concentration Using the Red and NIR Bands of MERIS—The Azov Sea Case Study, *IEEE Geoscience and Remote Sensing Letters*, vol. 6, no. 4, pp. 845-849, Oct. 2009, doi: 10.1109/LGRS.2009.2026657.

Neil, C., Spyrakos, E., Hunter, P.D., and Tyler, A.N. (2019) Corrigendum to "A global approach for chlorophyll-a retrieval across optically complex inland waters based on optical water types" [Remote Sens. Environ., 229: 159–178], Remote Sensing of Environment, Volume 246, 2020, 111837, ISSN 0034-4257, https://doi.org/10.1016/j.rse.2020.111837.

O'Reilly, J.E and Werdell. P.J. (2019) *Chlorophyll algorithms for ocean color sensors - OC4, OC5 & OC6*. Remote Sensing of Environment, Vol:229, pp:32-47, doi: 10.1016/j.rse.2019.04.021

Volpe, G., Colella, S., Brando, V. E., Forneris, V., La Padula, F., Di Cicco, A., Sammartino, M., Bracaglia, M., Artuso, F., and Santoleri, R. (2019). Mediterranean ocean colour Level 3 operational multi-sensor processing, Ocean Sci., 15, 127–146, https://doi.org/10.5194/os-15-127-2019.

Warren MA, Simis SGH, Selmes N. (2021) Complementary water quality observations from high and medium resolution Sentinel sensors by aligning chlorophyll-*a* and turbidity algorithms. Remote Sens Environ. 265:112651. doi: 10.1016/j.rse.2021.112651. PMID: 34732943; PMCID: PMC8507437.

Yang, W., Matsushita, B., Chen, J., Fukushima, B., and Ma, R. (2010) An enhanced three-band index for estimating chlorophyll-*a* in turbid case-II waters: case studies of Lake Kasumigaura, Japan, and Lake Dianchi, China IEEE Geosci. Remote Sens. Lett., 7 pp. 655-659

Appendix A: Updated optimal algorithm tables for v2 CERTO products

Given that a number of the algorithms in the chl-a round robin exercise have been fitted/parameterized using data from waters with a limited range of chl-a (compared to the range observed across all the CERTO regions) we do not extrapolate these algorithms beyond a lower chl-a concentration that is set per algorithm (Table 16).

Table 16: Lower limits of valid chl-a estimates from algorithms designed for non-deep-ocean waters.

Algorithm	**Lower limit of valid chl-a estimates [mg m^{-3}]**
Gdal	5.0
Git	10.0
Gur2	3.0
Gur3	3.0
GilSA2	5.0
GilSA3	5.0
Yang	10.0
NDCI	4.0
NDCI2	4.0
MPH	5.0

Updates to the CERTO processing system for the v2 product release included an atmospheric blending procedure of ACOLITE and POLYMER outputs, developed in WP3, to produce final CERTO v2 remote sensing reflectance products. This is only used for the MSI products, as initial analyses with the OLCI products suggested questionable nearshore artifacts. A new set of OWT classes for MSI were developed based on training data from these new reflectance products (Table 17), following the procedure detailed in §3 and §4. The OLCI OWT set remained unchanged from that created in v1 (Table 18).

Table 17: Sentinel-2 MSI v2 pan-regional Optical Water Type set, based on the atmospheric correction blended method used to produce MSI reflectance products. Band reflectances as rho_w (unitless).

Band (nm)	Class_1	Class_2	Class_3	Class_4	Class_5	Class_6	Class_7	Class_8	Class_9	Class_10	Class_11
443	0.00744	0.01105	0.01311	0.01158	0.01751	0.01365	0.01275	0.01357	0.01627	0.02376	0.03958
490	0.00929	0.01230	0.01538	0.01700	0.02246	0.02192	0.02208	0.02356	0.02673	0.03419	0.05147
560	0.00900	0.00895	0.01227	0.02258	0.02145	0.03242	0.03703	0.04167	0.04785	0.05949	0.08038
665	0.00221	0.00179	0.00246	0.00700	0.00439	0.01234	0.01934	0.02590	0.03346	0.04620	0.07004
705	0.00047	-0.00003	0.00022	0.00336	0.00135	0.00728	0.01481	0.02349	0.03428	0.05309	0.08584
740	-0.00004	-0.00013	-0.00005	0.00077	0.00029	0.00172	0.00373	0.00658	0.01135	0.02308	0.05255
783	0.00091	0.00093	0.00113	0.00210	0.00154	0.00323	0.00536	0.00828	0.01279	0.02404	0.05296
865	0.00014	0.00006	0.00010	0.00058	0.00023	0.00123	0.00243	0.00392	0.00643	0.01352	0.03515

Table 18: Sentinel-3 OLCI v1 pan-regional Optical Water Type set, based on POLYMER atmospheric correction alone used to produce OLCI reflectance products. Band reflectances as100 rho_w (unitless), multiplication used so that values fit into readable table.*

Band (nm)	CI_1	CI_2	CI_3	CI_4	CI_5	CI_6	CI_7	CI_8	CI_9	CI_10	CI_11	CI_12	CI_13	CI_14	CI_15	CI_16	CI_17	CI_18
400	0.064	0.298	0.640	0.296	0.687	1.219	1.063	0.533	1.466	0.662	0.985	0.804	2.038	1.341	0.941	1.110	1.445	1.056
412	0.253	0.459	0.774	0.475	0.836	1.298	1.191	0.703	1.571	0.827	1.145	0.941	2.142	1.285	1.103	1.098	1.262	1.208
443	0.498	0.652	0.921	0.702	1.021	1.327	1.355	0.941	1.782	1.084	1.439	1.206	2.469	1.146	1.520	1.199	1.175	1.725
490	0.621	0.778	1.011	0.908	1.187	1.342	1.542	1.262	2.116	1.495	2.013	1.738	3.039	1.388	2.346	1.796	1.785	2.792
510	0.684	0.791	0.924	1.008	1.158	1.111	1.467	1.413	2.071	1.716	2.296	2.067	2.986	1.757	2.797	2.240	2.318	3.405
560	0.820	0.830	0.795	1.270	1.126	0.800	1.348	1.884	1.972	2.480	3.211	3.253	2.844	3.399	4.230	3.821	4.104	5.302
620	0.323	0.266	0.203	0.511	0.319	0.180	0.356	0.794	0.540	1.181	1.471	1.956	0.776	2.209	2.696	3.142	3.988	4.045
665	0.199	0.152	0.100	0.319	0.159	0.084	0.160	0.497	0.278	0.745	0.936	1.305	0.439	1.610	1.913	2.439	3.501	3.180
674	0.277	0.227	0.167	0.388	0.222	0.139	0.214	0.556	0.327	0.786	0.954	1.287	0.482	1.437	1.863	2.344	3.440	3.084
681	0.281	0.227	0.161	0.393	0.215	0.129	0.201	0.566	0.310	0.809	0.967	1.327	0.457	1.482	1.882	2.418	3.532	3.092
709	0.059	0.012	-0.032	0.130	0.005	-0.052	0.003	0.240	0.081	0.437	0.554	0.960	0.161	2.059	1.361	2.232	3.433	2.482
754	0.079	0.071	0.063	0.109	0.095	0.050	0.112	0.152	0.120	0.213	0.237	0.346	0.119	0.561	0.434	0.688	1.192	0.749
779	0.050	0.042	0.034	0.078	0.059	0.024	0.071	0.119	0.086	0.181	0.211	0.327	0.094	0.544	0.435	0.723	1.273	0.776
865	-0.009	-0.017	-0.023	-0.004	-0.033	-0.018	-0.046	0.009	-0.031	0.036	0.060	0.118	-0.002	0.080	0.212	0.320	0.603	0.399
885	-0.042	-0.053	-0.059	-0.046	-0.083	-0.051	-0.105	-0.042	-0.092	-0.024	-0.003	0.040	-0.054	-0.049	0.133	0.194	0.392	0.283

Algorithms considered for the chl-a round robin exercise are listed in Table 19, further indicating which algorithms were evaluated with which sensor OWT set. The same for SPM is listed in Table 20. The procedure for SPM was different in that candidate algorithms were first calibrated per OWT and then put through the round robin analysis, thus all basis algorithms were considered for both sensors.

Table 19: Chlorophyll-a algorithms considered for the round robin analysis, indicating which were considered specifically for the MSI or OLCI Optical Water Type sets.

ID	Reference	MSI evaluated	OLCI evaluated
Gdal	Gitelson & Kondratyev (1991), Dall'Olmo et al. (2003)		x
GilSA2, GilSA3	Gilerson et al (2010)	x	x
Git	Gitelson et al (2011), Moses et al (2009)		x
Gons05	Gons et al (2005)	x	x
Gur2, Gur3	Gurlin et al (2011)		x
huCI	Hu et al. (2012)		x
huCI2	Hu et al. (2019)		x
MPH	Matthews et al. (2012)		x
NDCI, NDCI2	Mishra and Mishra (2012)		x
oc2, oc3	O'Reilly et al (2000)	x	x
oc2_warren, oc3_warren	Warren et al (2021)	x	
oc4	O'Reilly & Werdell (2019)		x
oc4Med	Volpe et al (2019)		x
oc4v7	O'Reilly & Werdell (2019)		x
oc5	O'Reilly & Werdell (2019)		x
oc5ci	Mix oc5 and oci		x
oc5NASA	Gohin et al. (2002)		x
oc6	O'Reilly & Werdell (2019)		x
oci	Hu et al. (2012), Cazzaniga et al (2018)		x
oci2	Hu et al. (2019)		x
ocx	O'Reilly et al. (2000)	x	x
Yang	Yang et al (2010)		x

Table 20: Suspended Particulate Matter algorithms considered for the round robin analysis, all algorithms were calibrated per sensor+OWT set and thus were all considered for the MSI and OLCI Optical Water Type sets.

ID	Reference
bala2020	Balasubramanian et al. (2020)
bin	Binding et al. (2010)
binUStir	Binding et al. (2010)
dek	Dekker (1993)
dox31 dox32	Doxaran et al. (2002)
jia	Jiang et al. (2021)
jorg	Jorgensen (2010)
mill	Miller & McKee (2004)
nec10_665 nec10_709 nec10_754 nec10_779 nec10_865	Nechad et al (2010)
nec16_665 nec16_709 nec16_754 nec16_779 nec16_865	Nechad et al (2016)
novoa2017G novoa2017B	Novoa et al. (2017)
ond	Ondrusek et al. (2021)
pet	Petus et al. (2010)
sis sis2011C sis2011T	Siswanto et al. (2011)
van	Vantrepotte et al. (2011)
wei2021	Wei et al (2021)
yu2019	Yu et al (2019)
zhang2014	Zhang et al. (2014)

The round robin procedure approach documented above was re-run across the v2 optical water types. To increase representation of CMEMS areas offshore waters, the matchup dataset was increased with OC-CCI in-situ chl-a data (total additional n=2,191, matchups additional n_OLCI=220 and n_MSI=71). Table 21 contains the updated per-water-type optimal algorithms used in the production of the final CERTO chl-a products with MSI data, the same in Table 22for OLCI data.

Table 21: Per Optical Water Type (OWT) optimal algorithms for chlorophyll-a estimation with MSI following additional in-situ data provision from OC-CCI and round robin comparison for V2 data production.

MSI OWT class	MSI chl-a algorithm v2
1	oc3
2	oc3
3	oc3
4	oc3
5	oc3
6	oc3_warren
7	oc3
8	oc2
9	oc3
10	Gons05
11	oc2

Table 22: Per Optical Water Type (OWT) optimal algorithms for chlorophyll-a estimation with OLCI following additional in-situ data provision from OC-CCI and round robin comparison for V2 data production.

OLCI OWT class	OLCI chl-a algorithm v2
1	oc4Med
2	oc3
3	oc3
4	GilSA2_nan
5	oc4Med
6	oci2
7	oc5ci
8	oc5
9	oc3
10	oc5
11	oc4Med
12	oc5
13	oc5ci
14	Gdal
15	oc4Med
16	GilSA2_nan
17	Git
18	GilSA2_nan

Table 23 contains the updated per-water-type optimal algorithms used in the production of the final CERTO SPM products with MSI data, the same in Table 24 for OLCI data.

Table 23: Per Optical Water Type (OWT) optimal algorithms for suspended particulate matter (SPM) estimation with MSI following OWT coefficient calibration and subsequent round robin comparison for V2 data production.

MSI OWT class	MSI SPM algorithm v2
1	jia
2	bala2020
3	bala2020
4	ond
5	wei2021
6	wei2021
7	wei2021
8	nec783nm
9	nec783nm
10	dek
11	van

Table 24: Per Optical Water Type (OWT) optimal algorithms for suspended particulate matter (SPM) estimation with OLCI following OWT coefficient calibration and subsequent round robin comparison for V2 data production.

OLCI OWT class	OLCI SPM algorithm v2
1	jia
2	jia
3	bin
4	bin
5	bin
6	bin
7	bin
8	wei2021
9	sis2011T
10	nec754nm
11	nec779nm
12	nec779nm
13	nec779nm
14	wei2021
15	bin
16	nec779nm
17	bin
18	sis2011T

Appendix References

Balasubramanian, S.V., Pahlevan, N., Smith, B., Binding, C., Schalles, J., Loisel, H., Gurlin, D., Greb, S., Alikas, K., Randla, M., Bunkei, M., Moses, W., Nguyễn, H., Lehmann, M.K., O'Donnell, D., Ondrusek, M., Han, T.-H., Fichot, C.G., Moore, T., Boss, E. (2020) Robust algorithm for estimating total suspended solids (TSS) in inland and nearshore coastal waters. Remote Sensing of Environment 246: 111768. https://doi.org/10.1016/j.rse.2020.111768

Binding, C.E., Jerome, J.H., Bukata, R.P., Booty W.G. (2010) Suspended particulate matter in Lake Erie derived from MODIS aquatic colour imagery, International Journal of Remote Sensing 31:19, 5239-5255. DOI: 10.1080/01431160903302973

Cazzaniga, I., Kwiatkowska, E., Obligis, E., (2018) Sentinel-3 OLCI Chlorophyll Index switch for low-chlorophyll waters Algorithm Theoretical Basis Document. Last accessed Dec 2022: https://www.eumetsat.int/media/47752

Dall'Olmo, G., Gitelson, A. A., & Rundquist, D. C. (2003). Towards a unified approach for remote estimation of chlorophyll-a in both terrestrial vegetation and turbid productive waters. *Geophysical Research Letters*, *30*(18).

Dekker, A.G., 1993. Detection of Optical Water Quality Parameters for Eutrophic Waters by High Resolution Remote Sensing. Proefschrift Vrije Universiteit Amsterdam, Amsterdam, The Netherlands (237 pp).

Doxaran, D., Froidefond, J.-M., Lavender, S., Castaing, P (2002) Spectral signature of highly turbid waters Application with SPOT data to quantify suspended particulate matter concentrations. Remote Sens. Environ. 81, 149–161. https://doi.org/10.1016/S0034-4257(01)00341-8

Gilerson, A, Gitelson, A., Zhou, J., Gurlin, D., Moses, W., Ioannou, I, and Ahmed, S. (2010) Algorithms for remote estimation of chlorophyll-a in coastal and inland waters using red and near infrared bands, Opt. Express 18, 24109-24125

Gitelson, A. , Gurlin, , Moses, W. and Yacobi, Y. Q. Weng (Ed.), Advances in Environmental Remote Sensing: Sensors, Algorithms, and applications, 9781420091755, CRC Press, Taylor and Francis Group (2011), pp. 449-478

Gitelson, A. & Kondratyev K.Y. (1991) Optical models of mesotrophic and eutrophic water bodies. International Journal of Remote Sensing, 12:3, 373-385. https://doi.org/10.1080/01431169108929659

Gohin, F., Druon, J.N., Lampert, L., 2002. A five channel chlorophyll concentration algorithm applied to SeaWiFS data processed by SeaDAS in coastal waters. Int. J. Remote Sens. 23, 1639–1661. http://dx.doi.org/10.1080/01431160110071879

Gons H.J., Rijkeboer M., Ruddick K.G. (2005) Effect of a waveband shift on chlorophyll retrieval from MERIS imagery of inland and coastal waters. Journal of Plankton Research, 27:1, 125–127. https://doi.org/10.1093/plankt/fbh151

Gurlin D., Gitelson A.A., Moses W.J. (2011) Remote estimation of chl-a concentration in turbid productive waters - Return to a simple two-band NIR-red model? Remote Sensing of Environment 115, 3479–3490. doi:10.1016/j.rse.2011.08.011

Hu, C., Lee Z., Franz B. (2012) Chlorophyllaalgorithms for oligotrophic oceans: A novel approach based onthree-band reflectance difference,J. Geophys. Res., 117:C01011. doi:10.1029/2011JC007395

Hu, C., Feng, L., Lee, Z., Franz, B. A.,Bailey, S. W., Werdell, P. J., Proctor,C. W. (2019). Improving satellite global chlorophyll a data products through algorithm refinement and data recovery. Journal of Geophysical Research: Oceans,124, 1524–1543. https://doi.org/10.1029/2019JC014941

Jiang D., Matsushita, B., Pahlevan, N., Gurlin, D., Lehmann, M.K., Fichot, C.G., Schalles, J., Loisel, H., Binding, C., Zhang, Y., Alikas, K., Kangro, K., Uusõue, M., Ondrusek, M., Greb, S., Moses, W.J., Lohrenz, S., O'Donnell, D. (2019) Remotely estimating total suspended solids concentration in clear to extremely turbid waters using a novel semi-analytical method. Remote Sensing of Environment, 258: 112386. https://doi.org/10.1016/j.rse.2021.112386

Jorgensen P.K. (1999) Standard CZCS Case 1 algorithms in Danish coastal waters. International Journal of Remote Sensing, 20:7, 1289-1301. DOI: 10.1080/014311699212731

Matthews, M.W., Bernard, S., Robertson, L., 2012. An algorithm for detecting trophic status (chlorophyll-a), cyanobacterial-dominance, surface scums and floating vegetation in inland and coastal waters. Remote Sens. Environ. 124, 637–652. DOI: 10.1016/j.rse.2012.05.032

Mishra, S. and Mishra, D.R. (2012) Normalized difference chlorophyll index: a novel model for remote estimation of chlorophyll-*a* concentration in turbid productive waters. Remote Sens. Environ., 117 (2012), pp. 394-406

Moses, W. J. , Gitelson, A. A., Berdnikov, S. and Povazhnyy, V., (2009) Satellite Estimation of Chlorophyll-a Concentration Using the Red and NIR Bands of MERIS—The Azov Sea Case Study, *IEEE Geoscience and Remote Sensing Letters*, vol. 6, no. 4, pp. 845-849, Oct. 2009, doi: 10.1109/LGRS.2009.2026657.

Nechad, B., Ruddick, K.G., Park, Y. (2010) Calibration and validation of a generic multisensor algorithm for mapping of total suspended matter in turbid waters. Remote Sens. Environ. 114, 854–866. https://doi.org/10.1016/j.rse.2009.11.022

Nechad, B., Dogliotti, A., Ruddick, K.G., Doxaran D. (2016) Particulate backscattering and suspended matter concentration retrieval from remote-sensed turbdity in various coastal and riverine turbid waters. ESA Living Planet Symposium, Prague, 9-13 May 2016, ESA-SP 740

Neil, C., Spyrakos, E., Hunter, P. D., Tyler, A. N. (2019) A global approach for chlorophyll-a retrieval across optically complex inland waters based on optical water types. Remote Sens. Environ. 229, 159–178. doi: 10.1016/j.rse.2019.04.027

Novoa, S. Doxaran, D., Ody, A., Vanhellemont, Q., Lafon, V., Lubac, B., Gernez, P.
(2017) Atmospheric Corrections and Multi-Conditional Algorithm for Multi-Sensor Remote Sensing of Suspended Particulate Matter in Low-to-High Turbidity Levels Coastal Waters. Remote Sens. 9(1), 61. https://doi.org/10.3390/rs9010061

Ondrusek, M., Stengel, E., Kinkade, C.S., Vogel, R.L., Keegstra, P., Hunter, C., Kim, C. (2012) The development of a new optical total suspended matter algorithm for the Chesapeake Bay. Remote Sensing of Environment 119: 243-254. https://doi.org/10.1016/j.rse.2011.12.018

O'Reilly, J.E and Werdell. P.J. (2019) *Chlorophyll algorithms for ocean color sensors - OC4, OC5 & OC6*. Remote Sensing of Environment, Vol:229, pp:32-47, doi: 10.1016/j.rse.2019.04.021

O'Reilly, J.E., Maritorena, S., Siegel, D., O'Brien, M.C., Toole, D., Mitchell, B.G. (2000) Postlaunch Calibration and Validation Analyses SeaWiFS, Part 3. Nasa tech. memo. 2000-206892. vol. 11. NASA Goddard Space Flight Center.

Petus, C., Chust, G., Gohin, F., Doxaran, D., Froidefond, J.-M. (2010) Estimating turbidity and total suspended matter in the Adour River plume (South Bay of Biscay) using MODIS 250-m imagery. Cont. Shelf Res. 30: 379–392. doi: 10.1016/j.csr.2009.12.007

Siswanto, E., Tang, J., Yamaguchi, H., Ahn, Y.-H., Ishizaka, J., Yoo, S., Kim, S.-W., Kiyomoto, Y., Yamada, K., Chiang, C., Kawamura H. (2011) Empirical ocean-color algorithms to retrieve chlorophyll-a, total suspended matter, and colored dissolved

organic matter absorption coefficient in the Yellow and East China Seas. Journal of Oceanography 67: 627–650. . https://doi.org/10.1007/s10872-011-0062-z

Vantrepotte, V., Loisel, H., Meriaux, X., Neukermans, G., Dessailly, D., Jamet, C., Gensac, E., Gardel, A. (2011).Seasonal and inter-annual (2002-2010) variability of the suspended particulate matter as retrieved from satelliteocean color sensor over the French Guiana coastal waters. Journal of Coastal Research, SI 64 (Proceedings of the11th International Coastal Symposium), 1750 – 1754. Szczecin, Poland, ISSN 0749-0208

Volpe, G., Colella, S., Brando, V. E., Forneris, V., La Padula, F., Di Cicco, A., Sammartino, M., Bracaglia, M., Artuso, F., and Santoleri, R. (2019). Mediterranean ocean colour Level 3 operational multi-sensor processing, Ocean Sci., 15, 127–146, https://doi.org/10.5194/os-15-127-2019.

Warren MA, Simis SGH, Selmes N. (2021) Complementary water quality observations from high and medium resolution Sentinel sensors by aligning chlorophyll-*a* and turbidity algorithms. Remote Sens Environ. 265:112651. doi: 10.1016/j.rse.2021.112651. PMID: 34732943; PMCID: PMC8507437.

Wei, J. Wang, M., Mikelsons, K., Jiang, L., Kratzer, S. (2022) Global satellite water classification data products over oceanic, coastal, and inland waters. Remote Sens. Environ. 282, 113233. https://doi.org/10.1029/2021JC017303

Yang, W., Matsushita, B., Chen, J., Fukushima, B., and Ma, R. (2010) An enhanced three-band index for estimating chlorophyll-*a* in turbid case-II waters: case studies of Lake Kasumigaura, Japan, and Lake Dianchi, China IEEE Geosci. Remote Sens. Lett., 7, 655-659

Yu, X., Lee, Z., Shen, F., Wang, M., Wei, J., Jiang, L., Shang Z. (2019) An empirical algorithm to seamlessly retrieve the concentration of suspended particulate matter from water color across ocean to turbid river mouths. Remote Sensing of Environment, 235: 111491. https://doi.org/10.1016/j.rse.2019.111491

Zhang, P., Wai, O. W. H., Chen, X., Lu, J., Tian, L. (2014) Improving Sediment Transport Prediction by Assimilating Satellite Images in a Tidal Bay Model of Hong Kong. Water 6, 642–660. doi:10.1371/journal.pone.0098055.g002